Multiscale Modelling of Urban Climate

THÈSE N^O 4531 (2009)

PRÉSENTÉE LE 30 OCTOBRE 2009
À LA FACULTÉ ENVIRONNEMENT NATUREL, ARCHITECTURAL ET CONSTRUIT
LABORATOIRE D'ÉNERGIE SOLAIRE ET PHYSIQUE DU BÂTIMENT
SECTION D'ARCHITECTURE

ÉCOLE POLYTECHNIQUE FÉDÉRALE DE LAUSANNE

POUR L'OBTENTION DU GRADE DE DOCTEUR ÈS SCIENCES

PAR

Adil RASHEED

EPFL

ÉCOLE POLYTECHNIQUE
FÉDÉRALE DE LAUSANNE

Suisse
2009

Abstract

Climate has a direct impact on cities' energy flows due to the space conditioning (heating, cooling) needs of the buildings accommodated. This impact may be reinforced due to climate change and to the (so called) urban heat island effect. The corresponding changes in energy demands alter greenhouse gas emissions so that there is a feedback loop. To be able to simulate cities' metabolism with reasonable accuracy it is thus important to have good models of the urban climate. But this is complicated by the diverse scales involved. The climate in a city, for example, will be affected not only by the buildings within the urban canopy (the size of a few meters) but also by large topographical features such as nearby water bodies or mountains (the size of a few kilometers). Unfortunately it is not possible to satisfactorily resolve all of these scales in a computationally tractable way using a single model. It is however possible to tackle this problem by coupling different models which each target different climatic scales. For example a macro model with a grid size of $200 - 300km$ may be coupled with a meso model having a grid of $0.5 - 1km$, which itself may be coupled with a micro model of a grid size of 5-10 meters. Here we describe one such approach.

Firstly, freely available results from a macro-model are input to a meso-model at a slightly larger scale than that of our city. This meso-model is then run as a pre-process to interpolate the macro-scale results at progressively finer scales until the boundary conditions surrounding our city are resolved at a compatible scale. The meso-model may then be run in the normal way. In the rural context this may simply involve associating topography and average land use data with each cell, the former affecting temperature as pressure changes with height the latter affecting temperature due to evapo(transpir)ation from water bodies or vegetated surfaces. In the urban context however, it is important to account for the energy and momentum exchanges between our built surfaces and the adjacent air, which implies some representation of 3D geometry. For this we use a new urban canopy model in which the velocity, temperature and scalar profiles are parameterized

as functions of built densities, street orientation and the dimensions of urban geometric typologies. These quantities are then used to estimate the corresponding sources and sinks of the momentum and energy equations.

Even at the micro-scale the use of conventional computational fluid dynamics modeling is unattractive because of the time involved in grid generation / tuning and the definition of boundary conditions. Furthermore, even the simplest geometry may require hundreds of millions of grid cells for a domain corresponding to a single meso-model cell, particularly if unstructured grids are used. To overcome this problem we describe a new approach based on immersed boundaries in which the flow around any complex geometry can be computed using a simple Cartesian grid, so that users benefit from both improved productivity and accuracy. Thus, a completely coupled macro, meso and micro model can be used to predict the temperature, wind and pressure field in a city taking into account not only the complex geometries of its built fabric but also the scales which are bigger than the city itself.

In this thesis we describe for the first time the theoretical basis of this new multi-scale modeling approach together with examples of its application.

KEY WORDS: Multiscale Modeling, Large Eddy Simulation, Urban Canopy Model, Immersed Surface Technique, Simplified Radiosity Algorithm

Résumé

Le climat a un impact direct sur les flux d'énergie dans les villes, de par son influence sur les besoins en chauffage et refroidissement des bâtiments concernés. Cet impact peut être renforcé par les changements climatiques ainsi que par l'effet « d'îlot de chaleur urbain » (urban heat island). Les variations correspondantes des demandes en énergie modifient les émissions de gaz à effet de serre, créant ainsi une boucle rétroactive. Il est donc important, pour pouvoir simuler le métabolisme des villes avec une précision raisonnable, de disposer de bons modèles du climat urbain.

Les différentes échelles impliquées rendent néanmoins le problème complexe. Le climat d'une ville, par exemple, sera affecté non seulement par les bâtiments du tissu urbain (de l'ordre de quelques mètres), mais aussi par les spécificités typographiques à plus grande échelle, comme une surface d'eau proche ou des montagnes (de l'ordre de quelques kilomètres). Malheureusement, il n'est pas possible de simuler de manière satisfaisante ces différentes échelles par des moyens informatiques maîtrisables en utilisant un seul modèle. Il est cependant possible de gérer ce problème en couplant différents modèles se concentrant sur différentes échelles climatiques. Par exemple, un modèle macroscopique avec une taille de maille de 200 à 300 km peut être couplé à un modèle méso-échelle avec une maille de $0,5$ à 1 km, qui peut lui-même être couplé à un modèle micro-échelle d'un maillage de 5 à 10 mètres. Nous décrivons ici une telle approche.

En premier lieu, les résultats d'un modèle à grande échelle, disponibles librement, sont donnés en entrée à un modèle intermédiaire d'une échelle légèrement supérieure à la ville. Ce modèle méso-échelle est appliqué comme un préprocesseur pour progressivement interpoler les résultats de l'échelle macroscopique à des échelles plus fines, jusqu'à ce que les conditions de bords autour de notre ville soient résolues à une échelle compatible. Le modèle méso-échelle peut alors être exécuté normalement. Dans le contexte rural, cela peut revenir simplement à associer à chaque cellule une topographie, qui a modifie la température lorsque

la pression change avec l'altitude, et une utilisation du sol représentative, qui agit sur la température par les effets d'évapotranspiration des surfaces d'eau et de la végétation. Dans le contexte urbain, par contre, il est aussi important de tenir compte des échanges d'énergie et d'impulsion entre les surfaces construites et l'air adjacent, ce qui nécessite la représentation d'une géométrie 3D équivalente. Pour ce faire, nous utilisons un modèle de canopée urbaine dans lequel la vitesse, la température et les profils scalaires de l'air sont des fonctions dépendant des densités de construction, de l'orientation des rues et des dimensions des géométries urbaines. Ces grandeurs sont alors utilisées pour estimer les sources et puits des équations gouvernant l'impulsion et l'énergie.

À l'échelle microscopique aussi, l'utilisation de la modélisation conventionnelle en mécanique des fluides numérique (computational fluid dynamics) semble inappropriée, en raison du temps nécessaire à la génération et au réglage du maillage et à la définition des conditions de bord. En outre, même la géométrie la plus simple peut nécessiter un maillage de centaines de millions de cellules pour le domaine correspondant à une cellule du modèle méso-échelle, en particulier si des maillages non-structurées sont utilisées. Ces derniers sont attrayants pour des raisons de productivité, mais souffrent d'instabilités numériques. Pour surmonter ce problème, nous décrivons ici une nouvelle approche basée sur des surfaces immergées, dans laquelle le flux autour de n'importe quelle géométrie complexe peut être calculé en utilisant un simple maillage cartésien, de manière à ce que les utilisateurs bénéficient à la fois d'une productivité accrue et d'une précision améliorée.

Ainsi un modèle multi-échelle complètement couplé peut être utilisé pour prédire la température, le vent et le champ de pression dans une ville, en tenant compte non seulement des géométries complexes de l'espace construit, mais aussi des échelles qui sont plus grandes que la ville elle-même. Cette thèse décrit pour la première fois les bases théoriques de cette nouvelle approche de modélisation multi-échelle, ainsi que ses applications pratiques.

MOT CLÉS: Multiscale Modelling, Large Eddy Simulation, Urban Canopy Model, Immersed Surface Technique, Simplified Radiosity Algorithm

Acknowledgements

First of all I would like to thank Professor Jean-Louis Scartezzini and Professor Darren Robinson for having faith in me and giving me the opportunity to work in the Laboratory of Solar Energy and Building Physics at the Swiss Federal Institute of Technology Lausanne. I would like to express my deepest and most sincere gratitudes to my supervisor, Professor Darren Robinson. His wide spectrum of knowledge and logical ways of thinking have been of great value to me. His understanding, encouraging and personal guidance have provided a good basis for the present thesis.

I am very much thankful to my Masters thesis director, Professor Anil W. Date under whose guidance I developed interest in Computational Fluid Dynamics, the knowledge of which was extensively used in the present work.

I owe my most sincere gratitudes to Professor Alain Clappier, who gave me the opportunity to work with his group in the Soil and Air Pollution Laboratory, EPFL and gave me untiring help during my difficult moments.

My warm thanks are due to Dr. Djamel Lakehal, General Manager and Dr. Chidambaram Narayanan, Research and Development Head, ASCOMP GmbH, who directed me into the details of Turbulence Modeling and Immersed Surface Technique. Their kind support and guidance have been of great value in this study. Thanks also to them for sharing their codes for most of the Microscale Simulations.

I wish to thank Dr. Alberto Martilli, Senior Scientist, CIEMAT for his essential assistance in reviewing and constructive criticism on parts of this study.

I also wish to thank my friend Mr. Deepak Angrula for helping me out during the end of the project in making the work accessible to the masses with his excellent knowledge of software architecture and design.

My special thanks goes to Miss Diane Perez for spending her precious time in translating the abstract into French with utmost care.

I am also thankful to Professor Marshall Shepherd and Professor Hiroyuki Kusaka for accepting to spend their precious time in reviewing my thesis and giving their valuable suggestions.

My special thanks also go to Mr. Jerome Kaempf and Dr. Andrea Krpo for the time we spent together discussing about radiosity, building physics and mesoscale codes.

I wouldn't have been able to maintain the healthy state-of-mind necessary to finish the thesis without a constant support from my friends. For this I thank: Sandeep Dhanik, Suraj Ravindran, Saurabh Aggarwal, Anothai Thanachareonkit, Maria Cristina, Nandita Aggarwal, Apiparn Borisuit, Debabrata Dash ,Sandy Herzlieb, Frederic Haldi and Urs Wilke. Good time or bad time they were always with me encouraging me and cheering me up whenever I needed such encouragement badly.

Special thanks also go to three dearest ladies in our laboratory: Suzanne, Barbara and Sylvette who made my life extremely comfortable leaving me nothing to worry about administrative stuffs.

I owe my loving thanks to my mother. She has lost a lot due to my research abroad. Without her encouragement and understanding it would have been impossible for me to finish this work. My special gratitude is due to my brothers, my sisters and their families for their loving support. My loving thanks are due to other LESO members and friends. They made me feel part of a happy family in Switzerland.

Contents

List of Figures

List of Tables

Abbreviations

Acronym	What (it) Stands For
LAH	List Abbreviations Here
GNP	Gross National Product
PBL	Planetary Boundary Layer
RANS	Reynolds Averaged Navier Stokes
DNS	Direct Numerical Simulation
LES	Large Eddy Simulation
URANS	Unsteady Reynolds Averaged Navier Stokes
DEM	Digital Elevation Model
UCM	Urban Canopy Model
BEM	Building Energy Model
NURBS	Non-Uniform Rational B-Spline
TKE	Turbulent Kinetic Energy
SGS	Subgrid scale
CDS	Central Differencing Scheme
HLPA	Hybrid Linear Parabolic Approximation
GMRES	Generalized Minimal Residual Method
DSM	Dynamic Smagorinsky
TEB	Town Energy Balance
SEB	Surface Energy Balance

Nomenclature

α_{ext} Albedo of external built surfaces

δ_{sf} solid-fluid interface thickness

ℓ Eulerian integral length scale

ϵ Dissipation

ϵ_{ext} Emmissivity of the external buillt surfaces

κ wave number

λ_k Kolmogorov microscale

μ Dynamic Viscosity

ν Dynamic Viscosity

ν_t Eddy viscosity

Ω Angular velocity of the earth

$\overline{p}$ Time averaged pressure

$\overline{u_i}$ Spatially filtered velocity in tensor form

$\overline{u_j}$ Spatially filtered velocity in tensor form

Φ Solid angle

ϕ_s Level-set function

ρ Density

ρ^f Density of fluid phase

ρ^s Density of solid phase

ρ_{mat} Density of built material

ρ_o Density of air at hydrostatic state

τ Kolmogorov time scale

θ' Fluctuation in potential temperature

θ_o Potential temperature of reference state

$\vec{D_u}$ Source term for momentum equation

$\vec{f}$ Momentum source

$\vec{u}$ Instantaneous velocity vector

$\vec{v^G}$ Geostrophic Wind

$\vec{v}$ Time averaged velocity vector

$\widehat{\sigma}$ Proportion of sky patch that can be seen

$\widehat{p}$ Number of sky patches

$\widehat{R}$ Radiance

B_1, B_2 Building width and bredth

C_ϵ Constant in TKE dissipation term

C_p Specific heat capacity of air

Cp_{mat} Specific heat capacity of built material

D_θ Source term for energy equation

e Turbulent kinetic energy

E_c Turbulent Kinetic Energy on UCM grid

$En(\kappa)$ Energy

f_μ Von Driest damping factor

g Acceleration due to gravity

g' Reduced acceleration due to gravity

H Cube height

$H(\phi_s)$ Heaviside function

h_{ext} External heat transfer coefficient

$I_{b\beta}$ Direct beam irradiance

I_{bn} Beam normal irradiance

$I_{d\beta}$ Direct sky irradiance

K_{mat} Thermal conductivity of built material

K_{zi} Turbulent diffusivity

l_ϵ Dissipation length scale

l_k Turbulent length scale

P Hydrostatic pressure

p_o Reference pressure

$Pb(z)$ Probability of having a building of height z

q_{ext} Heat flux incedent on external built surfaces

Q_e Source of TKE equation

Q_T Source term for the energy equation

R Gas constant

R^* Radiance of the surface which dominates the obstruction to sky

Re Reynolds Number

Rl_{ext} Longwave radiation incedent on external built surfaces

Rs_{ext} Shortwave radiation incedent on external built surfaces

T Temperature

t time

T_{amb} Ambient temperature

T_n Surface temperature

$u^{'}, v^{'}, w^{'}$ Fluctuation in velocity with time

U^{hor} Magnitude of horizontal velocity components

U_b Bulk velocity

U_c, V_c Horizontal velocity components on the UCM grid

U_i, U_j Time averaged velocity components

u_j, u_i Velocity in tensor notation

$v^{'}_z$ Time averaged vertical velocity component

W_1, W_2 Street widths in two directions

Dedicated to my family and friends. . .

Chapter 1

Introduction

Cities are increasingly expanding their boundaries and populations. Increased industrialization and urbanization in recent years have affected dramatically the number of urban buildings with major effects on the energy consumption of this sector. The number of urban dwellers have risen from 600 million in 1920 to 2 billion in 1986. One hundred years ago, only 14% lived in cities and in 1950, less than 30% of the world population was urban. By the end of 2000 the percentage rose to 50% and if the trend continues then by the end of 2030, 60% of the world's population will be living in urban area[1]. Today, at least 180 cities support more than one million inhabitants each. With so many people living and working in urban areas there is bound to be an increase in the energy demand for cooling or heating purpose in order to maintain proper thermal comfort. Statistical data (Stanners and Bourdeau (1995)) already shows that the amount of energy consumed by cities for heating and cooling of offices and residential buildings in western and southern Europe has increased significantly in the last two decades. An analysis, (Jones (1992)), showed that a 1% increase in the per capita GNP leads to an almost equal (1.03), increase in energy consumption. However, an increase of the urban population by 1% increases the energy consumption by 2.2%, i.e. the rate of change in energy use is twice the rate of change in urbanization.

---

[1]IPCC report, http://www.ipcc.ch/ Retrieved 2008-09-17

These data show clearly the impact that urbanization may have on energy use. Thus, it becomes increasingly important to study urban climatic environments and to apply this knowledge to improve people's environment and at the same time decrease the energy consumption in cities.

In the subsequent sections we describe briefly the planetary boundary layer and a phenomenon known as Urban Heat Island which is the consequence of urbanization and whose existence is established through a series of field experiments [Bubble Project [23], Kolokotroni and Giridharan (2008) and numerical simulations. At the end of this chapter we present a brief description of the structure of this thesis.

1.1   Urban Climate and the Planetary Boundary Layer (PBL)

In the vertical direction, the atmosphere can be divided into four distinct layers of different thickness, usually associated with a specific vertical temperature distribution (Jacobson (1999)) in the troposphere, the stratosphere, the mesosphere and the thermosphere. In particular with a thickness of around $10km$ ($16km$ at the Equator and $7km$ at the Poles according to Seinfield and Pandis (1998)), the troposphere represents the lowest portion of the Earth's atmosphere and contains almost 80% of the atmosphere mass and almost all the water vapor. In this layer one can furthermore distinguish two different parts (Oke (1987)): the Planetary Boundary Layer (PBL) from the ground to about $1km$ and the Free Atmosphere from $1km$ above the ground to the tropopause. As explained by Oke (1988), the PBL is that part of the atmosphere which is directly influenced by the presence of the earth's surface. In particular physical and chemical processes in the PBL can be deeply modified by the presence of urban surfaces which in turn affect meteorological conditions, air quality and consequently human comfort. As we can observe in Figure 1.1 there are mechanical and thermal factors with which

---

[3]http://pages.unibas.ch/geo/mcr/Projects/BUBBLE/
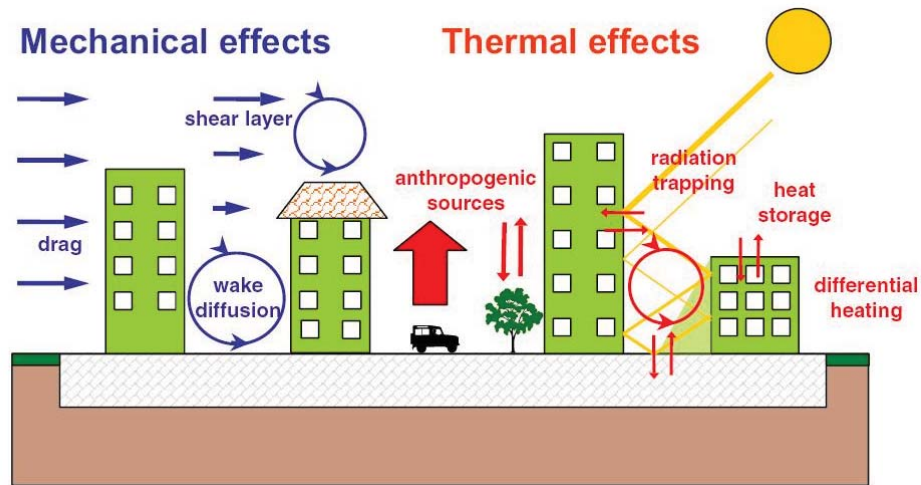
FIGURE 1.1: Main building effects. Source: Air and Soil Pollution Laboratory (LPAS)

urban regions can modify the local microclimate and the vertical structure of the atmosphere. Mechanical effects are induced by the high roughness of the urban surfaces. Buildings produce, in fact, an intense drag as well as a shear layer at the top of the canopy where mean kinetic energy is transformed into turbulent kinetic energy. Cities also generate a turbulent wake diffusion and decrease wind speed Roth (2000). Thermal effects are produced as geometrical and physical properties of urban areas generate a relatively dry environment and a differential heating / cooling compared to rural regions (explained in the next section). Radiation trapping effects in street canyons and heat storage in buildings modify the radiative and energy budget often causing a city to be warmer than the surrounding areas. This is one of the most important phenomena generated by the presence of cities and is called the Urban Heat Island (UHI) effect.

1.2 Introduction to Urban Heat Island Effect

A range of factors may vary between a rural and urban areas which may enhance or minimize the intensity of Urban Heat Island. Below we explain the causes of UHI one by one.

1.2.1 Causes of UHI

1. *Thermo-physical properties of the built surfaces:* Materials commonly used in urban areas, such as concrete and asphalt, have significantly different thermal bulk properties (including heat capacity and thermal conductivity) and surface radiative properties (albedo and emissivity) than the surrounding rural areas. Since urban materials have a relatively high specific heat capacity, during the day they can store a large amount of heat which can be slowly restituted at night. In consequence the urban temperature profile may be positively shifted in phase relative to rural profile.

2. *City Geometry and Radiation balance:* The temperature distribution in urban areas is highly affected by the city geometry and the corresponding urban radiation balance. This Urban fabric has relatively high rugosity compared to relatively flat rural terrain, so that more solar radiation is absorbed due to reflections between surfaces, modifying urban surface temperatures. The intensity of the emitted radiation depends heavily on the view factor of the surface regarding the sky. Due to the relatively small difference in temperature between surfaces the dominant path of longwave radiation exchange is from surface to sky rather than from surface to surface. Again because of the high rugosity of our urban fabrics these sky view factors are small relative to rural settings, so that longwave radiation exchange is diminished. Thus more solar (shortwave) radiation is absorbed and less longwave radiation is emitted, so that the mean temperature is higher in urban than in rural settings. This warming may be exacerbated by the reduction in mean wind speed, which also inhibits cooling by convection.

3. *Anthropogenic heat generation:* Another cause of UHI is anthropogenic heat generation due to heating (or cooling) of buildings, though they are relatively minor in summer and generally in low- and mid-latitude areas. In winter and especially in high latitudes, when solar radiation is considerably smaller, these effects can contribute the majority of UHI. As urban areas are often

inhabited by large numbers of people, heat generation by human activity also contributes to the UHI. Such activities include the operation of automobiles and various forms of industry.

4. *Evapotranspiration Effects:* The energy balance is also affected by the lack of vegetation and standing water in urban areas, which inhibits cooling by evapotranspiration.

5. *Green House Gas emission:* High levels of pollution in urban areas can also increase the UHI, as many forms of pollution can create a local greenhouse effect.

6. *Immediate Surrounding:* Presence of mountains, ocean, big water bodies can also minimise or exacerbate the intensity of UHI

7. *Aerosols and pollutants:* These also affect the longwave radiation balance, due to increased absorption, and supply extra cloud condensation nuclei around which cloud droplets may form (Oke (1973)).

1.2.2 Consequence of UHI

The Urban Heat Island can affect an urban population in the following ways:

1. *Energy demand:* Higher urban temperatures may increase or decrease energy demands for the space conditioning of buildings, depending on whether the corresponding climate is heating or cooling dominated.

2. *Affects the air quality:* Changes in energy consumption, have an impact on local pollutant production due to combustion of fossil fuels. The emission of pollutants from more distant power plants, including sulfur dioxide, carbon monoxide, nitrous oxides and suspended particulates, may also be altered.

3. *Change in the pattern of precipitation:* As a result of the urban heat island effect, monthly rainfall can be 28% greater between 20-40 miles downwind

of cities (Shepherd and Mehta (2002), Shepherd (2005), Hand and Shepherd (2009))

4. *Uncomfortable urban climate:* UHIs have the potential to directly influence the health and welfare of urban residents. As UHIs are characterized by increased temperature, they can potentially increase the magnitude and duration of heat waves within cities. The nighttime effect of UHIs (discussed below) can be particularly harmful during a heat wave, as it deprives urban residents of the cool relief found in rural areas during the night.

5. Aside from the obvious effect on temperature, UHIs can produce secondary effects on local meteorology, including the altering of local wind patterns, the development of clouds and fog, the number of lightning strikes, and the rates of precipitation. On a positive note they may also increase the duration of the growing seasons.

1.2.3 Case Study: London

An exhaustive study to understand the nature of UHI was conducted in London. We here present the result from the field measurements. In Figure 1.2(a) one can see that the UHI intensity ranges from $-2.5C$ to $7.5C$ although most of the time the intensity hovered around $1.5C$. In Figure 1.2(b) one can see the difference between the city center and its rural counterpart. Diamonds represent the measured UHI at different test sites spread across London city center while the dark line represents the average of the UHI intensity. One can clearly see that in case of London the average UHI intensity is always positive although at certain site it was negative during the day. Figure 1.2(c) gives the variation of the UHI intensity as a function of the radial distance. Quite expectedly it decreases with distance from the center. Finally, Figure 1.2(d) gives the UHI intensity as a function of wind speed. Higher wind speed increases advective heat removal from the city and also increases turbulent mixing and hence enhances heat transfer, resulting in a lower temperature. Also it was observed that the temperature contours were shifted in
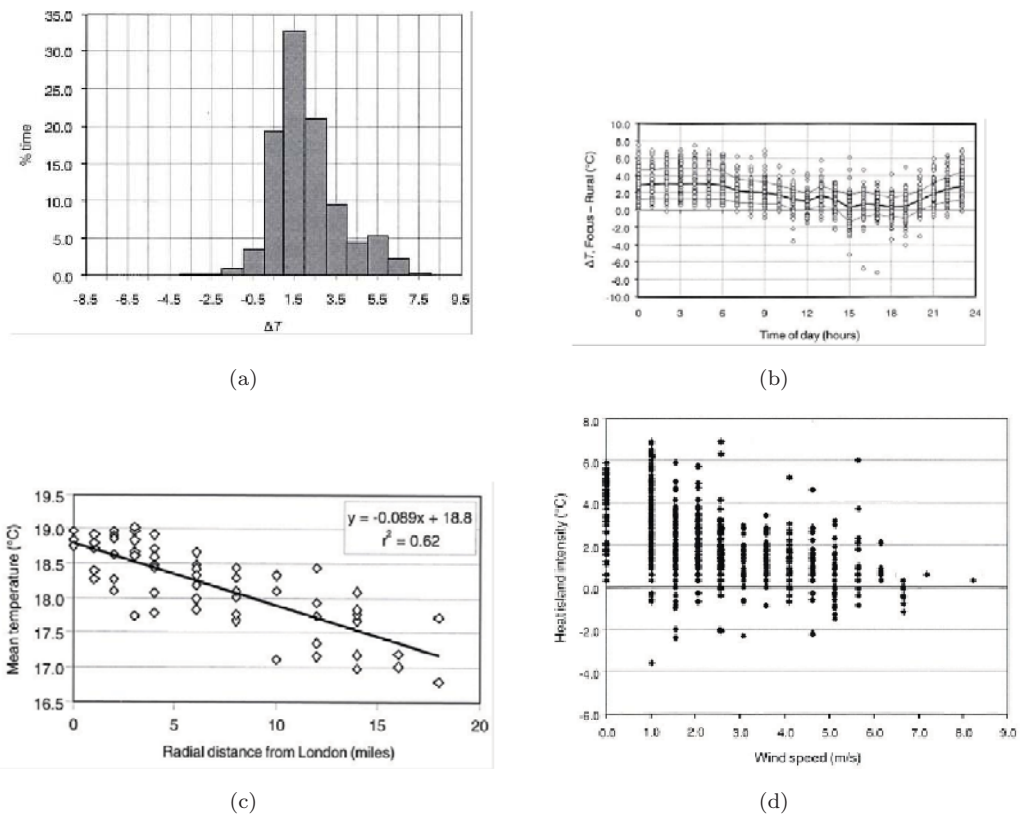
FIGURE 1.2: London Urban Heat Island Measurement Ref:(Graves et al. (2001))

the mean wind direction. More details on the study of UHI in London can be found in Graves et al. (2001).

1.2.4 Diurnal Behavior of UHI

Though the air temperature UHI is generally most apparent at night, urban heat islands exhibit significant and somewhat paradoxical diurnal behavior. The air temperature UHI is large at night and small during the day, while the opposite is true for the surface temperature UHI. Throughout the daytime, particularly when the skies are free of clouds, urban surfaces are warmed by the absorption of solar radiation. As described above, the surfaces in the urban areas tend to warm faster than those of the surrounding rural areas. By virtue of their high heat capacities, these urban surfaces act as a giant reservoir of heat energy. However, as is often the case with daytime heating, this warming also has the effect of

generating convective winds within the urban boundary layer. It is theorized that, due to the atmospheric mixing that results, the air temperature UHI is generally minimal or nonexistent during the day, though the surface temperatures can reach extremely high levels. At night, however, the situation reverses. The absence of solar heating causes the atmospheric convection to decrease, and the urban boundary layer begins to stabilize. If enough stabilization occurs, an inversion layer is formed. This traps the urban air near the surface, and allows it to heat from the still-warm urban surfaces, forming the nighttime air temperature UHI. The explanation for the night-time maximum is that the principal cause of UHI is blocking of "sky view" during cooling: surfaces lose heat at night principally by radiation to the (comparatively cold) sky, and this is blocked by the buildings in an urban area. Radiative cooling is more dominant when wind speed is low and the sky is cloudless, and indeed the UHI is found to be largest at night in these conditions as will be presented in the results of some research work in the following chapters.

Different climatic regions may have very different experiences of UHIs. In an already warm area they will be unwelcome, in a cold area they might be beneficial. Some cities exhibit a heat island effect, largest at night and particularly in summer while for some cities especially those which are closer to a large water body don't show much difference between the night and day time UHI. The results from some research works have been presented in the following sections.

1.3   Structure of Thesis

Starting with a brief presentation of the theory behind fluid flow modeling in chapter 2, the two most important problems associated with atmospheric modeling namely that of turbulence and spatio-temporal scales are discussed. Since computationally these problems can't be handled in a single model, the concept of Multiscale Modeling is introduced. Since one of the main aims of this work was to develop a tool to study urban-atmospheric interactions, a detailed study was

conducted to understand the flow around bluff bodies. The findings of this work are presented in Chapter 4. These results are then used to develop a new urban canopy model presented in Chapter 5. Since, this new model can only be implemented for a simplified geometry of repeated cuboids the concept of "Equivalent Geometry" is introduced in Chapter 6. Finally, the different modeling concepts are brought together and applied to a real city. Some initial city planning guidelines are presented in Chapter 7 for this city. Conclusions and future research needs in this field are finally presented in Chapter 8.

Chapter 2

Multiscale Modeling Approach

We encounter fluid flow in our life very frequently. Common examples of such flow can range from the blood flow in our blood vessels to the flow of air over electronic circuits for cooling purpose. Atmospheric flows although experienced at a much larger scale are no exceptions to these. It is quite amazing to know that all these seemingly different flows are governed by the same set of equations. In the next section we present in brief these equations along with the problems associated with different types of solutions strategies.

2.1 Governing Equations

The general equations describing the fluid flow in the atmosphere can be represented by the following set of equations.

2.1.1 Mass Conservation Equation

For any compressible fluid the principle of conservation of mass can be mathematically represented by the following equation.

$$\frac{\partial \rho}{\partial t} + \vec{\nabla}.(\rho \vec{u}) = 0 \tag{2.1}$$

2.1.2 Momentum Conservation Equation

Similarly the principle of conservation of momentum can be mathematically represented by the following equation.

$$\rho \left(\frac{\partial \vec{u}}{\partial t} + \vec{u} \cdot \nabla \vec{u} \right) = -\vec{\nabla} p + \mu \nabla^2 \vec{u} + \vec{f} \tag{2.2}$$

2.1.3 Energy Conservation Equation

Following the law of conservation of energy we write the following equation

$$\rho \left(\frac{\partial C_p T}{\partial t} + \vec{u} \cdot \vec{\nabla} T \right) = \mu \nabla^2 T + Q_T \tag{2.3}$$

In the above equations the terms $\vec{f}$ and Q_T can be looked upon as the sources or sinks of momentum and energy. More information about these terms will be furnished as and when required in later chapters.

2.2 Fluid flow modeling

There are three fundamental methods of simulating mesoscale atmospheric flows: physical, analytical and numerical models. With the first technique, scale model replicas of observed ground surface characteristics (e.g., topographic relief, buildings) are constructed and inserted into a chamber such as a wind tunnel (water

tanks are also used). The flow of air or other gases or liquids in this chamber is adjusted so as to best represent the larger-scale observed atmospheric conditions. Analytical modeling, in contrast, utilizes such basic analysis techniques as algebra and calculus to solve directly all or a subset of Equations 2.1 to 2.3 for constrained cases. The third approach, Numerical Modeling, is the most flexible of them all and can be used to simulate complex fluid flow. The following subsections describe them in a little more detail.

2.2.1   Physical Modeling

Physical Modeling involves conducting experiments in wind tunnels on a scaled down model (in our case: a city). This calls for some physical modeling criteria (popularly known as similarity criteria) to be satisfied. These similarity criteria are derived by writing the governing flow equations for the city and the scaled down model. Both these sets of equations are then non-dimensionalized using the characteristic length, velocity and temperature scales of the city and the model. These two sets of non-dimensionalised equations will be identical when the coefficients of each term of these two sets of equations match. These coefficients are known as the Reynolds Number, Froud Number, Richardson Number, Prandtle Number, Eckert Number, Rossby Number and the Schidmt Number. Matching these numbers ensures that the results from the experiment is independent of the scale of the model. Complete similarity of the flow requires, in addition to matching the foregoing parameters for the small and full scale system, similarity of the external boundary conditions. These external conditions include the distribution of surface temperature, the turbulence characteristics above the atmospheric boundary layer, the surface roughness and that there should be no pressure gradient in the mean flow direction. Of these it is almost impossible to have control over the first two. For sloping or irregular ground surfaces a geometrically similar topographical model is required to match the roughness and the modeled upwind fetch must be sufficiently long as to ensure that flow approaching the modeled urban area is in

equilibrium with the upwind boundary conditions to minimize the upwind pressure gradient. With all these requirements, physical modeling has been primarily limited to stably stratified flows over regular terrains. Even in this case, however, such observed features of the real atmosphere as the veering of winds with height and buoyancy driven flow, cannot be satisfactorily reproduced. Thus the possibility of using a physical model to understand the urban heat island doesn't appear to be feasible.

2.2.2 Analytical Modeling

The system of equations presented in Section 2.1 is a set of nonlinear partial differential equations. The non linear characters of the equations occur because products of the dependent variables are included in the relationships. To obtain exact solutions to the conservation relationships, it is necessary to remove the nonlinearities in the equations, which results after making considerable simplifications which rarely occur in reality. Nevertheless, results from such simplified, linear equations are useful for the following reasons:

1. The exact solutions of the simplified linear differential equations give some idea as to the physical mechanisms involved in specific atmospheric circulations. Because exact solutions are obtained, an investigator can be certain that the results are not caused by computational errors, as can be true with numerical models.

2. Results from these linearized equations can be contrasted with those obtained from a numerical model in which the magnitude of the nonlinear terms is small relative to the linear terms. An accurate nonlinear numerical model would give good agreement with the linear results when the products of the dependent variables are small. Linear representations of the conservation relations have been used to investigate wave motions in the atmosphere, as well as to represent actual mesoscale circulations. Kurihara (1976), for

example, applied a linear analysis to investigate spiral bands in a tropical storm. Klemp and Lilly (1975) used such an approach to study wave dynamics in downslope wind storms to the lee of large mountain barriers. Other linear models of airflow over mountain barriers include the model of Wang and Lin (1999). Similar approach have also been made by the building physics community to develop a model for predicting the temperature in an urban canopy. However, the complex nature of the non linearities involved in real atmospheric phenomenon doesn't allow any simplification to be made to reduce the governing equations to a solvable form, thus the possibility of developing an elegant analytical model of the urban climate is very remote.

2.2.3 Numerical Modeling

Because of the aforementioned shortfalls of the Physical and Analytical Modeling we choose a third approach in which the equations are solved numerically on a computer. The governing equations are discretized in time and space and solved using finite volume, finite element or a finite difference approach. A complete description of these methods can be found in Chung (2002). The equations when solved numerically with appropriate boundary conditions can be used to compute velocity, pressure and temperature profiles on a predefined numerical grid.

2.3 Problems in Urban Climate Modeling

The main complexities in atmospheric flow modeling arise due to the chaotic nature of turbulence and the presence of a large variety of spatio-temporal scales. These are explained in detail in the following sub-sections.

2.3.1 Turbulence Modeling

In fluid dynamics, turbulence or turbulent flow is a fluid regime characterized by chaotic, stochastic property changes. This includes high momentum convection, and rapid variation of pressure and velocity in space and time. Turbulence causes the formation of eddies of many different length scales. Most of the kinetic energy of the turbulent motion is contained in large scale structures. This energy "cascades" from these large scale structures to smaller scale structures by an inertial and essentially inviscid mechanism. This process continues, creating smaller and smaller structures which produces a hierarchy of eddies. Eventually, this process creates structures that are small enough so that molecular diffusion becomes important and viscous dissipation of energy finally takes place. The scale at which this happens is the Kolmogorov length scale. Important features of turbulence can be enumerated as:

- Turbulence is irregular and seemingly random (chaotic). Statistical methods should be used for extracting useful engineering information.

- Turbulence is highly diffusive. Rapid mixing significantly increases momentum, heat, and mass transfer.

- Turbulence is a rotational and three-dimensional motion.

- Turbulence is associated with high levels of vorticity fluctuation. Smaller scales are generated by the vortex stretching mechanism.

- Turbulence is highly dissipative. It needs a source of energy to be maintained.

- Turbulence is a continuum phenomenon. The smallest scale of turbulence is much larger than the molecular scales in most engineering applications.

- Turbulence is a manifestation of flow and not of the fluid.
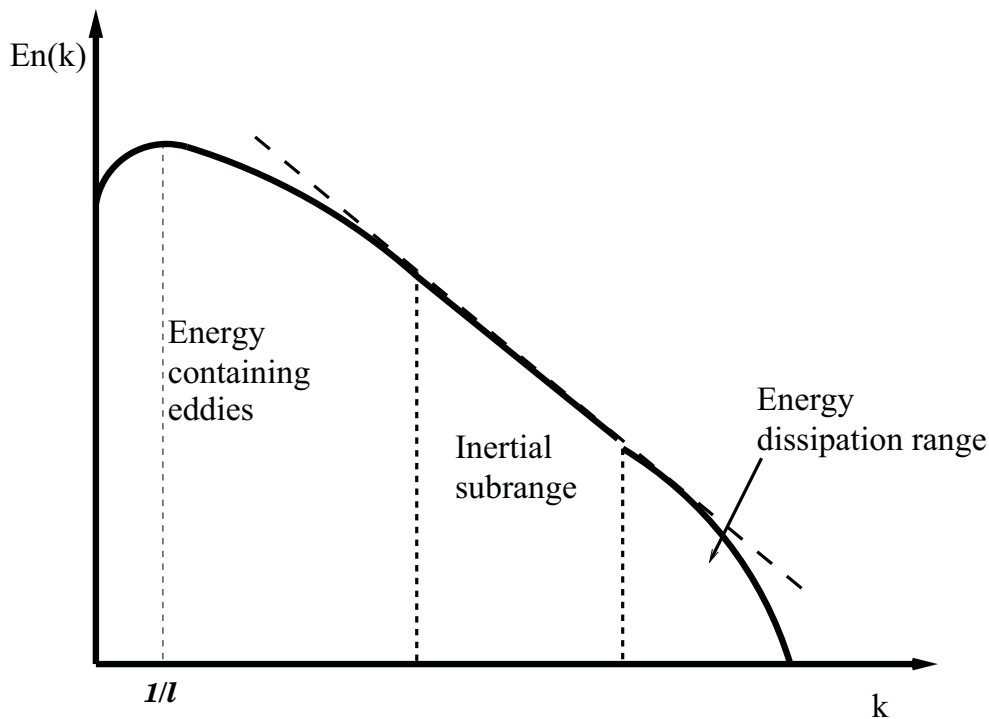
FIGURE 2.1: Energy spectrum vs. wave number space (log-log scale)

2.3.1.1 Spectral Analysis

Turbulence has a wide range of length (time) scales. A typical energy spectrum (Fourier decomposition of energy) is shown in Figure 2.1. Here En_k is the energy spectrum and k is the wavenumber (the inverse of wavelength $(1/\ell)$). Fluctuation energy is produced at the large eddies (with low wave numbers). A Vortex stretching mechanism then generates smaller and smaller eddies and energy flows down the spectrum to the high wave number region. The energy is mainly dissipated into heat at the smallest eddies (of the Kolmogorov scales). Depending upon the production and dissipation of turbulent kinetic energy the spectrum can be divided into the Energy containing range, the Inertial subrange and the Dissipation subrange.

Energy containing range: This is the range of large scale eddies, which contain most of the energy. At this scale, energy is converted from the mean flow into Turbulent Kinetic Energy (TKE). The forcing mechanisms that extract TKE

from the mean flow are shear, buoyancy and potentially pressure perturbations (which may produce TKE in smaller ranges, see McBean and Elliott (1975)). The energy containing range is dominated by the integral length scale ℓ. $En(k)$ reaches its maximum at a wavenumber roughly corresponding to this Eulerian integral length scale.

Inertial subrange: This is the range of wavenumber that are smaller than the smallest energy input ($\approx 10^1 m$) but larger than the Kolmogorov microscale λ_K ($\approx 10^{-3} m$). In this range, TKE is neither produced nor dissipated. Eddies do not interact with the mean flow anymore, and turbulence at this scale is statistically uncorrelated to the mean flow. It is isotropic and does not contribute to turbulent flux densities. Energy is passed down from larger scales to smaller ones, and according to Kolmogorov (1941) the inertial subrange is characterized by a straight line, known as Kolmogorov's $-5/3$ law:

$$En(k) = \alpha \epsilon^{2/3} k^{-5/3} \tag{2.4}$$

where α is a constant.

Dissipation subrange: In the dissipation subrange, TKE is transformed by dissipation into heat. Dissipation of TKE starts roughly at wavenumber that are smaller than the Kolmogorov microscale λ_K

$$\lambda_K = \left(\frac{\nu^3}{\epsilon} \right)^{1/4} \tag{2.5}$$

where ν is the kinematic molecular viscosity and ϵ the dissipation rate of TKE. With ultrasonic anemometers, this part of the spectra can not be measured directly, because the frequency response of these instruments is too slow and the measurement volume is too large. Indirectly, dissipation can be calculated from the inertial subrange slope.

2.3.1.2 Reynolds Decomposition

Reynolds decomposition splits any instantaneous variable $a(x,t)$ at a given location and time t into resolved mean value (denoted by on overhead bar) and an unresolved fluctuating part (denoted by a prime).

$$a = \bar{a} + a^{'} \tag{2.6}$$

Commonly, the splitting is done in the time domain with $\bar{a}$, the temporal average over an averaging time T_a, which fulfils the assumption of (i) stationarity and (ii) the condition that T_a lies in the region of the spectral gap:

$$\bar{a} = \frac{1}{T_a} \int_{t=0}^{T_a} a(t)dt \tag{2.7}$$

The condition of stationarity, which results in $\partial/\partial t = 0$, is seldom fulfilled, since superscale forcing (eg. inactive turbulence, diurnal and synoptic effects) results in continuously changing boundary conditions. For the same reason, the presence of the spectral gap, which theoretically results from an energetic separation of the energy input at the synoptic scale and the energy produced at the turbulent scale (Oke (1988)) is in doubt.

2.3.1.3 Turbulence Models

The problem of turbulence may be solved to a greater or a lower extent using a turbulence model. All of the existing turbulence models lie in one of the three categories DNS, LES or RANS.

DNS In Direct Numerical Simulation (DNS), the Navier Stokes system of equations is solved directly with refined meshes capable of resolving all turbulence length scales including the Kolmogorov microscales,

$$\lambda_k = (\nu^3/\epsilon)^{1/4} \tag{2.8}$$

All turbulence scales ranging from the large energy-containing eddies to the dissipation scales, $0 \leq k\lambda_k \leq 1$ with k being the wave number must be resolved (Figure 2.1). To meet this requirement, the number of grid points required is proportional to $L/\lambda_k \approx Re^{3/4}$ where L is the characteristic length and Re is the Reynolds number, referenced to the integral scale of the flow. This leads to the number of grid points in 3-D being proportional to $Re^{9/4}$. Similarly the time step is limited by the Kolgomorov time scale, $\tau = (\nu/\epsilon)^{1/2}$, as

$$\delta t = \frac{0.003H}{u_T Re_T^1/2} \tag{2.9}$$

These restrictions are clearly too severe for DNS to be a practical tool in view of the currently available computing capacity.

LES Large Eddy Simulation (LES) is an alternative approach towards achieving our goal of more efficient turbulent flow calculations. Here, by using more refined meshes than are usually required for Reynolds Averaged Navier Stokes (RANS) system of equations (see below), large eddies are calculated (resolved) whereas the diffusion of small eddies are modeled. The rigor of LES in terms of performance and ability is somewhere between RANS and DNS. There are two major steps involved in LES analysis: filtering and subgrid modeling. Traditionally, filtering is carried out using the box function, Gaussian function or Fourier cut off function. Subgrid modeling includes the eddy viscosity model, the structure function model, the dynamic model, the scale similarity model and a mixed model among others. The LES approach will be discussed in detail in Chapter 4.

RANS Reynolds-Averaged Navier-Stokes (RANS) equations are the conventional approach to turbulence modeling. An ensemble version of the governing equations is solved, which introduces new apparent stresses known as Reynolds stresses resulting in more number of unknowns than equations. This problem is known as the problem of closure. This adds a second order tensor of unknowns for which various models can provide different levels of closure. It is a common

misconception that the RANS equations do not apply to flows with a time-varying mean flow because these equations are 'time-averaged'. In fact, statistically unsteady (or non-stationary) flows can equally be treated. This is sometimes referred to as URANS. There is nothing inherent in Reynolds averaging to preclude this, but the turbulence models used to close the equations are valid only as long as the time scale of these changes in the mean is large compared to the time scales of the turbulent motion containing most of the energy.

2.3.2 Spatial and Temporal Scales

Other than turbulence there is also a problem of the spatial and temporal scales which influence urban climate modeling. Most atmospheric processes are limited to a certain time- and length- scale, which is reflected in the classification into global-, meso- and microscale processes. The overlapping between the chosen scale of interest and the scale of any physical process determines whether the process may be neglected, parameterized (empirically or physically) or directly solved in a model. It is obvious that all scales are interrelated. Kinetic energy is passed down from larger scales to smaller scales and is finally dissipated as heat. On the other hand, small scale processes in their quantity initiate and evolve larger structures and patterns. The classification into different scales is especially important for scale-dependent simplifications. The grid cell size of a particular model is limited to resolve only a certain level of detail, and thus has limited lower and upper resolution. Unresolved processes that are below the lower limit of the chosen scale are called subscale processes. In all applications concerning dispersion and transport processes in the atmospheric boundary layer, the unresolved processes are of essential importance. We try to parameterize the unresolved turbulent fluctuations by appropriate forcing at the resolved scale, which we have to identify first. Important subscale processes may be solved under certain closure assumptions or parameterizations. Unresolved processes that are above the upper limit of the chosen scale are called superscale processes. These may be handled by varying the boundary conditions (e.g. by model nesting). Britter and Hanna (2003) suggest

four conceptual ranges of length scales in the urban context: regional (up to 100 or 200km), city scale (up to 10 or 20km), neighborhood scale (up to 1 or 2km), and street canyon scale (less than 100 m). In fact, the atmospheric layer concept, the scale concept and also the typical duration of processes are all linked.

2.3.2.1 Street canyon scale

At the street canyon scale, detailed flow and dispersion within street canyons and around single buildings or intersections are addressed. The nature of the urban roughness sublayer is a consequence of inhomogeneities at the street canyon scale. Practically, the street canyon scale is important in architecture (wind load), microscale dispersion and in air pollution applications. The flow at this scale can be directly modeled in CFD applications. When modeling at this scale, a detailed knowledge of the three-dimensional built structure is needed. A number of wind tunnel studies and a few field experiments have focused explicitly on processes at the street canyon scale. Nearly all surface measurements are carried out at this scale, even if their representativeness is interpreted at larger scales. However, it is worth mentioning that the flow characteristics inside the street canyons will also be affected by effects induced by the local neighborhood and not only by the structures surrounding the canyon.

2.3.2.2 Neighborhood scale

The neighborhood scale restores horizontal homogeneity of the surface at a larger scale by horizontal averaging over a homogeneous area of the city, large enough to filter out (repetitive) surface inhomogeneities at the street canyon scale. The formation of an inertial sublayer is a consequence of the (assumed) homogeneity at the neighborhood scale. The neighborhood scale is the preferred level of detail where urban Lagrangian near-field dispersion models are run (e.g. Rotach (2001); Hanna and Strimaitis (1993)). The restored horizontal homogeneity allows for

many simplifications, but also requires parameterizations in order to model underlying urban roughness and canopy sublayer. Finally, the neighborhood scale is also the scale of choice for flux monitoring sites.

2.3.2.3 City scale and regional scale

These scales focus on the modification of the whole boundary layer (mixed layer). This is of interest in mesoscale models, since today's models already include many grid cells that are 100% urban, and especially urban areas need appropriate predictions due to the high number of human activities. On the other hand, urban areas modify the whole boundary layer, its stability, thermodynamic properties, and the mixed layer height. The modified urban surface exchange results in typical urban climate phenomena like the urban heat island. At this scale, many processes in the urban roughness sublayer and the canopy sublayer are not of central importance anymore. There have been many attempts to simply alter the surface exchange parametrization of models to incorporate effects at the city scale eg. (Taha (1999)). The city or regional scale is currently reached by experimental mesoscale numerical models, and sophisticated urban canopy parameterizations have been developed (e.g. Masson (2000); Martilli and Rotach (2002); Otte et al. (2004)).

In the above we have discussed the spatial scales influencing urban climate modeling but different temporal scales may also be involved. For example there can be seasonal changes that take place over a few months and then there are gusts and hurricanes which can last for not more than a few seconds or minutes. For a robust simulation of the urban climate all of these scales should be taken into account.

2.4 Proposed solution: Multiscale Modeling

The last section explained briefly the different scales encountered in urban climate modeling. Unfortunately, it is not possible to satisfactorily resolve all of these scales in a computationally tractable way using a single model. It is however possible to tackle this problem by coupling different models with each targeting different climatic scales. For example a global model with a grid size of $200km - 300km$ may be coupled with a meso model having a grid resolution of $0.5km - 1km$, which itself may be coupled with a micro model with a resolution of $5 - 10m$. Here we describe one such approach.

Firstly, freely available results from a global-model are input to a meso-model at a slightly larger scale than that of the city in question. Then a meso-model is run as a pre-processor to interpolate the macro-scale results at progressively finer resolutions until the boundary conditions surrounding our city are resolved at a compatible resolution. Since the meso-scale model itself is used to interpolate the results to different grids, mass, momentum and energy conservation is automatically satisfied. It should be stressed that for the purpose of interpolation we assume a 100% rural surface in all the grids. The meso-model with subscale parametrization is then run in a normal way. In the rural context this may simply involve associating topography and average land use data with each cell, the former affecting temperature as pressure changes with height the latter affecting temperature due to evapo(transpir)ation from water bodies or vegetated surfaces. In the urban context however, it is important to account for the energy and momentum exchanges between the built surfaces and the adjacent air, which implies some representation of $3D$ geometry. For this we use a new urban canopy model in which the velocity, temperature and scalar profiles are parameterized as functions of built densities, street orientation and the dimensions of urban geometric typographies. These quantities are then used to estimate the sources and sinks of the momentum and energy equations. Even at the micro-scale the use of conventional computational fluid dynamics modeling is unattractive because of the
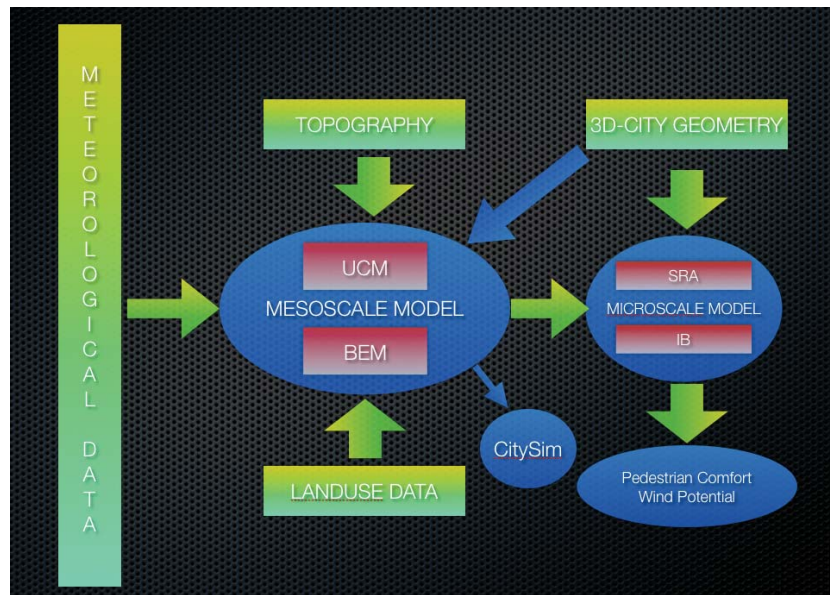
FIGURE 2.2: Multiscale Model: unidirectional arrows imply one way nesting

time involved in grid generation / tuning and the definition of boundary conditions. Furthermore, even the simplest geometry may require hundreds of millions of grid cells for a domain corresponding to a single meso-model cell, particularly if unstructured grids are used; which are attractive for productivity reasons but suffer from numerical instabilities. To overcome this problem we describe a new approach based on immersed boundaries in which the flow around any complex geometry can be computed using a simple Cartesian grid, so that users benefit from both improved productivity and accuracy.

Thus, a completely coupled global, meso and micro model (2.2) can be used to predict the temperature, wind and pressure field in a city taking into account not only the complex geometries of its built fabric but also the scales which are bigger than the city scale. Thus one can clearly see that the effects of superscales in any model is captured through the boundary conditions that are fed by a model handling bigger scales while the effects of subgrid scales are parametrized. For the mesoscale two such parameterizations have been developed an Urban Canopy Model (UCM) and a Building Energy Model (BEM). The result from such a Multiscale Model can be used either to evaluate pedestrian comfort or can be fed to an

urban resource flow modeling tool like CitySim Robinson et al. (2009) for studying the dynamics of a city in detail.

In this chapter the issues and importance of scales in urban climate prediction are explained. It became clear that it wasn't possible to handle all the spatio-temporal scales within a single modeling tool so we described a methodology to couple different modeling tools each capable of handling a particular range of scales. The different models in the Multiscale model will communicate with each other in two ways (feedback) however, it wasn't possible to address to this issue withing the scope of this project. Thus the Multiscale model that has been described is an example of a one way nested models. However, a new urban canopy model, immersed boundary technique, simplified radiosity algorithm and a novel approach to account for complex city geometry makes this approach the first of its kind.

Chapter 3

Model Description

The multiscale model as already explained in Chapter 2 consists of a Mesoscale Model (with UCM and BEM embedded in it) and a Microscale Model based on Immersed Surface Technique (IST). A Simplified Radiosity Algorithm (SRA) is used for the computation of radiation incident on wall, roof and ground surfaces. In this chapter we present these new techniques in an urban modeling context and evaluate their reliability for making urban climate predictions in a reasonable amount of time.

3.1 Mesoscale Model

The mesoscale model selected here, referred to as FVM (Finite Volume Model) was partly developed at the Soil and Air Pollution Laboratory of the Swiss Federal Institute of Technology Lausanne (Clappier et al. (1996)). In this model the following equations are solved:

3.1.1 Conservation of mass

$$\frac{\partial \rho}{\partial t} + \vec{\nabla}.(\rho \vec{v}) = 0 \qquad (3.1)$$

where $\vec{v}$ is the wind velocity and ρ the air density. On typical scales of velocity and length for the motion in the mesoscale range $\frac{\partial \rho}{\partial t}$ is much smaller than $\vec{\nabla}.(\rho\vec{v})$ and can therefore be neglected (anelastic approximation). Here, and in the following sections, variables are Reynolds averaged. Primed letters stand for their respective turbulent fluctuations.

Equations 3.3 to 3.4 hereafter have been written in advection form using the lagrangian time derivative for a more compact representation of the basic conservation laws. Because total mass is conserved, the rate of change of any mass-specific quantity ψ can be formulated by

$$\rho\frac{d\psi}{dt} = \frac{\partial(\rho\psi)}{\partial t} + \vec{\nabla}.(\rho\vec{v}\psi) \tag{3.2}$$

using the budget operator $\partial(\rho...)/\partial t + \vec{\nabla}.(\rho\vec{v}...)$. $\partial(\rho\psi)/\partial t$ can be interpreted as the storage of ψ and $\vec{\nabla}.(\rho\vec{v}\psi)$ as its mean transport (advection).

3.1.2 Conservation of Momentum

The conservation of momentum is expressed as follows:

$$\rho\frac{d\vec{v}}{dt} = -\vec{\nabla}\bar{p} + \rho\frac{\theta'}{\theta_o}\vec{g} - 2\vec{\Omega} \times (\vec{v} - \vec{v^G}) - \frac{\partial\overline{\rho v' v'_z}}{\partial z} + \vec{D_u} \tag{3.3}$$

in which p is the pressure, θ_o is the potential temperature of the reference state, $\theta' = \theta - \theta_o$ is the fluctuation relative to this state, $\vec{g}$ is the gravity acceleration, $\vec{\Omega}$ is the Earth's rotational angular velocity and $\vec{v^G}$ is the geostrophic wind velocity. The interpretation of the terms of equation 3.3 is the following:

Equation 3.3 is in the non-hydrostatic form and the buoyancy term is written using the Boussinesq approximation (see section 3.1.7.1).

$\vec{\nabla}\bar{p}$ pressure gradient force

$\rho\frac{\theta'}{\theta_o}\vec{g}$ vertical action of gravity (buoyancy)

$2\vec{\Omega}\times(\vec{v}-\vec{v^G})$ influence of the Earth's rotation (Coriolis effects)

$\frac{\partial\rho\overline{v'v'_z}}{\partial z}$ turbulent transport

$\vec{D}_u$ forces induced by interaction between solid surfaces and airflow

3.1.3   Conservation of Energy

The conservation of energy is expressed as follows:

$$\rho\frac{d\theta}{dt} = -\frac{\partial\rho\overline{v'_z\theta}}{\partial z} - \frac{1}{C_p}\left(\frac{p_o}{\bar{p}}\right)^{R/C_p}\frac{\partial R_{lw}}{\partial z} + D_\theta \tag{3.4}$$

where θ is potential temperature, C_p is the specific heat capacity at constant pressure of the air, R is the gas constant, p_o is the reference pressure (1000mb) and R_{lw} is the long wave radiation flux. D_θ denotes the impact of the sensible heat fluxes from the solid surfaces (ground or buildings) on the potential temperature budget. The interpretation of the various terms is as follows:

$\frac{\partial\rho\overline{v'_z\theta}}{\partial z}$ turbulent transport of heat

$\frac{1}{C_p}\left(\frac{p_o}{\bar{p}}\right)^{R/C_p}\frac{\partial R_{lw}}{\partial z}$ loss through long-wave emissions

D_θ the impact of sensible heat fluxes from solid surfaces on the potential temperature budget.

D-terms in Equations 3.3 and 3.4 arise from the consideration of urban elements, and are solved by the urban module presented later in Chapter 5.

3.1.4   Poisson Equation for Pressure

In the numerical resolution, the mass equation 3.1 is combined with the momentum equation 3.3 to yield the following Poisson differential equation for pressure:

$$\vec{\bigtriangledown}^2 \bar{p} = \bigtriangledown \cdot \vec{F} \tag{3.5}$$

with $\vec{F}$ defined as $(i = 1, 2, 3)$:

$$Fi = -\vec{\bigtriangledown} \cdot (\rho \vec{v} v_i) + \left[\rho \frac{\theta'}{\theta_o} \vec{g} - 2\vec{\Omega} \times (\vec{v} - v^{\vec{G}}) - \frac{\partial \overline{\rho v' v'_z}}{\partial z} + \vec{D}_u \right] \cdot \vec{e_i} \tag{3.6}$$

This Poisson equation actually expresses the propagation of acoustic waves through the domain. A study of orders of magnitude shows that this propagation is practically instantaneous. Equations 3.3 and 3.4 are solved explicitly, except for the pressure which is solved implicitly.

3.1.5   Turbulent Fluxes

Unfortunately, by introducing prognostic equations for the previously unknown second moments in Equations 2.2 and 2.3, we get new third-order terms in Equation 3.3 and 3.4, which we are still not able to predict. With each higher order set of equations, we have even more unknown terms than equations. This is called the closure problem. Practically, the process of continuously introducing new prognostic equations for even higher moments has to be stopped at a certain level of detail. Any turbulence closure scheme considers only a finite set of equations and approximates the missing higher order moments in terms of known moments. There are local and non-local closure schemes. Local closure schemes approximate any unknown parameter by known parameters at the same point in space. A common local scheme is the $K - theory$, which approximates turbulent transports with a transfer coefficient K_z, which is proportional to the local mean gradient as:

$$\overline{u_i a'} = -K_{zi} \frac{\partial \overline{a}}{\partial x_i} \tag{3.7}$$

where $\overline{a}$ is the mean part and a' the turbulent part of the variable that may be either the potential temperature or a velocity component depending on the equation to be solved and K_{zi} is the diffusion coefficient. The vertical-transfer coefficient K_{zi} is parameterized with a $k - l$ closure from Bougeault and Lacarre (1989). For that, the following prognostic equation for turbulent kinetic energy is solved:

$$\frac{\partial \rho e}{\partial t} + \frac{\partial \rho e u_j}{\partial x_j} + \frac{\partial \rho \overline{e' u_j'}}{\partial x_j} = -\overline{u_i' u_j'} \frac{\partial u_i}{\partial x_j} + g \frac{\overline{u_i' \theta'}}{\theta_o} \delta_{i3} - \frac{\rho C_\epsilon e^{3/2}}{l_\epsilon} + Q_e \tag{3.8}$$

The interpretation of the various terms in Equation 3.8 is as follows:

$\frac{\partial \rho e}{\partial t}$	time variation of tke
$\frac{\partial \rho e u_j}{\partial x_j}$	advection of tke
$\frac{\partial \rho \overline{e' u_j'}}{\partial x_j}$	turbulent transport of tke
$-\overline{u_i' u_j'} \frac{\partial u_i}{\partial x_j}$	shear production of tke
$g \frac{\overline{u_i' \theta'}}{\theta_o} \delta_{i3}$	buoyant production of tke
$\frac{\rho C_\epsilon e^{3/2}}{l_\epsilon}$	dissipation of tke
Q_e	sources / sinks of tke

The vertical diffusion coefficient can then be calculated using the following relation:

$$K_{zi} = c_i C_k l_k e^{1/2} \tag{3.9}$$

where c_i, C_k are numerical constants and l_k and l_ϵ are the turbulent and dissipative length scales and are computed as follows:

$$\int_{z}^{z+l_{up}} \beta(\theta(z) - \theta(z'))dz' = E(z) \tag{3.10}$$

$$\int_{z-l_{down}^{z}} \beta(\theta(z') - \theta(z))dz' = E(z) \tag{3.11}$$

$$l_{\epsilon} = (l_{up}l_{down})^{1/2} \tag{3.12}$$

$$l_k = min(l_{up}, l_{down}) \tag{3.13}$$

where, l_{up} and l_{down} refer to the distance that a parcel originating from level z, and having a TKE of the level $e(z)$ can travel upward and downward before being stopped by buoyancy effects. Close to the surface, the maximum value of l_{down} is limited by the height above the ground l_{ground}. In the standard mesoscale model, at the ground, turbulence fluxes of momentum and heat are computed using the Monin Obukonv Similarity Theory according to the formulation of Louis (1979). The solar radiation at the surface is computed using the formulation of Schayes (1982), including a specific aerosol absorption factor, variable earth-sun distance, dry air Rayleigh scattering and water vapor absorption. The longwave radiation flux is computed with the Sasamori (1999) scheme, which takes into account water vapor and carbon dioxide concentration in the atmosphere. The same formulation is used for the evaluation of the infrared flux divergence in equation 3.4. More detail regarding the shortwave and longwave modeling can be found in Martilli and Rotach (2002) and Krpo (2009). The shortwave radiation on the surfaces can now also be computed using the more accurate Simplified Radiosity Algorithm described later in this chapter, in Section 3.3

3.1.6 Mesoscale Grid
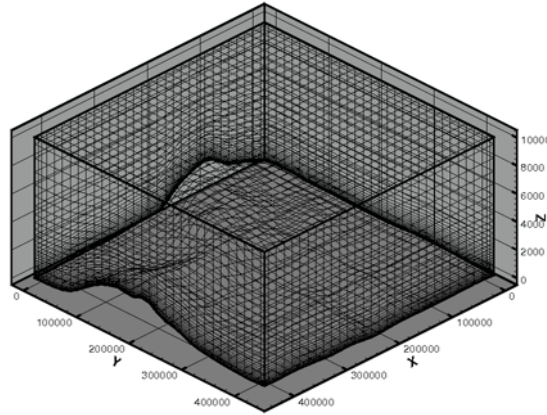
FIGURE 3.1: Terrain following mesh for mesoscale simulations

This mesoscale model uses a terrain-following (deformed) mesh (Figure 3.1) and is thus able to take into account the topography of the domain. The model is typically applied over areas of $200km$ by $200km$ horizontally and reaches up to heights of $10km$ above the earth's surface, so as to cover the entire troposphere. The volume thus defined is discretized to provide a horizontal resolution with cells of $1km$ to $5km$ and a vertical resolution of typically $10m$ close to the ground, where high accuracy is needed to $1000m$ at the top of the domain, near the tropopause.

3.1.7 Simplifying Hypotheses

3.1.7.1 Boussinesq Approximation

The Boussinesq approximation is applied in the field of buoyancy-driven flow. It states that density differences are sufficiently small to be neglected, except where they appear in terms multiplied by g, the acceleration due to gravity. The essence of the Boussinesq approximation is that the difference in inertia is negligible but gravity is sufficiently strong to make the specific weight appreciably different between the two fluids. The approximation's advantage arises because when considering a flow of, say warm and cold air of densities ρ_1 and ρ_2, one needs only

consider a single density ρ: the difference $\rho_1 - \rho_2$ is negligible. Dimensional analysis shows that, under these circumstances, the only sensible way that acceleration due to gravity g should enter into the equations of motion is in the reduced gravity g' where

$$g' = g\frac{\rho_1 - \rho_2}{\rho_1} \qquad (3.14)$$

Furthermore, neglecting the pressure variation in comparison to the potential temperature variation yields:

$$\frac{\rho_0 - \rho}{\rho_0} \approx \frac{\theta - \theta_0}{\theta_0} \qquad (3.15)$$

in which ρ_1 and ρ_2 have been replaced by ρ_0 (the density at hydrostatic state) and by ρ respectively. Equations 3.14 and 3.15 give rise to the buoyancy term in the momentum conservation equation 3.3.

3.1.7.2 Anelastic Approximation

The objective of the anelastic approximation is similar to that of Boussinesq approximation, but it can be applied to non-acoustic atmospheric motions. The key point of the approximation is dropping the time derivative term, in the continuity equation:

$$\frac{\partial \rho}{\partial t} \ll \vec{\nabla}.(\rho\vec{v}) \qquad (3.16)$$

This assumption also implies that the atmospheric fluid is incompressible.

3.1.8 Model Numerics

In the mesoscale model the mass, momentum, energy and turbulent kinetic energy conservation equations are solved using a Finite Volume Method (FVM). Advection of the aforementioned quantities is very important in such a model. This is

handled using a multiple order Crowley method (Crowly (1968)) with a Universal Limiter (Thuborn (1996)). As explained in Leveque (2002), this numerical scheme is very efficient as it leads to smaller diffusive errors and prevents non-physical oscillations. The algorithm has also been corrected for multidimensional applications (Clappier (1998)). For the complete resolution of the mesoscale problem, the Acoustic equation has been derived from the mass and momentum conservation laws and solved implicitly with a bi-conjugate gradient method, preconditioned in the vertical direction. The spatial discretization is based on a finite volume approach with the pressure gradients and the velocity fluxes estimated at the faces of the cells (finite volumes), while the velocity components, temperature, density, humidity and pressure are computed at the center. The model was tested for several well known problems to evaluate its efficiency and accuracy. The results can be found in Krpo (2009).

3.1.9 Urban Effects

Computation of the source terms of the mass momentum and energy equation is done using a new urban canopy model described in detail in Chapter 5.

3.2 Microscale Model

As already explained in the previous chapter, at microscale we intend to resolve the effects of buildings and hence we need a grid resolution fine enough to resolve the flow around buildings.

3.2.1 Mesh Generation

In Computational Fluid Dynamics the quality of mesh very often dictates the accuracy of the results and the computational time. A wisely chosen mesh can

(a) unstructured grid   (b) structured grid
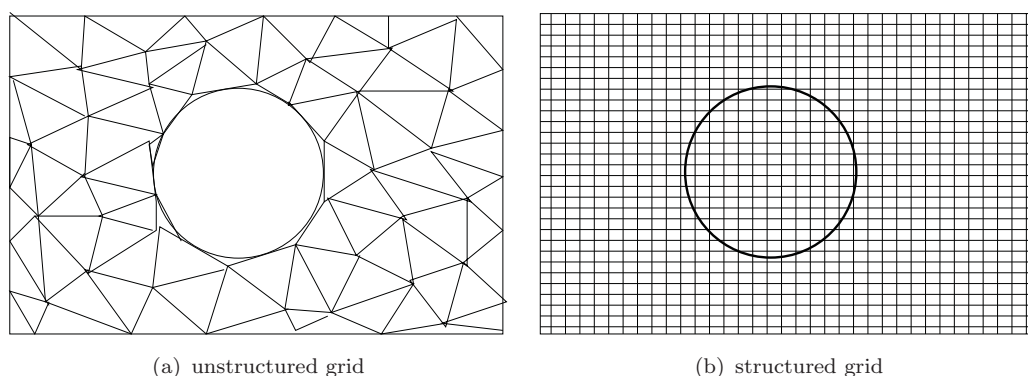
FIGURE 3.2: Different types of meshes

significantly improve the accuracy of the result without incurring any higher cost on computational resources. When it comes to choosing a grid for simulation one can choose a structured, unstructured or block structured grid. Structured grids (Figure 3.2(b)) are built with a repeating geometric and topological structure. They are usually formed from hexahedra or bricks. These grids are very simple to deal with, especially in terms of application development, computation and visualization. This simple structure often simplifies the computational connectivity of the grid, allowing for very efficient computation on modern computers. Block-structured grids are a collection of structured grids that together fill complex domains. They inherit most of the computational efficiency of a structured grid, but a difficulty is introduced of communication between the blocks. Nevertheless with the approach it is easier to grid a complicated geometry with a multi-block than a structured grid, but filling in complex geometry intersections and building blocks that properly share boundary surfaces usually requires a significant expertise and partially offsets the benefits of the multi-block approach. Unstructured grids (Figure 3.2(a)) are typically formed from simplexes such as tetrahedral. The fact that they have no repeating structure can make it very difficult to create and compute the necessary cell-to-cell connectivity required in CFD applications. The random orientation of an unstructured grid can also lead to awkward interfaces within the grid, possibly reducing the final accuracy of the solution. In summary then, the use of Cartesian structured grid not only provides simplicity in grid generation but also make available efficient algorithms for CFD simulations. This

is therefore our desired solution provided of course that we can fit this grid to the complex geometries found in real cities. For this we use a method called the Immersed Surface Technique.

(a)   (b)
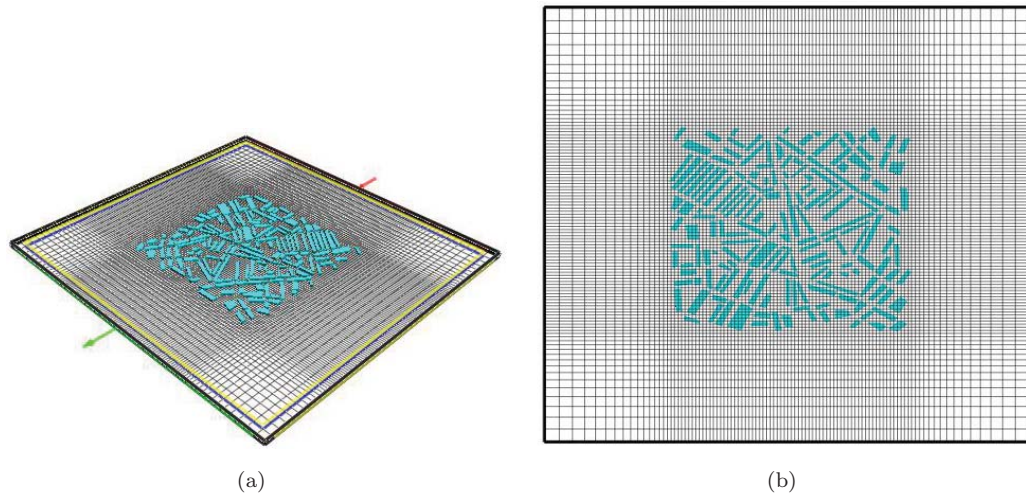
FIGURE 3.3: (a) Meshing of the geometry (Perspective view) (b) Meshing of the geometry (Aerial view)

3.2.2   Immersed Surface Technique

The term "Immersed Surface Technique" was first used in reference to a method developed by Peskin (1977) to simulate cardiac mechanics and associated blood flow. The distinguishing feature of this method was that the whole simulation was carried out on a Cartisean grid which didn't conform to the geometry of the heart and a novel procedure was formulated for imposing the effects of the immersed boundary on the flow.

To better understand the procedure let us take the example of a flow over a solid body. The conventional approach will be to employ structured or unstructured grids that conform the mesh to the region where the fluid will flow. Appropriate boundary conditions can then be applied on the body-fluid interface. If a finite difference method is employed on a structured grid, then the differential form of the governing equations is transformed to a curvilinear coordinate system aligned with the grid lines. Since, the grid conforms to the surface of the body, the

transformed equations can then be discretized in the computational domain with relative ease. If a finite volume technique is employed, then the integral form of the governing equations is discretized and the geometrical information regarding the grid is incorporated directly in the discretization. If an unstructured grid is employed, then either a finite volume or a finite element methodology can be used. Both approaches incorporate the local cell-geometry in to the discretization and do not resort to grid transformations. In this approach we use a nonbody conformal Cartesian grid in which the IS would still be represented through some means such as a surface grid, but the Cartesian volume will be generated with no regard to this surface grid. Thus the solid boundary would cut through the Cartesian volume grid. Because the grid doesn't conform to the solid boundary, incorporating the boundary conditions requires us to modify the equations in the vicinity of the boundary. Assuming that such a modification is possible (of course it is) the modified governing equations would then be discretized using a finite difference, finite volume or a finite element technique without resorting to coordinate transformation or complex discretization operators. When compared with unstructured grid methods, the Cartesian grid-based IST retains the advantage of being amenable to powerful line-iterative techniques and geometric multigrid methods, which can also lead to lower per-grid-point operation count. The primary advantage of the IST method is associated with the fact that the gird generation is greatly simplified. Generation of body-conformal structured or unstructured grids is time consuming and usually very cumbersome. The main aim in grid generation is to ensure maximum local resolution with a minimum number of total grid points and user intervention in setting-up the grid. For anything but simple geometries, these conflicting requirements can lead to deterioration in grid quality, which can negatively impact the accuracy and convergence properties of the solver. Furthermore, as the geometry becomes more complex the task of generating the grid becomes more and more difficult. The unstructured grid is better suited for complex geometries but even such grids are also affected by the complexity of the geometry. In contrast, for a simulation carried out on a nonbody conformal Cartesian grid, grid complexity and quality are not significantly affected by the complexity of the

geometry.

3.2.3 IST in an urban context

The new technique, as against the conventional CFD approach, offers us the possibility to simulate large domains. Construction of city geometry with a 3-D modeling tool is trivial and can be reasonably quick depending on the availability of existing data. Such geometries can be quickly converted into a STL (sterio lithography) file. These files have information about the solid-liquid interface (in our case building-atmosphere interface). The air flowing over the buildings are treated as phase one and the buildings are treated as phase two. The specific heat capacity, conductivity, density of the two phases can be specified for each building separately and the air. The amount of solar radiation as well as the anthropogenic heat generated due to human activities can be looked upon as heat sources which might vary with time. The methodology to compute the solar radiation is explained in the next section. The boundary condition of the velocity and temperature is forced through the interpolation of the results from the mesoscale simulations on to the microscale grid. Care is taken to impose a mass conservation over the full domain.

3.2.4 Mathematical Formulation

The immersed surface is represented on the fluid grid by a Level Set function (ϕ_s), where $\phi_s = 0$ represents the fluid-solid interface. ϕ_s is a signed distance function which is positive in the solid phase and negative in the fluid phase. The equations in the solid and fluid domain are combined using a smooth Heaviside function $H(\phi_s)$ which has value 1 in the fluid phase and 0 in the solid phase.

$$H(\phi_s) = \frac{1}{2}\left(1 - \tanh\left(\frac{2\phi_s}{\delta_{sf}}\right)\right) \tag{3.17}$$

where, δ_{sf} is the solid-fluid finite interface thickness.

The following equations are used for the solid phase:

$$\frac{\partial \rho^s}{\partial t} + \frac{\partial}{\partial x_j}(\rho^s u_j^s) = 0 \tag{3.18}$$

$$\frac{\partial \rho^s u_i^s}{\partial t} + \frac{\partial}{\partial x_j}(\rho^s u_i^s u_j^s) = 0 \tag{3.19}$$

For the case of non moving immersed surfaces, the solid phase velocity is set to zero (u_i^s=0). The standard Navier-Stokes equations are used for the fluid phase:

$$\frac{\partial \rho^f}{\partial t} + \frac{\partial}{\partial x_j}(\rho^f u_j^f) = 0 \tag{3.20}$$

$$\frac{\partial \rho^f u_i^f}{\partial t} + \frac{\partial}{\partial x_j}(\rho^f u_i^f u_j^f) = -\frac{\partial \rho^f}{\partial x_i} + \frac{\partial}{\partial x_j}\left(2u^f \frac{\partial S_{ij}^f}{\partial x_j}\right) + \rho^f g_i \tag{3.21}$$

Combining the solid and fluid equations into a single equation by multiplying the phase equations by the respective Heaviside functions and summing up, we obtain the following equations:

$$\frac{\partial \rho}{\partial t} + \frac{\partial}{\partial x_j}(\rho u_j) = 0 \tag{3.22}$$

$$\frac{\partial \rho u_i}{\partial t} + \frac{\partial}{\partial x_j}(\rho u_i u_j) = -\mathrm{H}(\phi_s)\frac{\partial \rho^f}{\partial x_i} + \frac{\partial}{\partial x_j}\left(2u\frac{\partial S_{ij}}{\partial x_j}\right) + \mathrm{H}(\phi_s)\rho^f g_i - 2u^f S_{ij}^f n_j \delta(\phi_s) \tag{3.23}$$

where, the composite quantities ρ and u_i are defined as

$$\rho = H\rho_f + (1 - H)\rho_s \tag{3.24}$$

$$\rho u_i = H\rho_f u_i^f + (1 - H)\rho_s u_i^s \tag{3.25}$$

the last term in the RHS is a viscous shear at the wall, where n_j is the normal to the fluid-solid interface and $\delta(\phi_s)$ is the Dirac delta function representing the location of the interface. The wall shear itself is modelled as Beckermann et al. (1999).

$$2\mu^f S_{ij}^f n_j = 2\mu^f \left(\frac{\rho}{\rho f} \right) u_i \delta(\phi_s) \qquad (3.26)$$

When used in combination with RANS turbulence modelling with wall functions, the wall shear is calculated using the logarithmic law of the wall.

3.2.5 Flow over a cube
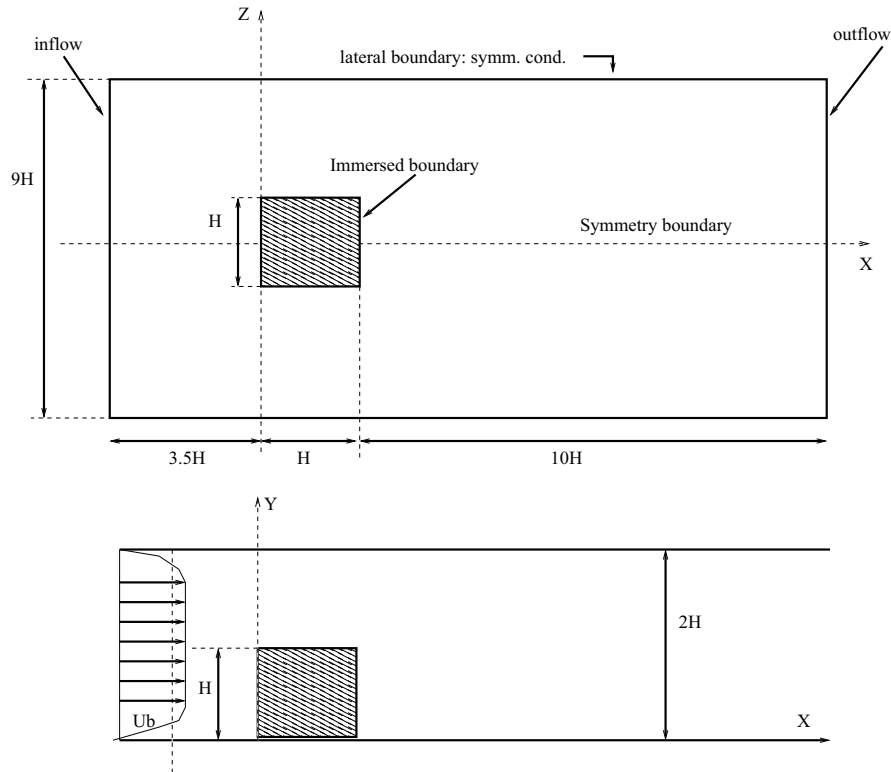
FIGURE 3.4: Flow over a cube: Simulation setup

3.2.5.1 Set-up

The test set-up consists of a cube of height H kept in a channel, as shown in Figure 3.4 The Reynolds number was $Re = U_b H/\nu = 40000$ based on the incoming

mean bulk velocity, U_b, and the obstacle height H. Even though the geometry of the flow configuration is rather simple, the flow is physically quite complex, with multiple separation regions and vortices. Martinuzzi and Tropea (1993) carried out flow visualization studies and detailed LDA measurements from which the mean velocity components and the various Reynolds stresses are available for this configuration. The on-coming turbulence intensity at roof height is relatively low ($T_u = u'^2/U_b \approx 0.03$). The present simulation set-up was borrowed from Lakehal and Rodi (1997) and Breuer et al. (1996). Earlier calculations of these authors using various grids (within the traditional blockdefined meshing) employed a $110 \times 32 \times 32$ grid for the standard $K - \epsilon$ model using wall functions. The width of the near-wall cell was set such as to correspond to $10 < y^+ < 25$. A similar grid was used for the new computations but this time using IST.

3.2.5.2 Validation results

Comparison of results from the IST simulations with the measurements of Martinuzzi and Tropea (1993) are presented as discussed below.

Figure 3.5 compares the streamlines in the plane of symmetry obtained by IST. It appears that the stagnation point is well simulated by the two techniques ($Y_s/H = 0.76$). However, the model predicts the separation point too close to the obstacle in comparison with the experiment. The location of the horse-shoe vortex center in front of the cube is also predicted to be further upstream.

Figures 3.6, 3.7, 3.8, 3.9, 3.10 and 3.11 compare the stream-wise velocity components at different values of x/H (-1.0, 0.5, 1, 1.5, 2.5 and 4) also on the symmetry plane. All U-velocity profiles agree well with the measurements at $x/H = -1.0$ upstream of the cube. As was to be expected from the streamlines, differences between the CFD results and the experiment can already be observed at a location at the middle of the cube ($x/H = 0.5$), as well as at the position of the back face of the cube ($x/H = 1.0$). At $x/H = 1.5$, the profiles predicted by the various models are rather similar and agree fairly well with the experiments in the region above

the roof height. Below this, the reverse flow velocity is under-predicted. Figures 3.12, 3.13 and 3.14 display three turbulent kinetic energy profiles in the symmetry plane at $x/H = 0.5, 1.0, 2.0$. At $x/H = 0.5$, the technique predicts fairly well the peak value of TKE, while near the backward edge of the cube, these values are under-predicted. In the region close to the flow reattachment point ($x/H = 1$ and 2), the TKE levels are under-predicted when compared with the experiments. This could partly be due to deficiencies of the eddy-viscosity concept but may again be largely caused by unsteady effects as the LES calculations produce higher levels in significantly better agreement with the measurements Breuer et al. (1996). From the above comparison it turns out that the IST produces results which are good enough for our purpose explained in chapter 6.
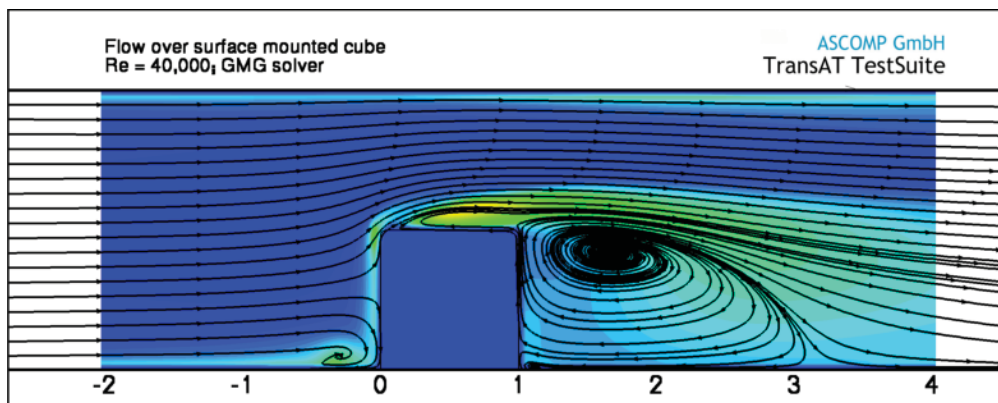
FIGURE 3.5: Streamlines and vectors and horse shoe vortex
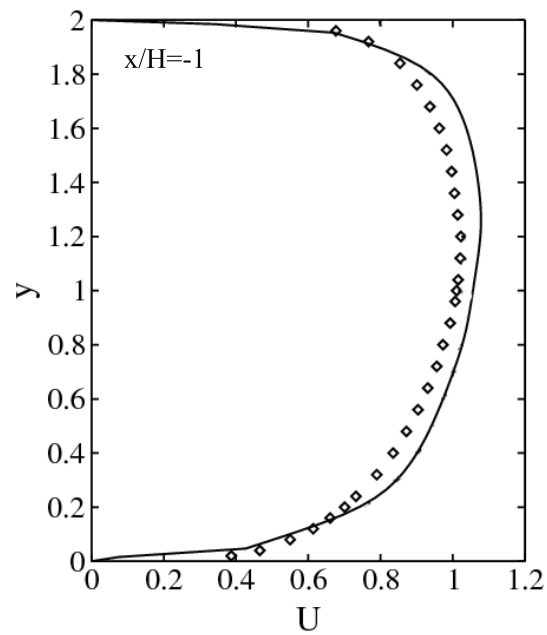
FIGURE 3.6: Comparison of mean streamwise velocity profile $U(m/s)$ in the symmetry plane at $x/H = -1.0$ in the vertical direction $Y(m)$ ($\Diamond$ represents experimental data)
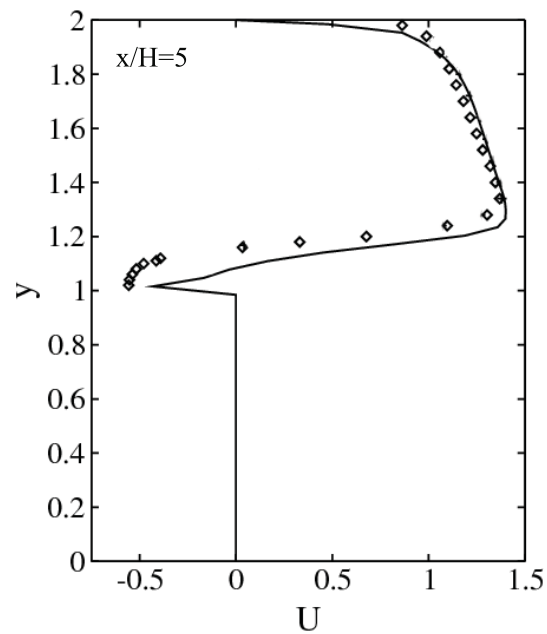
FIGURE 3.7: Comparison of mean streamwise velocity profile $U(m/s)$ in the symmetry plane at $x/H = 0.5$ in the vertical direction $Y(m)$ ($\Diamond$ represents experimental data)
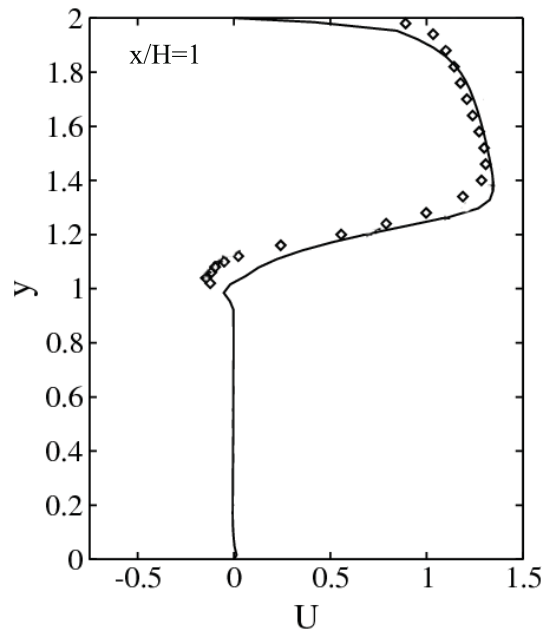
FIGURE 3.8: Comparison of mean streamwise velocity profile $U(m/s)$ in the symmetry plane at $x/H = 1.0$ in the vertical direction $Y(m)$ ($\Diamond$ represents experimental data)
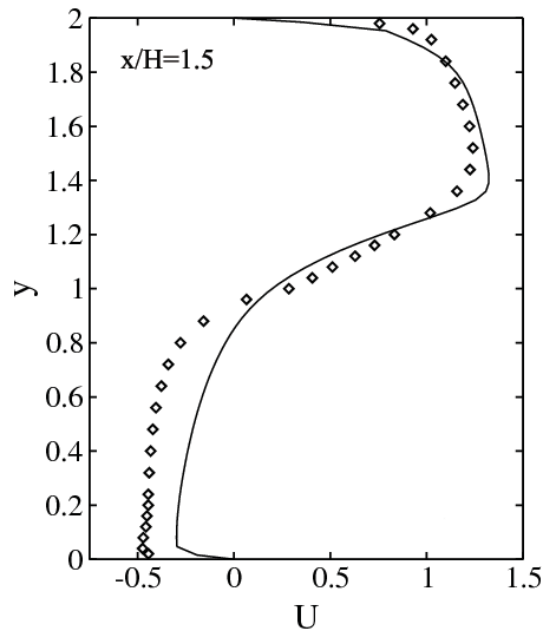
FIGURE 3.9: Comparison of mean streamwise velocity profile $U(m/s)$ in the symmetry plane at $x/H = 1.5$ in the vertical direction $Y(m)$ ($\Diamond$ represents experimental data)
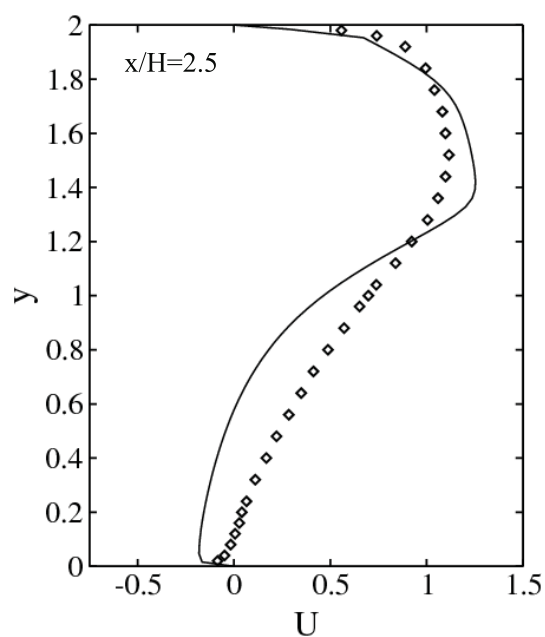
FIGURE 3.10: Comparison of mean streamwise velocity profile $U(m/s)$ in the symmetry plane at $x/H = 2.5$ in the vertical direction $Y(m)$ ($\Diamond$ represents experimental data)
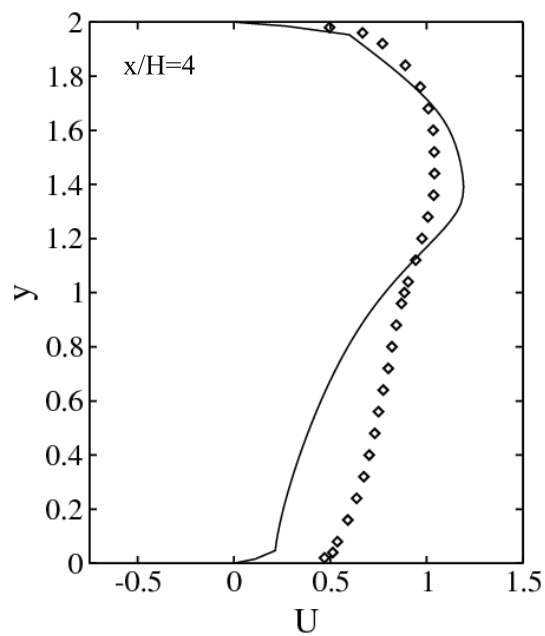
FIGURE 3.11: Comparison of mean streamwise velocity profile $U(m/s)$ in the symmetry plane at $x/H = 4.0$ in the vertical direction $Y(m)$ ($\Diamond$ represents experimental data)
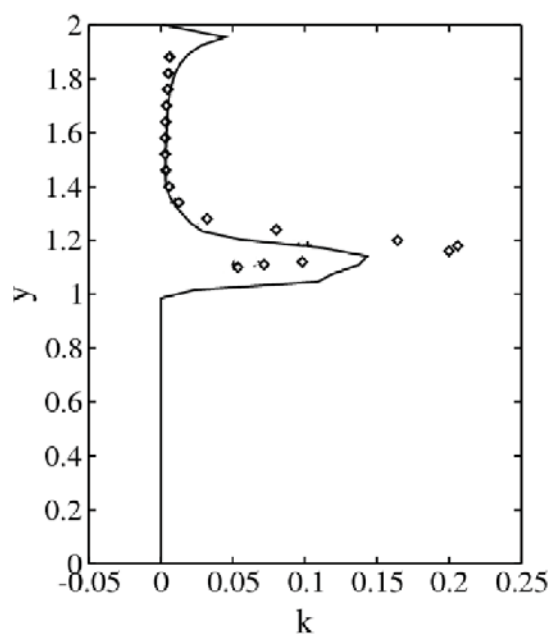
FIGURE 3.12: Comparison of mean turbulent kinetic energy profile (m^2/s^{-2}) in the symmetry plane at $x/H = 0.5$ in the vertical direction $Y(m)$ ($\Diamond$ represents experimental data)
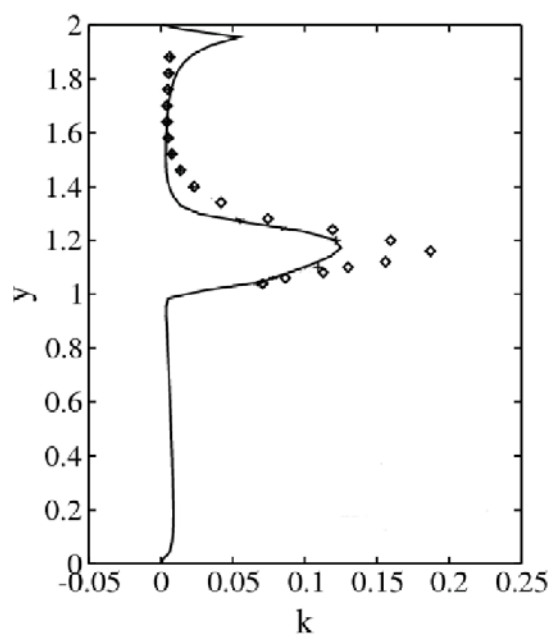
FIGURE 3.13: Comparison of mean turbulent kinetic energy profile (m^2/s^{-2}) in the symmetry plane at $x/H = 1.0$ in the vertical direction $Y(m)$ ($\Diamond$ represents experimental data)
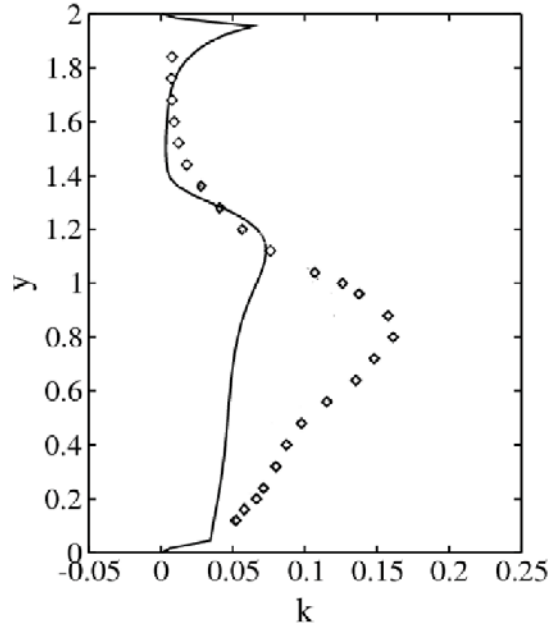
FIGURE 3.14: Comparison of mean turbulent kinetic energy profile (m^2/s^{-2}) in the symmetry plane at $x/H = 2.0$ in the vertical direction $Y(m)$ ($\Diamond$ represents experimental data)

3.3 Radiation Computation

The Simplified Radiosity Algorithm (SRA) of Robinson and Stone (2004) is used to solve for the shortwave irradiance incident on the surfaces defining our urban scene. For some set of $\widehat{p}$ sky patches, each of which subtends a solid angle Φ (Sr) and has radiance $\widehat{R}$ $(Wm^{-2}Sr^{-1})$ then, given the mean angle of incidence ζ (radians) between the patch and our receiving plane of slope β together with the proportion of the patch that can be seen $\widehat{\sigma}$ ($0 \leq \sigma \leq 1$), the direct sky irradiance (Wm^{-2}) is given by:

$$I_{d\beta} = \sum_{i=1}^{\widehat{p}} (\widehat{R}\Phi\sigma cos\zeta) \tag{3.27}$$

For this the well known discretization scheme due to Tregenza and Sharples (1993) is used to divide the sky vault into 145 patches of similar solid angle and the Perez

all weather model (Perez et al. (1993)) is used to calculate the radiance at the centroid of each of these patches. The direct beam irradiance $I_{b\beta}$ is calculated from the beam normal irradiance I_{bn} which is incident at an angle ζ to our surface of which some fraction ψ is visible from the sun, so that:

$$I_{b\beta} = I_{bn}\psi cos\zeta \tag{3.28}$$

Now the direct sky and beam irradiance contributes to a given surface's radiance $\widehat{R}$ which in turn influences the irradiance incident at other surfaces visible to it, so increasing their radiance and vice versa. To solve for this a similar equation to that used for the sky contribution gives the reflected diffuse irradiance. In this case two discretized vaults are used, one for above and one for below the horizontal plane, so that:

$$I_{b\beta} = \sum_{i=1}^{2\widehat{p}} (R^*\Phi\omega cos\zeta) \tag{3.29}$$

where ω is the proportion to the patch which is obstructed by urban (reflecting) surfaces and R^* is the radiance of the surface which dominates the obstruction to this patch (in other words, that which contributes the most to ω). As noted earlier, R^* depends on reflected diffuse irradiance as well as on the direct sky and beam irradiances. For this a set of simultaneous equations relating the beam and diffuse sky components to each surface's irradiance, which itself effects the reflected irradiance incident at other surfaces, may be formulated as a matrix and solved either iteratively or by matrix inversion (Robinson and Stone (2004)).

The principle complication in the above algorithm lies in determining the necessary view factors. For obstruction view factors, views encapsulating the hemisphere are rendered from each surface centroid, with every surface having a unique color. Each pixel is then translated into angular coordinates to identify the corresponding patch as well as the angle of incidence. For sky view factors then, $\Phi\sigma cos\zeta$ is treated as a single quantity obtained by numerical integration of $cos\zeta.d\Phi$ across each sky patch. Likewise for $\Phi\omega cos\zeta$, for which the dominant occluding surface is identified

as that which provides the greatest contribution. A similar process is repeated for solar visibility fractions for each surface, for which a constant size scene is rendered from the sun position.

3.3.1 Scene description and surface tesselization

The urban scene is sketched using NURBS (Non-Uniform Rational B-Splines) based 3-D modeling software: Rhinoceros. A two dimensional projection 3.15(a) of all the buildings are sketched using Google images as a rough guideline. A boolean operation is then conducted to remove the projection from the domain surface to get the ground surface 3.15(b). The 2-D building projections are then extruded and all the surfaces including the ground surfaces are discretized into small triangles as shown in the Figures 3.16(a), 3.16(b) and 3.17

(a) 2-D projections sketched from Google images   (b) Ground surfaces
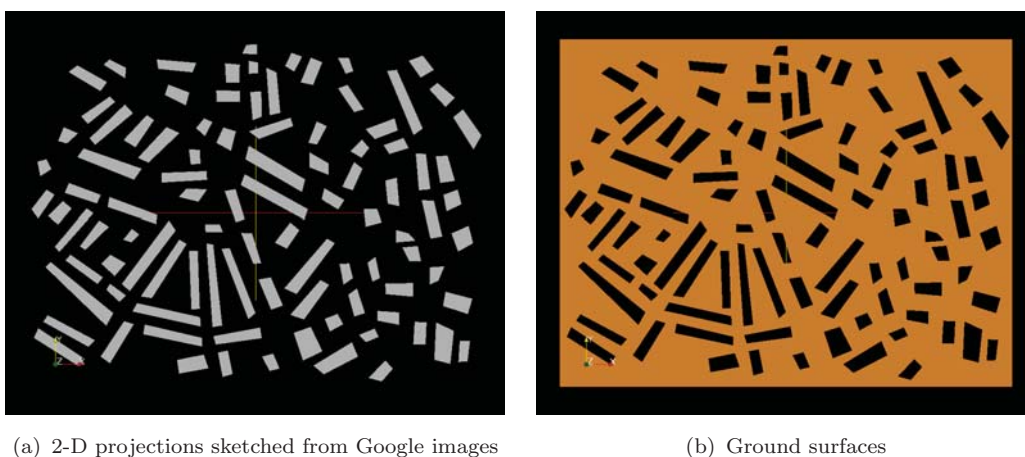
FIGURE 3.15: 2D projection of the buildings and the ground

The resulting geometry file is then exported in STL format which is converted to "rad" format to make it compatible with the SRA program.

Computation of radiation using the Simplified Radiosity Algorithm thus involves the following steps:

1. Description of sky

2. Division of sky vaults into 145 patches

(a) 2-D projections of the buildings (b) Ground surface
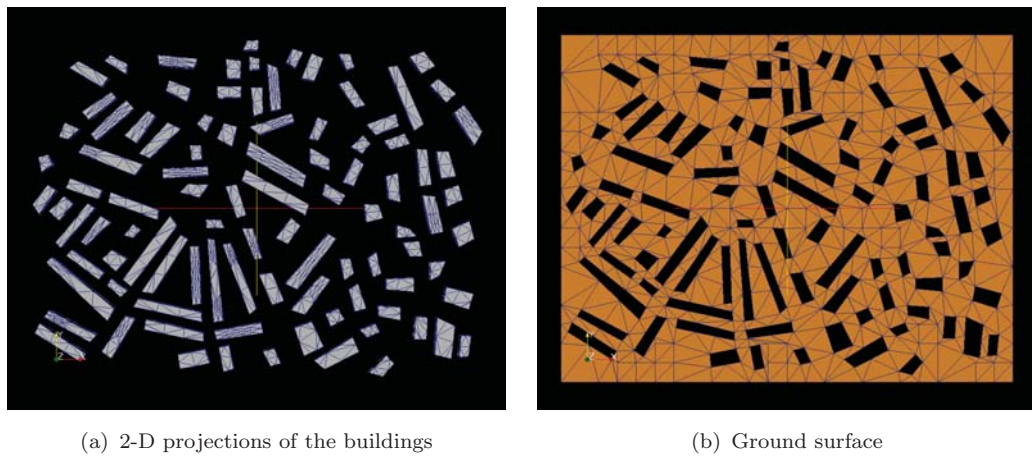
FIGURE 3.16: Tesselized surfaces
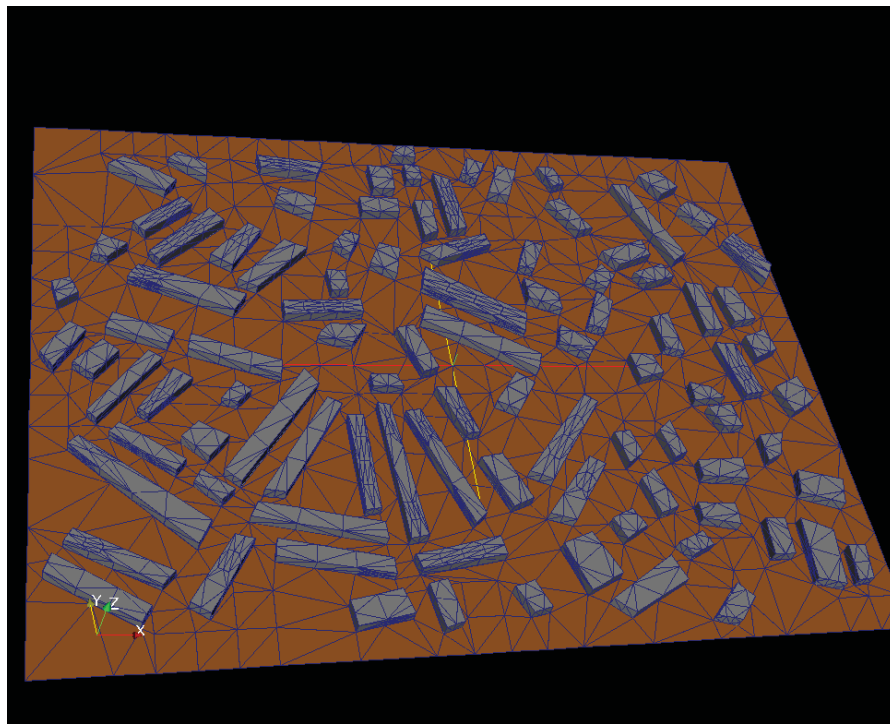
FIGURE 3.17: Meshed geometry

3. Geometrical description of the scene (including urban geometry and ground) and surface tesselization

4. Computation of view factors

5. Solving the matrix to obtain the shortwave and longwave radiation

3.3.2 Validation Results
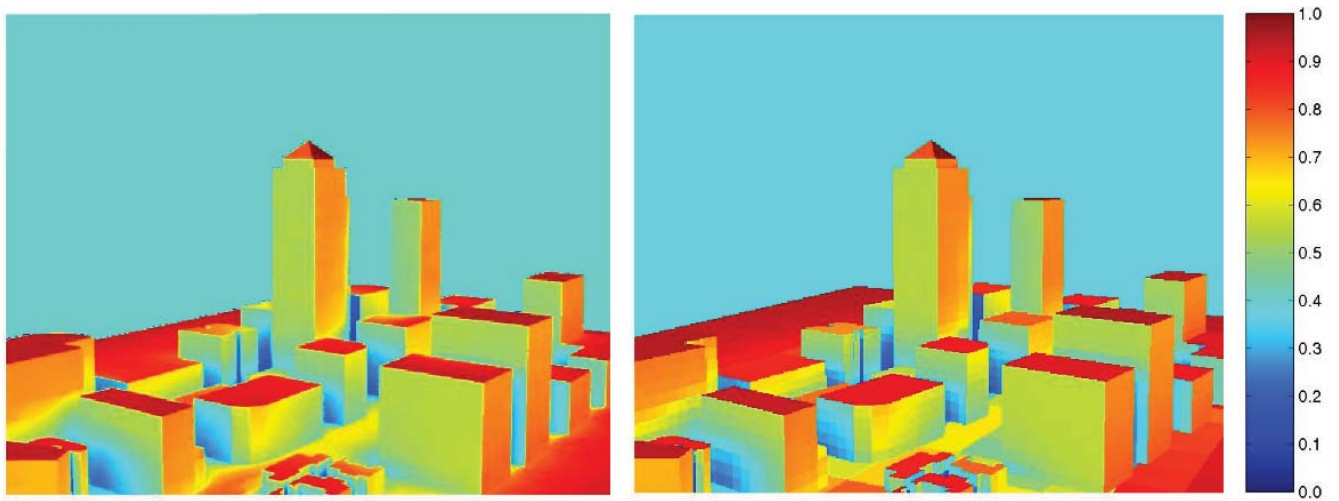
FIGURE 3.18: Predictions of annual solar irradiation (in MWh) throughout a simplified 3D model of Canary Wharf in London, UK from RADIANCE (left) and the SRA (right) (Robinson and Stone (2005))
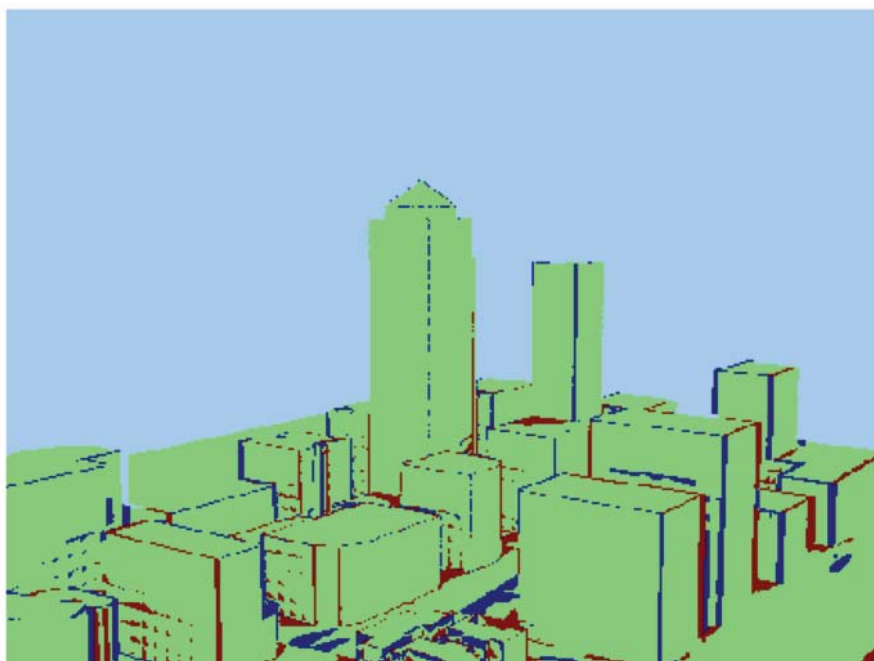
FIGURE 3.19: Difference between RADIANCE and SRA: Green corresponds to a difference of below 10% (Robinson and Stone (2005))

Figure 3.18 shows a comparison of annual shortwave irradiation computed by RA-DIANCE (left) and SRA (right). Figure 3.19 shows the difference between the values computed by the two models. It is clear from the figures that the SRA model computes the radiation within acceptable limits for our applications. More detail about the simulation and SRA can be found in (Robinson and Stone (2005)

3.4 Conclusion

In this chapter a detailed description of the Meso and Micro flow and radiation models was given. This included the description of the governing equations as well as the basic assumptions underlying these models. The Immersed Surface Technique and Simplified Radiosity Algorithm which are new to the Atmospheric community were introduced. Since these tools have been used extensively for developing parameterizations, their accuracy and efficiency was evaluated by making comparisons with wind tunnel data in the case of the IST and with simulations result from Radiance for the SRA (this latter by the model developers). The comparisons were found to be excellent, suggesting that these new techniques could be used with confidence in future work.

Chapter 4

Characterization of Flow around an array of cubes using Large Eddy Simulation

In the last chapters we gave an overview of the Multiscale Modeling approach adopted in this work. We also described the methodology for conducting a mesoscale simulation in some detail. In this it was apparent that the resolution of such models was too coarse to resolve the effects of cities (and buildings) and hence needed additional implicit representations of urban structures (UCM and BEM). To inform the development of such parameterizations it is important to have access to a sizable body of experimental (physical or numerical) results. So, as a starting point in the development of new urban canopy model we started with the standard assumption that a city can be represented by a regular array of cubes. With this assumption Large Eddy Simulations were conducted over an array of cubes for different inter-cubic spacings. The results obtained were then averaged over the simulation domain. This resulted in additional terms called dispersive fluxes. Until now these fluxes have been ignored in the development of urban parameterizations. However, the present study shows that these fluxes are as important as the turbulent fluxes and exhibit some strange trends. They can be either positive

or negative depending upon the inter-cube spacings. Furthermore, the profiles of the fluxes seem to have a close relationship with eddy formation inside the canopies. It is thus important that these fluxes be taken into account in the future development of a UCM.

4.1 Introduction

The large and continuous variety of scales present in the atmospheric flow over a city generates an intrinsic difficulty in the numerical treatment of the atmospheric conservation equations. From scaling considerations, the ratio between the smallest flow scale and the characteristic length scale is approximately proportional to $Re^{3/4}$ (Tennekes and Lumley (1972)), where Re is the Reynolds number. This means that a 3D representation of the planetary boundary layer resolving all scales will require about 10^{15} grid cells. This number is far from being handled conveniently nowadays or in the near future by any computing device. Therefore, the transport phenomena over larger distances (in our case covering a city and its bounding context) must be handled by mesoscale atmospheric codes with spatial resolutions of a few kilometers. As such these mesoscale codes cannot "see" buildings explicitly. Yet buildings and urban landuse significantly impact the micro and mesoscale flow, altering the wind, temperature and turbulence fields and radiation exchanges (Hosker (1984),Bornstein (1987)). Since, mesoscale numerical models do not have the spatial resolution to directly simulate the fluid dynamics and thermodynamics in and around urban structures, urban parameterizations are needed to approximate the drag, heating and enhanced turbulent kinetic energy (tke) produced and dissipated by the sub-grid scale urban elements. The drag forces offered by the buildings as well as the heat transfer characteristics are a function of the local velocity field. Local turbulent fluxes, dispersive fluxes (generally ignored in mesoscale models) and drag coefficients can significantly impact the exchange of mass, momentum and energy. However, a mesoscale code as described earlier, doesn't have the spatial resolution to generate the profiles of these

quantities. Several attempts have been made in the recent past to estimate the velocity profiles in the urban canopy. These so called "urban canopy models" are based on either single layer (Kusaka et al. (2001)) or multilayer considerations of the canopy (Kondo et al. (2005)). In almost all these models the dispersive fluxes which results from the averaging of the governing equation in the horizontal plane are either ignored or assumed to behave in the same way as the turbulent fluxes. However, recent work (Martilli and Santiago (2007),Santiago et al. (2007)) tends to confirm that these stresses can be significant and sometime comparable to the turbulent stresses themselves and may behave differently. However most of these findings were based on simulations conducted using Reynolds Averaged Navier Stokes (RANS) codes whose validity for this kind of application is somewhat questionable (Cheng et al. (2003)). Moreover, in the study we wanted to compare the magnitude of the dispersive fluxes and the turbulent fluxes. A RANS model only gives the modeled turbulent fluxes against which the dispersive fluxes can't be compared. In an attempt to resolve this issue we therefore employ an LES code which is capable of resolving the turbulent flux.

As discussed earlier LES 'resolves' only the large-scale fluid motions and 'models' the subgrid scale motions by filtering the Navies Stokes Equations. When unsteady RANS methods are used, it is implicitly assumed that there is a fair degree of scale separation between the large timescale of the unsteady flow features and the time scale of the genuine turbulence. However, in reality it is hard to find an evident time scale gap for many turbulent flows. Furthermore, RANS generally doesn't intend to capture most of the genuinely turbulent fluctuation information. A RANS approach thus has obvious weaknesses and poses serious uncertainties in flows for which large-scale organized features dominate, such as flows around building like obstacles. Against this background, it may be argued that the use of a sound although computationally expensive LES approach is fully justified. Although a city might not be well represented by a regular array of buildings, this is nevertheless a sound pragmatic starting point because these shapes are the basic building blocks of the city and also because there is good availability of

data for validation purposes. Thus, the study of the flow over a matrix of cubes (resembling an array of buildings) can provide some fundamental understandings of the various physical phenomena involved in the flow through an urban area. Various characteristics like vortex shedding, flow separation and velocity profiles have been experimentally investigated for such problems in the past (Meinders (1998),Meinders and Hanjalic (1999)).

In this study all the simulations have been conducted with the Smagorinsky model, because of its numerical simplicity and stability. It has also provided excellent results for the case we are interested in, when compared against the experimental data (Meinders (1998)). Since, we are interested in general behaviors rather than results for a particular point inside the domain, we present the spatially averaged profiles of the velocity, turbulent fluxes, and dispersive fluxes and explain their nature, in particular with respect to the dispersive fluxes.

4.2 Governing equations for LES

4.2.1 Transport Equations:

In LES, only the large scales are explicitly resolved by the numerical grid while the smaller ones are represented by a subgrid-scale model. The motivation for this approach is that the large-scale vortices are dominated by geometrical constraints and boundary conditions. Due to turbulent transport phenomena these vortices pass their kinetic energy on to smaller scales while the orientation of the initial vortices gets lost during this energy cascade. Therefore, the small-scale turbulence is expected to be isotropic without any preferred orientation and should consequently be much easier to model than the whole spectrum of turbulence. Starting with the governing equations for an incompressible three-dimensional (3D) unsteady flow field we apply a top-hat filter function to separate large and small-scale motion

leading to the filtered equation set

$$\frac{\partial \overline{u}_i}{\partial x_i} = 0 \tag{4.1}$$

$$\frac{\partial \overline{u}_i}{\partial t} + \frac{\partial (\overline{u_i u_j})}{\partial x_j} = \frac{-1}{\rho} \frac{\partial \overline{p}}{\partial x_i} + \frac{\partial (2 S_{ij})}{\partial x_j} \tag{4.2}$$

where $\overline{u}_i$ are the filtered velocity components, $\overline{p}$ is the filtered pressure, $S_{ij} = \frac{1}{2} \left[\nu \left(\frac{\partial \overline{u}_i}{\partial x_j} + \frac{\partial \overline{u}_j}{\partial x_i} \right) \right]$ denotes the filtered strain-rate tensor and ν the molecular viscosity. The correlation within the convective term $(\overline{u_i u_j})$ is a priori unknown and has to be modeled. The most common way is to rewrite this term into $\tau_{ij} = \overline{u_i u_j} - \overline{u}_i \overline{u}_j$ where τ_{ij} is the unresolved stress resulting from the subgrid-scale contribution and needs to be modeled by an appropriate subgrid-scale (SGS) model. The additional stresses are split into an anisotropic part $\tau_{ij}^a = \tau_{ij} - \frac{1}{3} \tau_{kk} \delta_{ij} = -2 \nu_t S_{ij}$ (where ν_t is the eddy viscosity) and an isotropic part which is added to the pressure $p^* = \overline{p} + \frac{1}{3} \tau_{kk}$, leading to the LES equation set which forms the basis of this investigation.

$$\frac{\partial \overline{u}_i}{\partial x_i} = 0 \tag{4.3}$$

$$\frac{\partial \overline{u}_i}{\partial t} + \frac{\partial (\overline{u}_i \overline{u}_j)}{\partial x_j} = \frac{-1}{\rho} \frac{\partial p^*}{\partial x_i} + \frac{\partial}{\partial x_j} \left[\nu \left(\frac{\partial \overline{u}_i}{\partial x_j} + \frac{\partial \overline{u}_j}{\partial x_i} \right) \right] - \frac{\partial \tau_{ij}^a}{\partial x_j} \tag{4.4}$$

4.2.2 Numerics

For our Large Eddy Simulations we used the Transat Code which is based on a finite volume discretization. It solves for mass, momentum and heat transport in both single and two phase flow conditions and provides the option of using Reynolds Averaged or Unsteady turbulence modeling (LES or Direct Numerical Simulation). For the present simulation we used LES because of the accuracy we needed for a better understanding of the flow. A 3rd order Runge Kutta scheme is used for time integration while the convective schemes used for density, velocity and temperature were HYBRID, CDS (Central Differencing Scheme) and HLPA (Hybrid Linear Parabolic Approximation) respectively. A preconditioned

(multigrid) GMRES (Generalized Minimal Residual Method) pressure solver is used for solving the acoustic equation. The Standard Smogorinsky Model is used to simulate the effects of the subgrid scales on the flow. Although there are more accurate models available, the established accuracy of prediction of this particular model Cheng et al. (2003) has proved to be sufficiant for our purpose.

4.2.3 Sub Grid Scale Modeling

An eddy-viscosity based model has been employed in the computations presented in this paper, where (as mentioned earlier) the anisotropic part of the SGS stress is modeled using

$$\tau_{ij} - \frac{1}{3}\delta_{ij}\tau_{kk} = -2\nu_t S_{ij} \tag{4.5}$$

The eddy viscosity ν_t is determined using Smagorinsky's expression $\nu_t = C_s \Delta^2 S$ with $|S| = (2S_{ij}S_{ij})^{1/2}$ and $\Delta = (\Delta x \Delta y \Delta z)^{1/3}$, determined using an explicit box filter of width twice the mesh size in wall-parallel planes, together with averaging in the spanwise direction and a relaxation in time with a factor of 10^{-3}. The model coefficient C_s is taken to be equal to 0.12. The dynamic Smagorinsky model (DSM) of Germano et al. (1991), with the modification of Lilly (1992), could also be applied here, but the required averaging of the model coefficient C_s (which will now depend on the resolved invariant $|S|$) is made difficult by the absence of a clear homogeneous averaging direction. The near-wall behavior of the model is such that it yields an eddy viscosity that reduces as the wall is approached, using an explicit damping following the van Driest relationship (Driest (1956)):

$$f_\mu = 1 - \exp(-y^+/26) \tag{4.6}$$

where $y^+ = y u_\tau / \nu$ is the distance from the wall in viscous wall units for which u_τ is the friction velocity.

4.3   Governing Equations for Mesoscale Model

For the mesoscale model standard Reynolds Averaged Navier Stokes Equations are used. The mass and momentum equations described in Section 3.1 can be rewritten as:

$$\frac{\partial U_i}{\partial x_i} = 0 \tag{4.7}$$

$$\frac{\partial U_i}{\partial t} + \frac{\partial (U_i U_j)}{\partial x_j} + \frac{\partial (\overline{u_i' u_j'})}{\partial x_j} = -\frac{1}{\rho}\frac{\partial P}{\partial x_i} + \nu\frac{\partial^2 U_i}{\partial x_j^2} + Q \tag{4.8}$$

where U_i is the mean part of the velocity, u_i' is the fluctuation of velocities in time, P the mean pressure, $\overline{u_i' u_j'}$ the Reynolds Stresses and Q the source term. It is quite clear that $\vec{v} = U_1\hat{i} + U_2\hat{j} + U_3\hat{k}$ and $\bar{p} = P$. The coriolis force and buyoncy forces are absorbed in the term Q. The Equation 4.8 when averaged over space takes the following form:

$$\left\langle\frac{\partial U_i}{\partial t}\right\rangle + \left\langle\frac{\partial (U_i U_j)}{\partial x_j}\right\rangle + \left\langle\frac{\partial (\overline{u_i' u_j'})}{\partial x_j}\right\rangle = -\left\langle\frac{1}{\rho}\frac{\partial P}{\partial x_i}\right\rangle + \left\langle\nu\frac{\partial^2 U_i}{\partial x_j^2}\right\rangle + \langle Q\rangle \tag{4.9}$$

where angular brackets represent the space averaging operator. Such space averaging, as we will show later in the paper, results in an additional term called the dispersive flux.
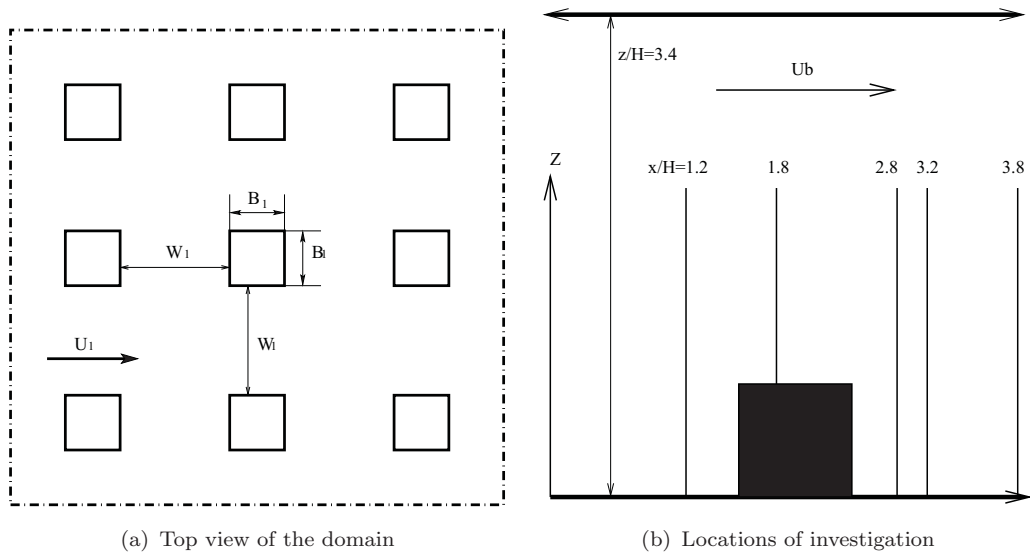

(a) Top view of the domain   (b) Locations of investigation

FIGURE 4.1: Domain and locations where comparisons have been made

4.4   Geometric Description and test cases

For the purpose of determining the validity of the LES model for our study we used the experimental results of Meinders (1998) and Meinders and Hanjalic (1999) who carried out detailed measurements of the mean flow and turbulence characteristics using Doppler anemometry throughout an array of cubes. The experimental setup consisted of 250 cubes, each of height H placed at a distance of $3H$ from their neighboring cubes in an aligned configuration (4.1(a)) consisting of 25 rows of 10 columns. The depth of the plane channel was $3.4H$. Due to the high computation cost associated with LES, our numerical simulations were based on a domain of $4H \times 4H \times 3.4H$ (*streamwise $\times$ spanwise $\times$ height*) with the cube located at the center (consistent with the experimental setup) and with periodic boundary conditions in the streamwise direction. Since a symmetric boundary condition is inappropriate for the instantaneous velocity field, a periodic boundary condition was also applied across the pair of vertical boundary planes of the flow domain in the spanwise direction. For the top and bottom walls of the channel, as well as for the surfaces of the cube, no-slip and impermeability conditions were specified (for the tangential and wall normal velocity components respectively). In accordance with the experiment, the Reynolds number for the simulation was 3800, based on the mean bulk velocity U_b and the height H of the cube. The domain was discretized into 66 nodes in each direction, with the grids being preferentially fine near the wall surfaces. Although no grid independence test was attempted it should be pointed out that the resolution we used in this simulation is finer than that used in a similar simulation reported in another study (Cheng et al. (2003)). We refer to this particular case ($4H \times 4H \times 3.4H$) which has been validated against the experimental data, as Case A. Four more simulations were conducted for domain sizes of $2H \times 2H \times 5H$, $2.5H \times 2.5H \times 5H$, $3H \times 3H \times 5H$, $4H \times 4H \times 5H$ corresponding to W_1/B_1 (W_1 is the inter-cube spacing and B_1 is the cube height) ratios of $1, 1.5, 2, 3$. These we refer to as Cases I, II, III, IV. The number of nodes used in all these cases was $66 \times 66 \times 82$ out of which $24 \times 24 \times 24$ nodes have been used to represent the cube. It should be noted that Case IV corresponds

to $W_1/B_1 = 3$, which is same as that for Case A. Indeed the only difference between these two cases is the type and placement of the upper boundary: in case IV a free slip boundary condition is applied at a height of $5H$. Although, we haven't been able to directly validate Cases I-IV because of the unavailability of experimental data, we found that the profiles of velocities and stresses inside the canopy predicted in Case IV are almost identical to those obtained in Case A, so that we may have a reasonably good degree of confidence in our own results. The volume between $3.4H$ to $5H$ in Case IV was meshed with a uniform grid of dimensions similar to those of the topmost level in the mesh of Case A. For Cases I, II and III the domain size was reduced but the same number of nodes was used, so resulting in finer resolutions in Cases I, II and III as compared to Case IV. The profiles of mean velocity and turbulence statistics were obtained using a time-averaging procedure. After carrying out the simulation for several large-eddy turnover times to ensure that the final time-averaged results were independent of the initial conditions, we averaged the instantaneous quantities over $10,000$ time steps. The corresponding averaged quantities were compared with those that were similarly obtained for $15,000$ time steps. Very little difference was observed between the two cases implying statistical convergence.

4.5 Results

4.5.1 Validation of LES model

4.5.1.1 Velocity profiles

In common with the experimental procedure of Meinders (1998), we present results on the mid-plane at different positions (x/H), Figure 4.1(b). It can be clearly seen from the velocity profiles presented in Figure 4.2 that the core flow in the region above the cube remains unidirectional and that a reverse flow is present in the spanwise oriented street canyon between two rows of cubes. The latter implies

the existence of a flow separation in the street canyon. Figure 4.3 presents the horizontal profiles of the mean streamwise velocity on the x-y plane at $z/H = 0.5$ at the same locations. The flow between cubes in the spanwise direction for $y/H > 0.5$ is unidirectional while the wake flow behind the cube is reversed for $2.5 < x/H < 3.8$. Figure 4.4 displays predictions of the horizontal profiles of the mean spanwise velocity on the $x-y$ plane at $y/H = 0.5$ at the same x/H locations. The agreement between LES results and the experimentation is generally very good. Indeed the prediction of the velocity profile (u, v, w) in general are very much acceptable.
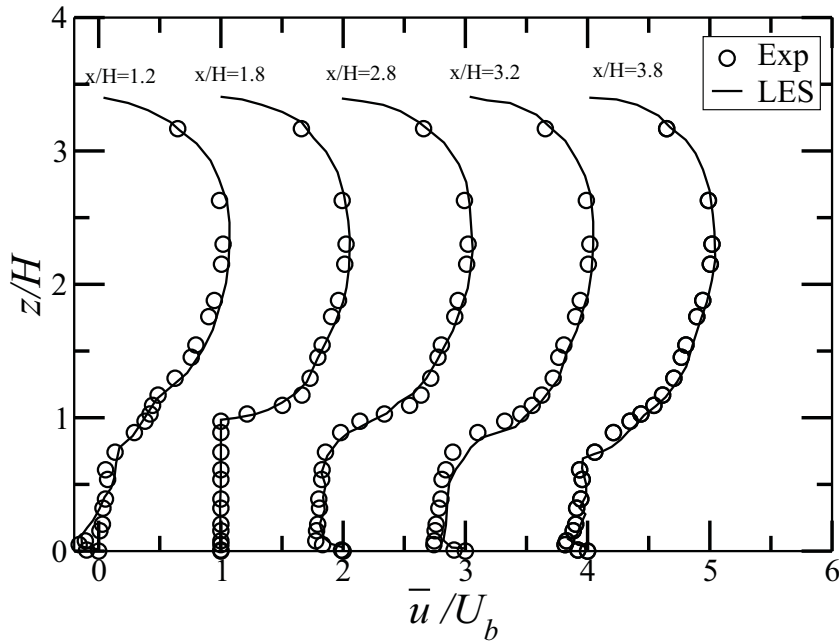
FIGURE 4.2: Vertical profiles of the time-mean streamwise velocity $\bar{u}/U_b$ on the vertical plane (x-z) through the center of the cube (ie. at $y/H = 0$). Each profile has been offset by one unit.
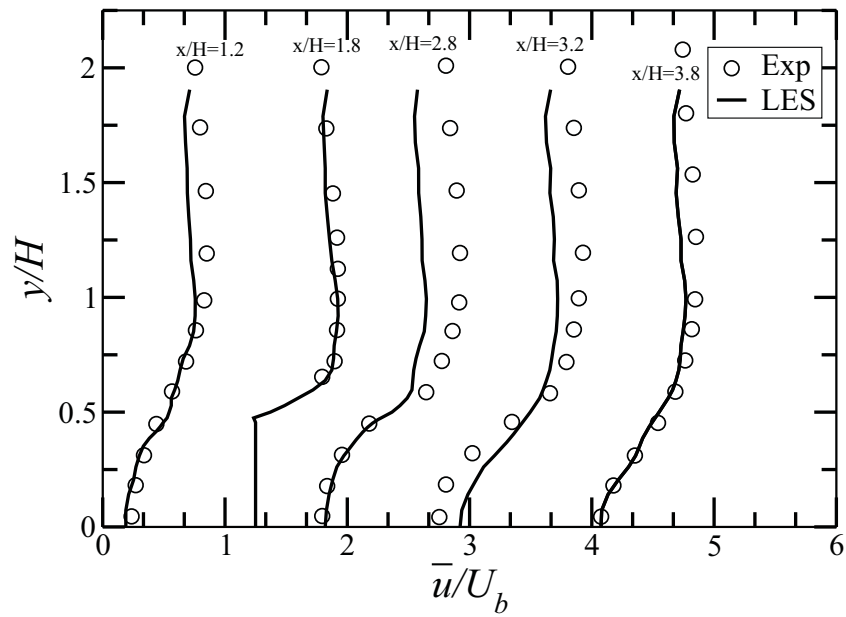
FIGURE 4.3: Horizontal profiles of the time-mean streamwise velocity $\bar{u}/U_b$ on the horizontal (x-y) plane at half cube height ($z/H = 0.5$). Each profile has been offset by one unit.
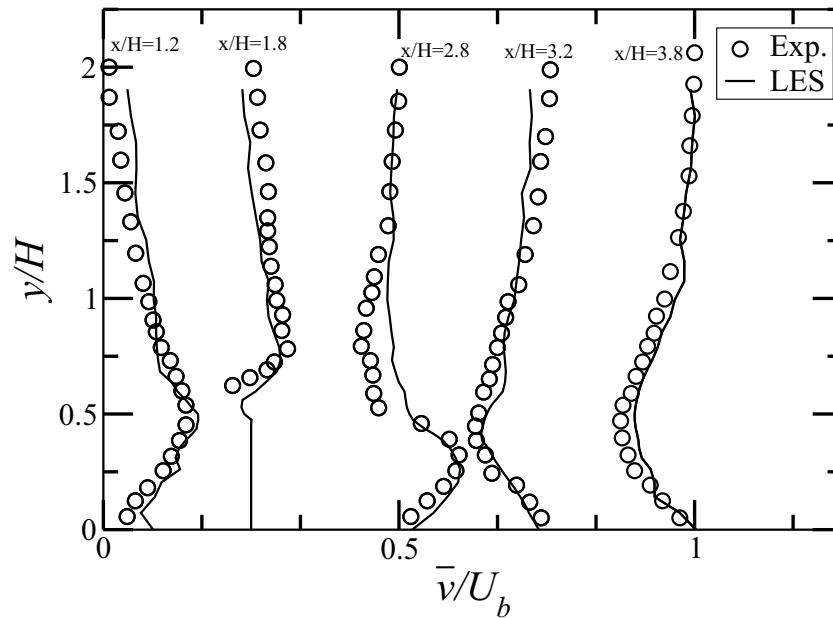
FIGURE 4.4: Horizontal profiles of the time-mean spanwise velocity $\bar{v}/U_b$ on the horizontal (x-y) plane at half cube height ($z/H = 0.5$). Each profile has been offset by 0.25 unit.

4.5.1.2 Stress Profiles

Figures 4.5(a) and 4.5(b) present the Reynolds normal stress $\overline{u'u'}$, in the x-z plane at $y/H = 0$ and on the $x - y$ plane at $z/H = 0.5$ at five selected x/H locations of 1.2, 1.8, 2.8, 3.2 and 3.8. From these results it is clear that the normal stress is always at a maximum near the walls (top or side). These peaks correspond to the generation and development of thin intense vertical and horizontal shear layers along the roof and side walls of the cube, respectively. Moving downstream of this position, the evolution of $\overline{u'u'}$ in the vertical plane along the cube centerline or in a horizontal plane at half cube height is dominated by vertical or horizontal spreading, respectively, of the vertical or horizontal shear layers generated at the rooftop and side walls of the cube. Consequently, the peak value of $\overline{u'u'}$ attenuates downstream as the streamwise normal stress is exported by outward pressure or turbulent transport from the center of the vertical or horizontal shear layers. As is very clear from Figure 4.5(a) and 4.5(b) the values of the streamwise Reynolds normal stress predicted by LES is in very good agreement with the experimental data. However, the results for the spanwise Reynolds stresses (Figure 4.6(a) and 4.6(b)) are not very encouraging. Whilst, the predicted values compares well for $z/H > 1$, inside the canopy the magnitude is underpredicted. Currently, it is an unresolved issue and is a subject of further investigation. Such mismatch was also observed in another study Cheng et al. (2003) Furthermore, profiles of Reynolds shear stress on the horizontal plane at half cube height (Figure 4.7) are in good agreement at most locations but for $x/H = 3.2, 3.8$ the agreement it is not good specially inside the canopy. Nevertheless one can say that the LES results are in good agreement with the experimental data and its use for further investigation of similar cases is reliable.
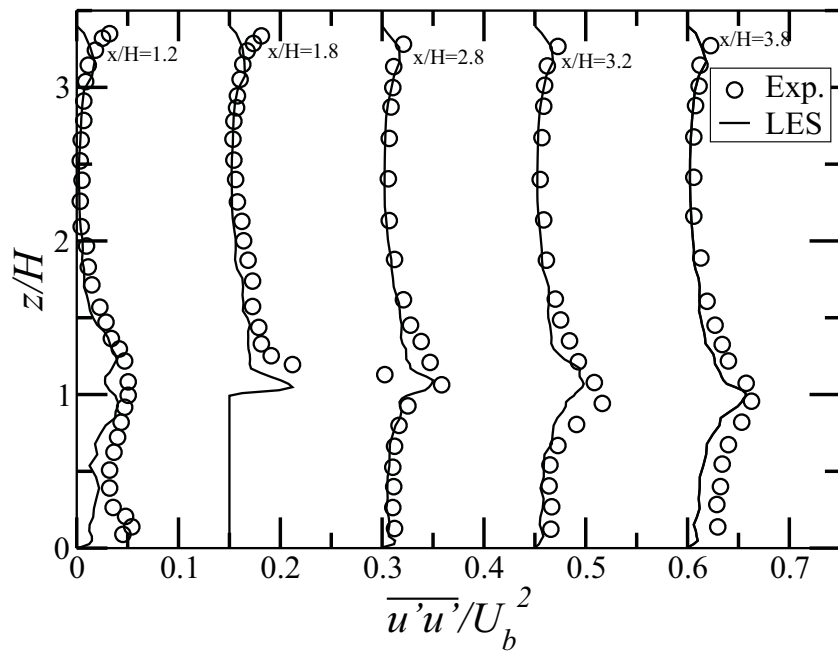
(a)
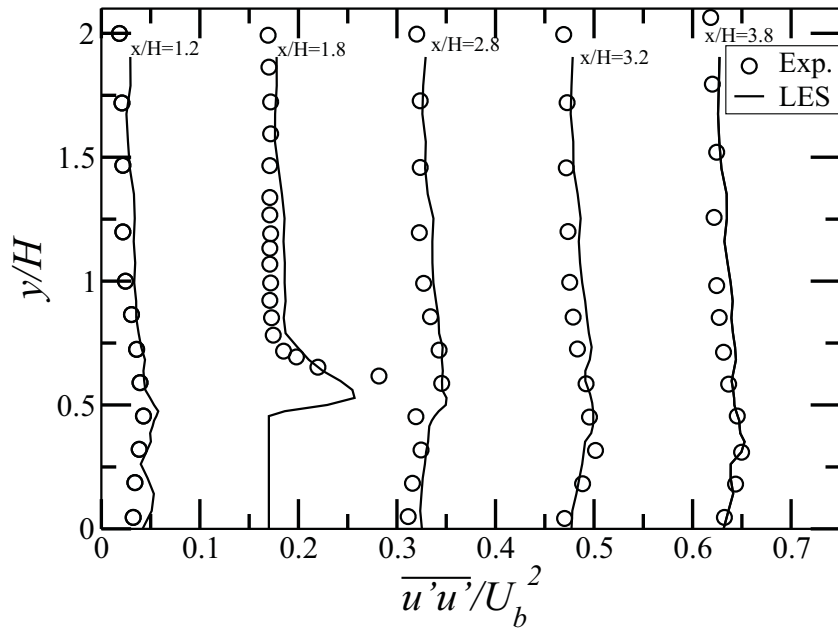
(b)

FIGURE 4.5: (a)Profiles of streamwise Reynolds normal stress on the vertical plane through the center of the cube (ie. y/H=0).Each profile has been offset from the previous one by 0.15 unit.(b)Profiles of streamwise Reynolds normal stress on the horizontal plane at half cube height (ie. z/H=0.5). Each profile has been offset from the previous one by 0.15 unit.
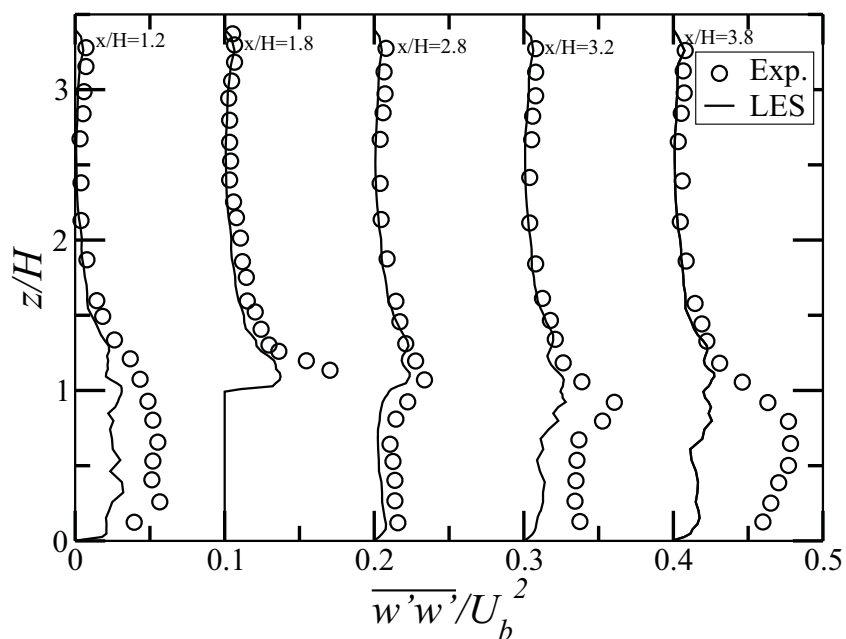
(a)
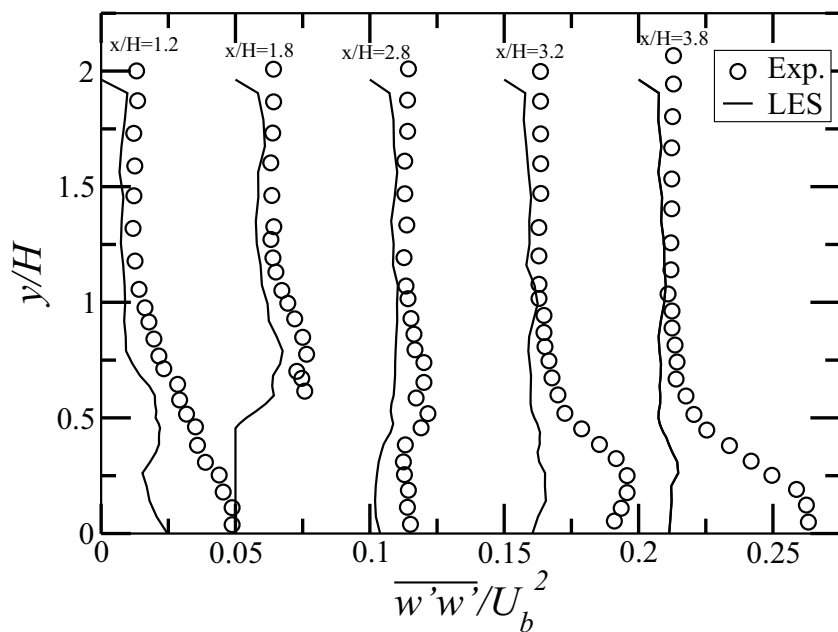
(b)

FIGURE 4.6: (a)Profile of spanwise Reynolds normal stress on the vertical (x-z) plane through the center of the cube (y/H=0).The successive profiles in the figure have been offset by 0.1 unit.(b)Profile of spanwise Reynolds normal stress on the the horizontal (x-y plane at half cube height (z/H=0.5)).The successive profiles in the figure have been offset by 0.05 unit.
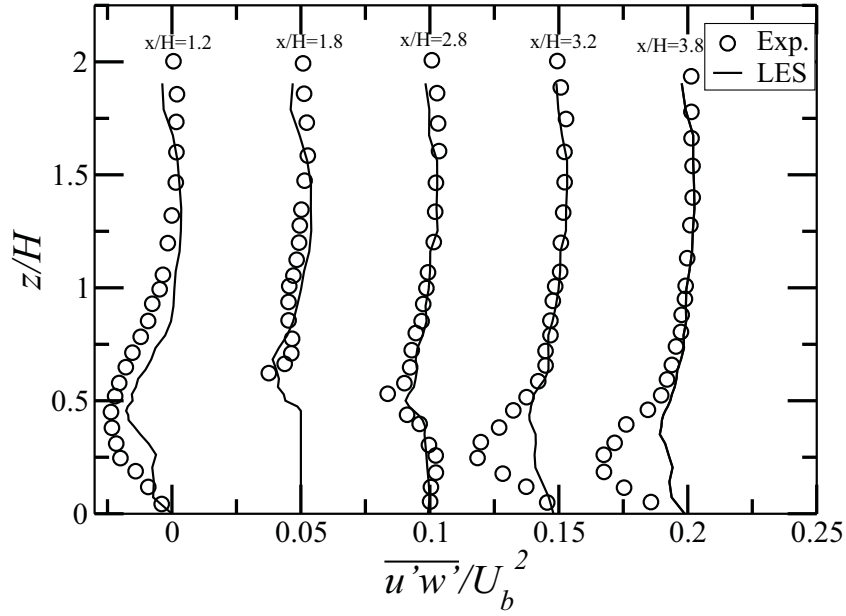
FIGURE 4.7: Horizontal profiles of Reynolds shear stress $u^{'}w^{'}/U_b^2$ on the horizontal (x-y) plane at half cube height (z/H=0.5). Each successive profiles in the figure has been offset by 0.05 unit from the previous one.

4.5.2 Effects of a change in street width to building height ratio on the spatially averaged quantities

Since our numerical simulations (LES) were conducted at a very high resolution, detailed profiles of the velocity field, pressure, stresses and turbulent kinetic energy have been obtained. However, we are interested in spatially averaged quantities that can be compared to the mesoscale grid. Assuming that the values computed by the LES at every grid point are also representative of the volume average of the corresponding grid volume, we apply Equation 4.9 to the domain on which LES was conducted. The equation for the streamwise velocity component can be

expanded to the following form

$$\frac{\partial <U>}{\partial t} + \frac{\partial <UU>}{\partial x} + \frac{\partial <UV>}{\partial y} + \frac{\partial <UW>}{\partial z} =$$
$$\frac{\partial <\overline{u'u'}>}{\partial x} + \frac{\partial <\overline{u'v'}>}{\partial y} + \frac{\partial <\overline{u'w'}>}{\partial z} - \frac{1}{\rho}\frac{\partial <P>}{\partial x} +$$
$$\nu\frac{\partial^2 <\overline{U}>}{\partial x^2} > +\nu\frac{\partial^2 <\overline{V}>}{\partial y^2} > +\nu\frac{\partial^2 <\overline{W}>}{\partial z^2} > + <Q> \qquad (4.10)$$

Since we are looking for the steady state equation we can neglect the first term on the left hand side. The second term on the LHS, using the flux divergence theorem, can be written as:

$$\left\langle \frac{\partial UU}{\partial x} \right\rangle = \frac{1}{V_{air}} \int_{V_{air}} \frac{\partial UU}{\partial x} dv = \frac{1}{V_{air}} \int_{S} UUn_x ds \qquad (4.11)$$

Here V_{air} is the volume of air over which the averaging is performed, S is the surface delimiting the volume over which the average is performed. and n_x is the x component of the normal entering the surface (x in this case because the derivative is respect to x). For horizontal surfaces, the value of n_x is zero. There are two types of vertical surfaces: those at the boundaries of the domain and those delimiting the obstacle. For the surfaces at the boundary of the domain, since we have periodic boundary conditions the contribution is zero, whilst over the surfaces of the obstacle, the velocity is zero. So, the second term on the right hand side of Equation 4.10 is zero. Similarly the third term is also zero. Furthermore, the first and second terms on the RHS can be neglected. Because the flow is turbulent, the viscous terms (fifth, sixth and seventh) can also be neglected. Thus we are left with the simplified equation:

$$\frac{\partial <\overline{u'w'}>}{\partial z} + \frac{\partial <UW>}{\partial z} + \frac{1}{\rho}\frac{\partial <P>}{\partial x} = <Q> \qquad (4.12)$$

Splitting $U = <U> +\tilde{u}$ and $W = <W> +\tilde{w}$ where $<U>$, $<W>$ are spatially averaged velocity components in the direction of flow and vertical directions and

$\tilde{u}$ and $\tilde{w}$ are fluctuation in space. Using these expressions one gets:

$$< UW >=< U >< W > + < \tilde{u}\tilde{w} > \tag{4.13}$$

Since, $< W >= 0$ Equation 4.13 reduces to $< UW >=< \tilde{u}\tilde{w} >$. Introducing this into Equation 4.12 we have the following equation:

$$\frac{\partial < \overline{u'w'} >}{\partial z} + \frac{\partial < \tilde{u}\tilde{w} >}{\partial z} + \frac{1}{\rho}\frac{\partial < P >}{\partial x} =< Q > \tag{4.14}$$

where the first and second LHS terms are the gradient of turbulent and dispersive fluxes respectively in the vertical direction and the third term is the gradient of pressure in the flow direction. To study the vertical profiles of the streamwise velocity, Reynolds shear stress, and dispersive stress we evaluate these quantities from the result obtained from the simulation using equations 4.15 through to 4.18.

$$< U >_k= \frac{\sum_i \sum_j (U)_{i,j} V_{i,j}}{\sum_i \sum_j V_{i,j}} \tag{4.15}$$

$$< \tilde{u}\tilde{w} >_k= \frac{\sum_i \sum_j (\tilde{u}\tilde{w})_{i,j} V_{i,j}}{\sum_i \sum_j V_{i,j}} \tag{4.16}$$

$$< \overline{u'w'} >_k= \frac{\sum_i \sum_j (\overline{u'w'})_{i,j} V_{i,j}}{\sum_i \sum_j V_{i,j}} \tag{4.17}$$

$$< TKE >_k= \frac{\sum_i \sum_j (TKE)_{i,j} V_{i,j}}{\sum_i \sum_j V_{i,j}} \tag{4.18}$$

where $V_{i,j,k} = 0$ for the blocked regions and i,j,k are the indexes in the streamwise, spanwise and vertical directions. As is clear from equations 4.15 to 4.18 the averaging is performed over horizontal planes at different heights.
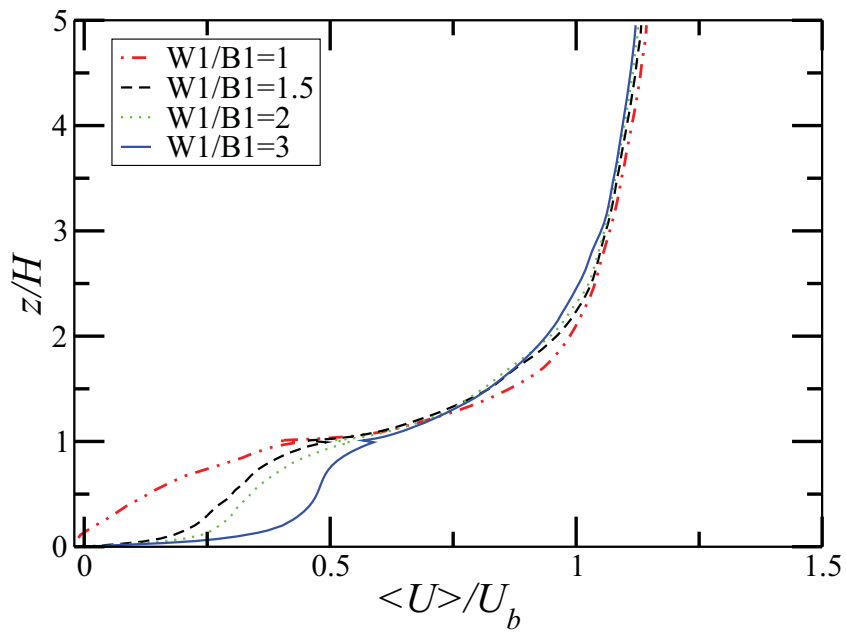
FIGURE 4.8: Space averaged velocity
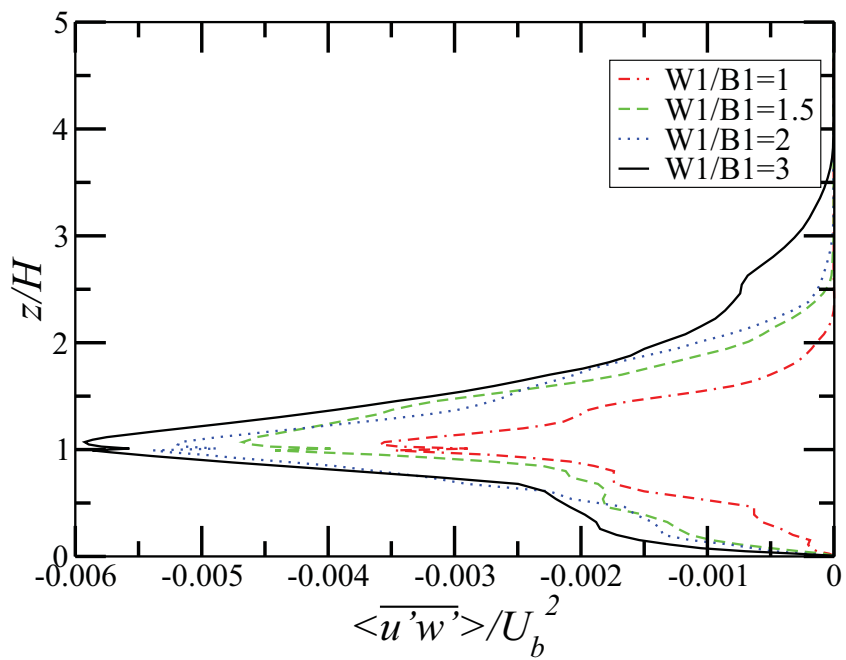
FIGURE 4.9: Space averaged turbulent Flux
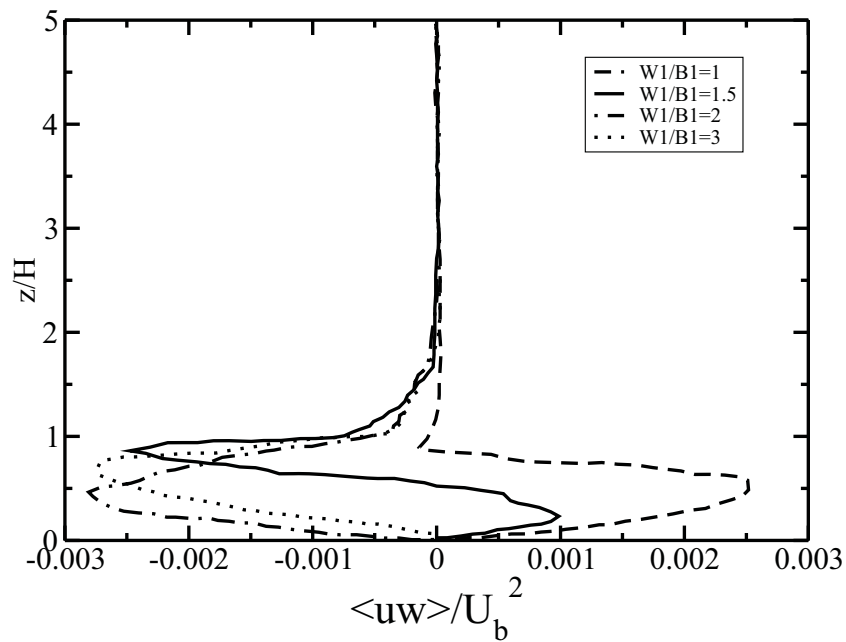
FIGURE 4.10: Space averaged dispersive flux

4.5.2.1 Mean Velocity

Figure 4.8 gives the spatially averaged streamwise velocity profiles. These appear to be logarithmic above the canopy but inside the canopy they can be strongly affected by adjacent buildings, as can be seen comparing the cases corresponding to different W_1/B_1 ratios. In the case of $W_1/B_1 = 3$, the profile inside the canopy also takes a logarithmic profile because the flow has sufficient time and space to redevelop within the wide canopy. However, as W_1/B_1 ratio decreases the profile starts to deviate from the normal logarithmic profile, becoming linear for $W_1/B_1 = 1$.

4.5.2.2 Turbulent Stresses

The mesoscale unresolved fluxes can be split into two components: the turbulent part and the dispersive part. As shown in Figure 4.9 the vertical profile of the turbulent stresses is negative throughout the profile (there is a downward transfer

of momentum) implying that the flux is a downgradient. Within the canopy, the turbulent fluxes decrease with height until the top of the cube where a minima is reached. Above the canopy the magnitude increases with height, to a height of $3.5H$. These fluxes are then absent above this height, so that there is very little sign of turbulence within this region. Also noteworthy are the linear profiles of the turbulent stress both inside and above the canopy with a negative and positive slope respectively. These turbulent stresses, which are actually an indication of the transport property of turbulence, decrease with W_1/B_1 ratio; indicating that an area of widely spaced buildings can experience more turbulence because of greater penetration of eddies within these streets. Conversely, very narrow streets will experience little turbulence because of low eddy penetration. However, there is a need for more exhaustive data analysis to support such a generalization.

(a) $W_1/B_1 = 1$

(b) $W_1/B_1 = 1.5$

(c) $W_1/B_1 = 2$

(d) $W_1/B_1 = 3$

VM: -0.1   0   0.26   UM: -0.14   0   0.108   0.356   0.604   0.852   1.1
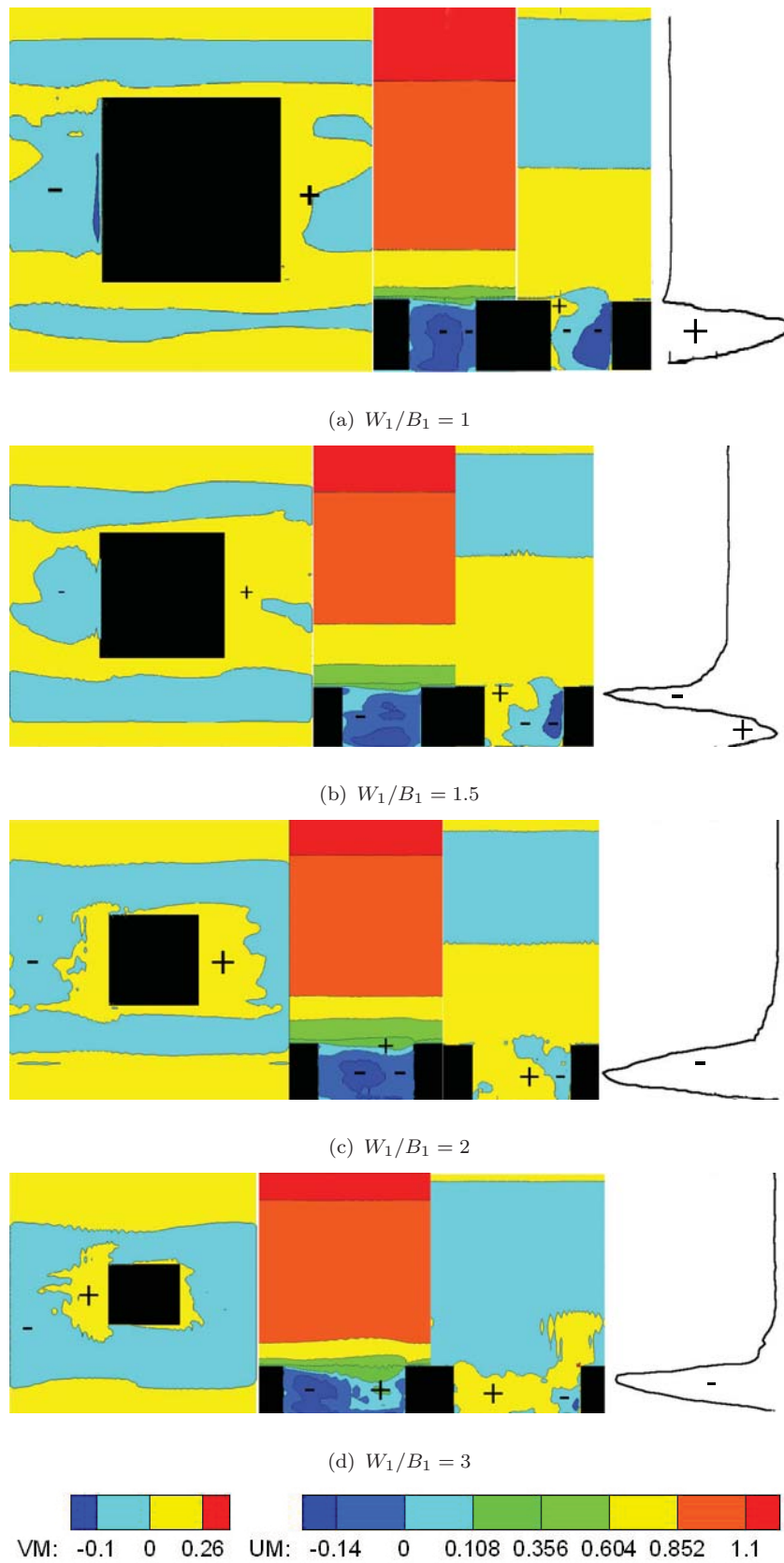
FIGURE 4.11: From extreme left to extreme right. Contours of the vertical velocity at the top of the canopy, streamwise velocity at the mid plane, vertical velocity at the mid plane, profile of space averaged dispersive flux (extreme right)
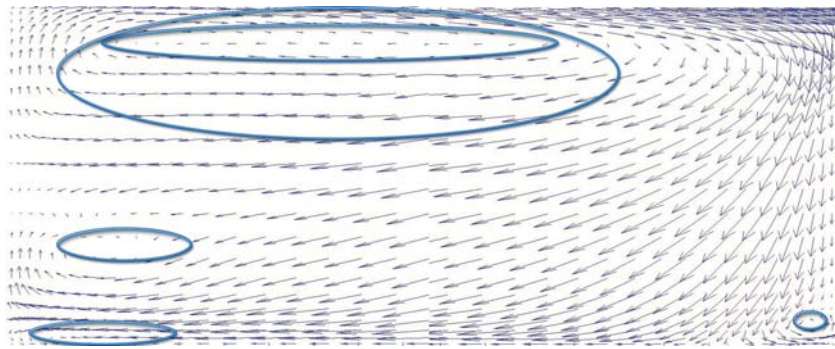
(a) $W_1/B_1 = 1$
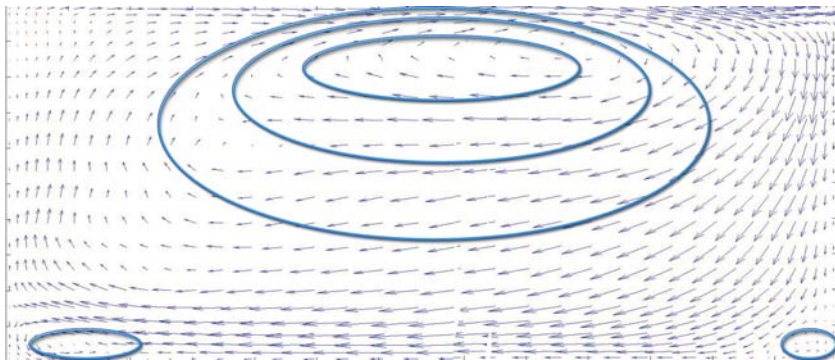
(b) $W_1/B_1 = 1.5$
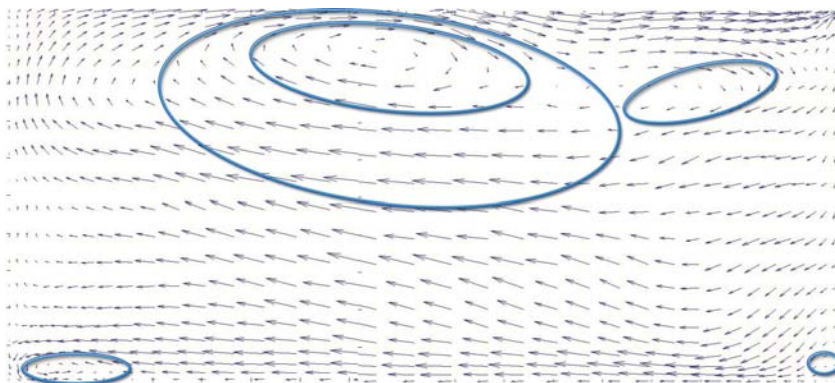
(c) $W_1/B_1 = 2$
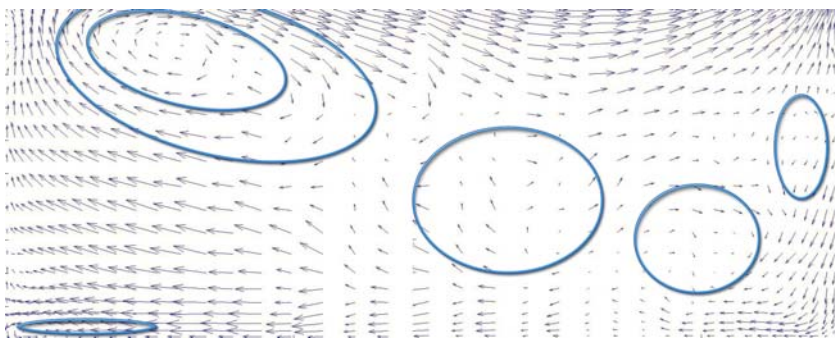
(d) $W_1/B_1 = 3$

FIGURE 4.12: Time averaged Velocity field and vortices inside the canopy

4.5.2.3 Dispersive Stresses

In most mesoscale models the dispersive stresses mentioned earlier are neglected. In order to study and understand their behavior, these stresses were plotted in Figure 4.10. From this it is clear that these stresses can be significant and in some cases comparable to turbulent stresses (Figure 4.9). These dispersive stresses are absent at the bottom wall but increase or decrease (depending upon W_1/B_1) to attain a maxima or minima at half the cube height. Above the canopy their magnitude is always negative with one minima. As with turbulent stresses they reduce to zero above $3H$. Of particular interest is that these dispersive stresses don't exhibit a regular trend when expressed as a function of W_1/B_1. When the cubes are wide apart ($W_1/B_1 = 2, 3$) the dispersive fluxes inside the canopy are negative but upon decreasing the inter-cube spacing beyond a certain point a switch to a positive flux is experienced. The physical explanation of the dispersive stresses lies in the coherent vortex formed in the canyon.

In order to better understand the behavior of these dispersive fluxes contours of vertical velocity (at the top of the canopy), horizontal velocity and spatially averaged dispersive flux for different W_1/B_1 are plotted side by side, as shown in Figure 4.11. Since dispersive flux is defined as $\tilde{u}\tilde{w} = (<U> - U)(<W> - W)$, its sign will also depend on $\tilde{u}$ and $\tilde{w}$. Here $<U>$ is always positive (Figure 4.8) and inside the canopies U is mostly negative implying that $\tilde{u}$ will mostly be positive. Thus, the sign of the dispersive flux will depend on the sign of $\tilde{w}$. Also since, $<W>$ is negligible one can conclude that the sign of $\tilde{w}$ will be opposite to that of W. Now let us consider each of our cases in turn.

Case 1 ($W_1/B_1 = 1$): In Figure 4.12(a) one can see that a jet of fluid impinges the top of the windward side of the cube and is deflected downward, resulting in two clockwise rotating vortices one above the other, with the stronger one at the top. These vortices are eccentric with their "eyes" shifted toward the leeward side of the cube. The formation of such eccentric vortices results in negative U and W in most of the regions inside the canopy (Figure 4.11(a)). However, there are regions

near the bottom and top of the leeward side of the cube where there is a positive vertical velocity. At the same time there are regions near the mid plane inside the canopy where the vertical velocity is mostly negative. The existence of a mixture of regions of positive and negative vertical velocity field results in the cancellation of the dispersive fluxes during the averaging over horizontal planes near the top and bottom planes. Near the mid-plane there is no such canceling and hence a maxima of dispersive flux is obtained.

Case 2 ($W_1/B_1 = 1.5$): An increase of the W_1/B_1 ratio from 1 to 1.5 results in the shift of the eye of the primary vortex towards the windward side of the cube. The primary vortex in this case is concentric (Figure 4.12(b)). The formation of such a nearly concentric vortex results in positive vertical velocities near the leeward side of the cube and negative velocities near the windward side as show in Figure 4.11(b) . On any horizontal plane below $0.5H$ there is greater flux injection (negative vertical velocity) and less ejection (positive vertical velocity). However, above $0.5H$ the situation is exactly the opposite. At the mid-plane itself both the ejection and injection balance each other resulting in a cancellation of dispersive fluxes. As explained earlier the profile of the dispersive flux depends on the sign of the vertical velocity, so that in this particular case the dispersive fluxes are positive below $0.5H$ and negative above $0.5H$.

Case 3 and 4 ($W_1/B_1 = 2, 3$): For both $W_1/B_1 = 1$ and 1.5 there is a clear demarcation between the zones of positive and negative vertical velocities. Injection from the top takes place near the windward side and ejection near the leeward side of the cube. This is the result of a strong large vortex formed inside the canopy as a consequence of the strong shear forces at the top. However, this behavior changes significantly when W_1/B_1 is increased to 2 and 3. Contrary to the observations in cases 1 and 2, in these cases the injection occurs in the middle of the top plane just above the canopy (Figure 4.12(c) and 4.12(d)) and the jet impinges not on the top of the cube but on the lower half of the cube. This situation leads to the formation of several tilted vortices resulting in strong ejection at both the leeward and the windward side of the cube. Also the tilt in the vortices, which is a result

of the injection in the middle, results in positive vertical velocities in most regions and hence negative dispersive fluxes (Figures 4.11(c) and 4.11(d)).

In all cases (I-IV) the vertical velocity above the cube and the canopy is positive and hence it always resulted in a negative dispersive flux. Another thing to be observed in the Figures 4.8, 4.9 and 4.10 is that the effect of the cube can be felt upto a height of $3H$ to $4H$ which is consistent with observations from field experiments (Rotach (1993)).

4.6   Conclusion

LES with a standard Smogarinsky model was used to compute a fully developed turbulent flow over a matrix of cubes. Detailed comparisons between the numerical predictions obtained with the LES and the corresponding experimental data of Meinders (1998) were conducted. The numerical data generated was used to study the spatially averaged profiles of the velocity, turbulent flux, turbulent kinetic energy and dispersive flux. The results of this investigation allow the following conclusions to be drawn:

- Validation of the numerical results: Qualitatively, the profiles of mean velocities and Reynolds stresses, the latter including $\overline{u'^2}, \overline{w'^2}$ and $\overline{u'w'}$ are generally well represented by the LES model. The greatest discrepancy between the predictions and observations was for $\overline{w'^2}$ within the street canyon of the obstacle array. The underestimation of $\overline{w'^2}$ will lead to an underestimation of the turbulent kinetic energy and hence must be kept in mind. Overall the numerical predictions were very good for the this particular problem.

- Spatially Averaged Quantities: We then carried out tests for an array of cubes with different inter-cube spacings. The results that were obtained from LES were spatially averaged to derive information useful for urban mesoscale simulations. It was evident that the profiles of turbulent flux and

dispersive flux, which we have found to be similar in magnitude, go to zero at nearly three times the cube height, a fact which has been observed in various field experiments Rotach (1993). Of particular significance has been the use of the results to explain the behavior of dispersive fluxes. It was observed that for widely spaced array of cubes these fluxes were negative (same sign as the turbulent fluxes). This implies that these fluxes can be modeled in the same way as the turbulent fluxes. However, for high packing density these profiles started assuming a negative profile which may result in the canceling of other sources in the equation and therefore needs to be modeled differently.

However, it must be stressed here that the conclusions drawn from this study are only valid for a regular array of cubes in a neutral atmosphere. In order to generalize such conclusion, more numerical and wind tunnel experiments are required. Nevertheless these results may be used to inform the development of a new Urban Canopy Model (subject to above constraints) as described in the next chapter.

On a related note this work leads us to pose some interesting scientific questions, such as: How much complexity must be added to produce a configuration that gives spatially-averaged values similar to those of a real city? Or in other words, which is the simplest configuration that represents a real city? Which combination of parameters (building heights, building shapes, building width, street widths etc) is sufficient to characterize city morphology.

Chapter 5

Development of an Urban Canopy Model

In the last chapter we investigated in detail the flow over an array of cubes. Here we use those observations to develop a new urban canopy model for estimating the momentum and energy exchanges between the built surfaces and the air surrounding them.

5.1   Introduction

In order to more accurately model the physics of the urban canopy, new concepts in surface modeling have been developed. These models aim to solve the Surface Energy Balance for a realistic 3D urban canopy. They share in common the following characteristics in their construction:

- Buildings have a 3D shape.

- The schemes possess separate energy budgets for roof, streets and walls.

- Radiative interactions between streets and wall(s) are explicitly treated.

These models are based on a geometry which, even though simple, is reasonably close to the reality that they aim to represent. Since they are composed of both horizontal and vertical surfaces, they are able to capture the special energetic behaviours of the urban canopy. The use of distinct surface types gives the advantage that their properties (e.g. wall heat capacity, wall temperature) are more easily interpreted than the corresponding averaged quantities found in modified vegetation schemes (e.g. the heat capacity or surface temperature of the whole system). These new models use a relatively simple and robust methodology to compute the complex radiative exchanges in the manner of Noihan (1981), based on view factors between the different surfaces or facets comprising the surface. Solar reflections and shadows are also explicitly resolved. Storage of energy in the materials is easily modeled, either by the force-restore method or the more accurate heat conduction equation. The latter allows simulation of different layers in roads, roofs or walls, including insulation layers. These models can be separated into two main categories: those where the canopy air is parameterized, as in TEB (Masson (2000)), and those using a drag approach, as for forests, but here with buildings (as in Martilli and Rotach (2002)). Here the first ones are referred to as single-layer models, because there is direct interaction with only one atmospheric layer, above the uppermost roof level. The second category are called multilayer models, because several air layers are explicitly influenced by the buildings (down to the road surface, because the air layers extend down into the canopy).

5.1.1   Single-layer models

In these schemes, the exchanges between the surface and the atmosphere occur only at the top of the canyons and roofs. This means that, when coupled with an atmospheric model, the base of the atmospheric model is located at roof level. This has the advantage of simplicity and transferability, but means that the characteristics of the air in the canyon space must be specified. In general, the logarithmic law for wind is assumed to apply down to just under the top of the canyon, and an exponential law is used below. Air temperature and humidity are assumed to

be uniform in the canyon. The simplest of these models is the Town Energy Balance (TEB) scheme of Masson (2000). Its simplicity derives from the use of only one roof, one generic wall and one generic road. This does not mean that road orientations are not considered, because averaging is performed over all directions in order to keep only these generic surfaces. The advantage to the generic facet scheme is that relatively few individual Surface Energy Balance (SEB) Equations need to be resolved, radiation interactions are simplified, and therefore computation time is kept low, despite the (simplified) 3D geometry. Interception of water and snow, and the associated latent heat fluxes, are also included. Despite the simplification hypotheses, TEB has been shown to reasonably reproduce the SEB, canyon air temperature and surface temperatures observed in dense urban areas (Masson and Oke (2002); Lemonsu (2004)). The two other such schemes retain a higher level of detail, because the differently orientated roads (and hence their walls) are simulated separately. Mills (1997) chose a geometry kernel based on building blocks, with roads at right angles. The model by Kusaka et al. (2001)) is very similar too. Inspite of many arguments in favor of Single-layer model, the basic underlying assumption that the temperature, humidity and wind velocity can be represented by a single value inside the canopy seems unreasonable (as will be shown in later chapters).

5.1.2 Multi-layer models

When the drag approach is applied, exchanges with the atmosphere occur at ground level and at several atmospheric levels in contact with the buildings. The SEB is still computed for each surface or part of the surface, but atmospheric properties such as the wind and temperature are not assumed, they depend more closely on the interaction between the canopy and the air. In particular, such models are able to represent profiles of the turbulent statistics of the canyon air and in the roughness sub-layer. However, such a refinement is made at the cost of direct interaction with the atmospheric model because their equations are modified. Among these models, that of Martilli and Rotach (2002) models in a high

degree of detail the SEB, since any number of road (and wall) orientations are available, different building heights can be present together, and at each level of the wall intersecting an air level, there is a separate energy budget. This feature means that this model is able to represent the differential heating of the wall due to the shading effects of local obstructions. This model has been tested against wind turbulence data from Rotach (2001) and Roth (2000). Two other models of this type have been developed, one by Vu et al. (1999) the other by Kondo and Liu (1998). They are based on similar principles to that of Martilli, except that only one SEB per wall is possible (there is no vertical resolution). However, in Vu et al. (1999), the volume occupied by the buildings is more accurately taken into account. In Martilli's model, additional terms influence the air at each level, but the volume of air remains the same as when there are no buildings. In the Vu et al. (1999) model the volume of the buildings is removed from the volume of air, however, this requires strong modification to the atmospheric model equations. Most of the models have been compared with field experiments, but these have considerable uncertainties associated with them. In this study we have tried to understand the spatially averaged profiles of velocities, turbulent kinetic energy and dispersive fluxes and have come up with a simple column model to predict the velocity and tke profile inside the canopy, taking into account geometrical parameters like the building height, width and the probability of having buildings of a particular height in a region as well as the street width. Results from the model have also been validated against the results from the LES of flow over an array of cubes as described in the last chapter.

5.2 Numerical Experiments

As noted earlier Large Eddy Simulations were conducted over an array of cubes for the arrangements shown in Figure 5.1. Four scenarios were investigated relating to four different B/W ratios: 1,1.5,2,3. Results from these simulations gave a good insight into the fluid flow behavior around bluff bodies (an array of cubes in this
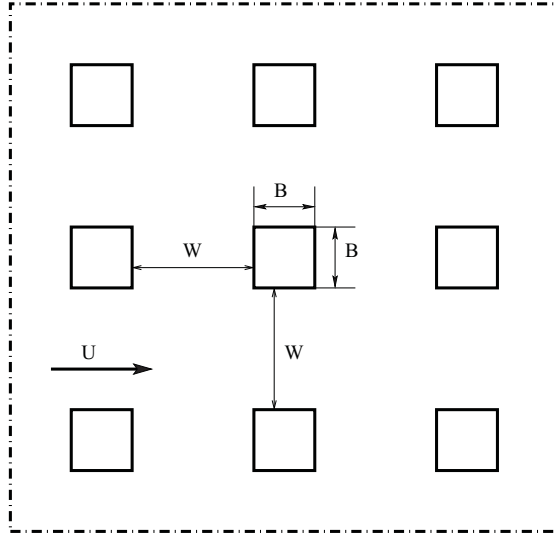
FIGURE 5.1: Regular array of cubes in an aligned configuration

case). The details of those simulations have already been explained in the previous chapter. Here we use the spatially averaged quantities from the simulations to develop and validate our new urban canopy model.

5.3 Space-averaged equations

The mesoscale equations following the averaging procedure described in section 4.5.2 take the following form

$$\frac{\partial <U>}{\partial t} + \frac{\partial <\overline{u'w'}>}{\partial z} + \frac{\partial <\tilde{u}\tilde{w}>}{\partial z} = -\frac{1}{\rho}\frac{\partial <P>}{\partial x} + <Q_u> \qquad (5.1)$$

$$\frac{\partial <V>}{\partial t} + \frac{\partial <\overline{v'w'}>}{\partial z} + \frac{\partial <\tilde{v}\tilde{w}>}{\partial z} = -\frac{1}{\rho}\frac{\partial <P>}{\partial y} + <Q_v> \qquad (5.2)$$

The unsteady term has been retained in the above equations for the purpose of generality. This also implies that with low horizontal resolution (here 1.5km) compared to high vertical resolution (a few meters) in a mesoscale model, vertical fluxes dominate the horizontal fluxes and represent the main source term in the energy budget equation. Therefore, the horizontal fluxes can be neglected, as
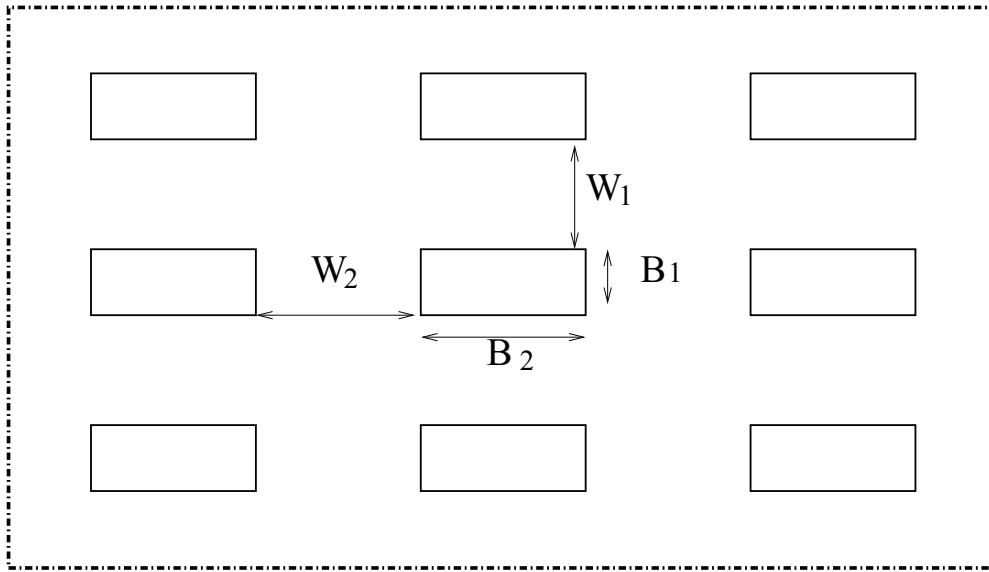
FIGURE 5.2: Regular array of cubes in an aligned configuration

shown by Masson and Oke (2002) with measurements. The vertical turbulent exchanges balance the fluxes coming from the buildings and ground, thus the equation for sensible heat for each layer in the canopy is parametrized as follows:

$$\frac{\partial < \theta >}{\partial t} + \frac{\partial < \overline{\theta' w'} >}{\partial z} + \frac{\partial < \tilde{\theta} \tilde{w} >}{\partial z} = < Q_\theta > \qquad (5.3)$$

Anthropogenic heat sources or sinks can be directly added to the term $< Q_\theta >$. It is expected at this point of time that the solution of these equations will result in the vertical profiles of U,V and θ and the corresponding source terms.

5.4   Canopy Model

The space averaged equations, after slight modifications suggested by Kondo et al. (2005), takes the following form and constitute our 1-D model for predicting the velocities, temperature and TKE inside the canopies. The drag forces offered by the cubes have been taken to be proportional to the square of the local velocity field and the turbulent and dispersive fluxes have been combined (because they are similar in nature for $W_1/B_1 > 1$).

$$\frac{\partial <U_c>}{\partial t} = \frac{1}{\Lambda}\frac{\partial}{\partial z}\left(K_{zu}\Lambda\frac{\partial <u>}{\partial z}\right) - a_1 C_d <U_c> \sqrt{<U_c>^2 + <V_c>^2} \quad (5.4)$$

$$\frac{\partial <V_c>}{\partial t} = \frac{1}{\Lambda}\frac{\partial}{\partial z}\left(K_{zu}\Lambda\frac{\partial <v>}{\partial z}\right) - a_2 C_d <V_c> \sqrt{<U_c>^2 + <V_c>^2} \quad (5.5)$$

$$\frac{\partial <\theta_c>}{\partial t} = \frac{1}{\Lambda}\frac{\partial}{\partial z}\left(K_{z\theta}\Lambda\frac{\partial <\theta>}{\partial z}\right) + <Q_\theta> \quad (5.6)$$

$$\frac{\partial <E_c>}{\partial t} = \frac{1}{\Lambda}\frac{\partial}{\partial z}\left(K_{ze}\Lambda\frac{\partial <E_c>}{\partial z}\right) + \rho K_{ze}\left(\frac{\partial <U_c>}{\partial z}\right)^2 + \rho K_{ze}\left(\frac{\partial <V_c>}{\partial z}\right)^2 - \frac{\rho C_e <E>^{3/2}}{l_e}$$
$$(5.7)$$

Here $<U_c>$ and $<V_c>$ are the wind velocity components in the streamwise and spanwise directions inside the canopies. θ_c is the space averaged potential temperature. The subscript c is added to stress the fact that these quantities are computed on the one dimensional urban canopy grid. Λ can be defined as a volume porosity. The heights of buildings may be non-uniform and can be described using a variable $Pb(z)$ such that $0 \leq Pb(z) \leq 1$. $Pb(z) = 1$ means that the entire building area at z is actually occupied by buildings.

$$a_1 = \frac{B_1 P_b(z)}{(B_1 + W_1)(B_2 + W_2) - B_1 B_2 P_b(z)} \quad (5.8)$$

$$a_2 = \frac{B_2 P_b(z)}{(B_1 + W_1)(B_2 + W_2) - B_1 B_2 P_b(z)} \quad (5.9)$$

It should be noted, that in the expression of a_1 and a_2, any plane area can be approximated to an area with infinitely wide streets. In such a situation the variables a_1 and a_2 become zero leading to a no drag situation, as one would expect. Similarly if the variable $P_b(z)$ takes on a value of zero for all z we also

have a plane. Λ, also defined as a volume porosity, is defined as follows:

$$\Lambda = 1 - \left(\frac{B_1 B_2}{(B_1 + W_1)(B_2 + W_2)} \right) P_b(z) \tag{5.10}$$

For our one dimensional case, this is also the surface permeability. Also, in the atmosphere (except for the surface layer), turbulent diffusion coefficients are used. Gambo (1978) formula is used for $R_f \leq R_{fc}$, where R_f is the flux Richardson number and $R_{fc} = 0.29$ is the critical Richardson number, so that

$$K_{zu} = L^2 \left| \sqrt{\left(\frac{\partial U_c}{\partial z} \right)^2 + \left(\frac{\partial V_c}{\partial z} \right)^2} \right| \frac{S_m^{3/2}}{\sqrt{C}} (1 - R_f)^{1/2} \tag{5.11}$$

A complete derivation of the expression of K_{zu} can be found in Gambo (1978).

The length scale L is given by Watanabe and Kondo (1990) and was derived from consideration of forest canopy.

$$L(z) = \frac{2k^3}{ca} (1 - exp(-\eta)) \tag{5.12}$$

where η is

$$\eta = \frac{caz}{2k^2} \tag{5.13}$$

and above the canopy we use the interpolation formula of Blackadar (1968)

$$L(z) \leq \frac{kz}{1 + \frac{kz}{L_o}} \tag{5.14}$$

which interpolates between two limits $L \sim kz$ as $z \to 0$ and $L \sim L_0$ as $z \to \infty$. In this study we have used a value of $L_o = 70m$. When $R_f > R_{fc}$,

$$k_{zu} = L^2 \left| \sqrt{\left(\frac{\partial U_c}{\partial z} \right)^2 + \left(\frac{\partial V_c}{\partial z} \right)^2} \right| \tag{5.15}$$

Computation of the source of energy equation is described in the following sections.

5.4.1 Surface Fluxes
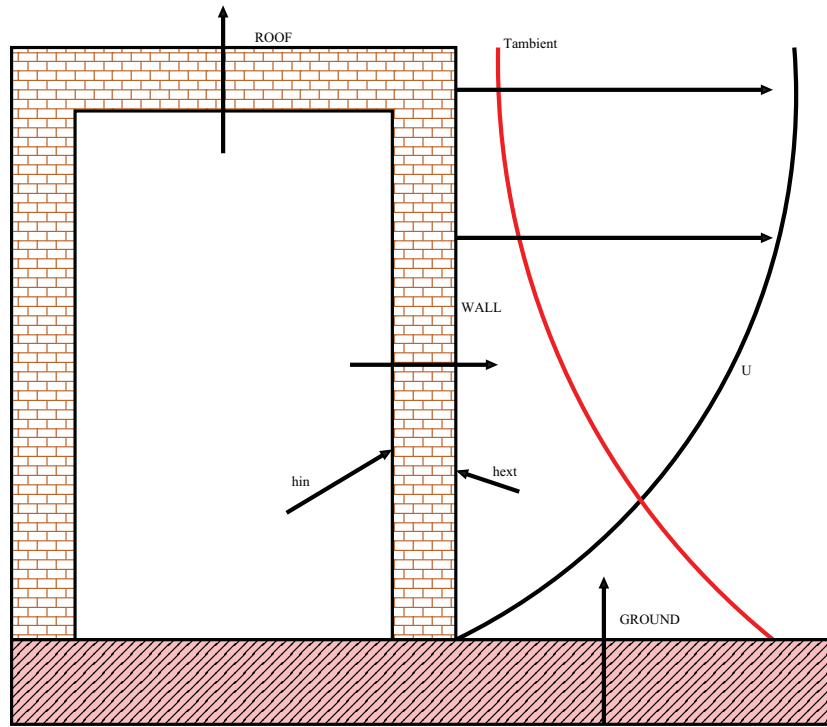
FIGURE 5.3: Building energy model

In order to compute our surface temperatures the following heat diffusion equation is solved for walls, roofs and ground surfaces (Figure 5.4.1).

$$\frac{\partial \rho_{mat} C_{pmat} T_{mat}}{\partial t} = \frac{\partial}{\partial x}\left[K_{mat}\frac{\partial T_{mat}}{\partial x}\right] \tag{5.16}$$

where T_{mat} is the temperature at the different layers inside the material, ρ_{mat} is the density, C_{pmat} is the specific heat capacity and K_{mat} is the thermal conductivity of the built material. To solve the problem following boundary conditions are applied at the interior and exterior surfaces of the buildings.

External boundary condition: A time varying heat flux boundary condition is applied:

$$q_{ext} = (1 - \alpha_{ext})Rs_{ext} + \epsilon_{ext}Rl_{ext} - \epsilon_{ext}\sigma T_n^4 - h_{ext}(T_n - T_{amb}) \tag{5.17}$$

where α_{ext} and ϵ_{ext} are respectively the albedo and emmisivity of the external layer, σ the Boltzmann constant, Rs_{ext} the incoming external shortwave radiation, Rl_{ext} the longwave radiation received by the external surface and h_{ext} is the external heat transfer coefficient. In particular following the work of Clarke (2001), this value is determined by the following expression:

$$h_{ext} = c_c \left[a_c + b_c \left(\frac{U^{hor}}{d_c} \right) \right] \tag{5.18}$$

where a_c, b_c, n_c, d_c are constants deduced from laboratory studies, respectively equal to 1.09, 0.23, 5.678 and 0.3048. The term U^{hor} corresponds to the horizontal wind component.

When $T_n < T_{amb}$, the usual Monin Obukov theory is used for both horizontal and vertical surfaces. The MO theory is also used to calculate the momentum flux with roughness lengths of $0.1m$ and $0.0041m$ specified for the momentum in all conditions and potential temperature for $T_n < T_{amb}$ respectively on each surface. The treatment of the internal boundary condition is similar to that of the external albeit with a differnt correlation of heat transfer coefficient and a set internal temperature.

5.5 Results

5.5.1 Comparison between the Column Model and LES results

The new model was run for the steady state isothermal case to obtain the streamwise velocity and turbulent kinetic energy profiles. A comparison between the results from the new model and LES is shown in Figures 5.4 and 5.5 for the velocity and turbulent kinetic energy respectively.

(a) $W_1/B_1 = 1$

(b) $W_1/B_1 = 1.5$

(c) $W_1/B_1 = 2$

(d) $W_1/B_1 = 3$
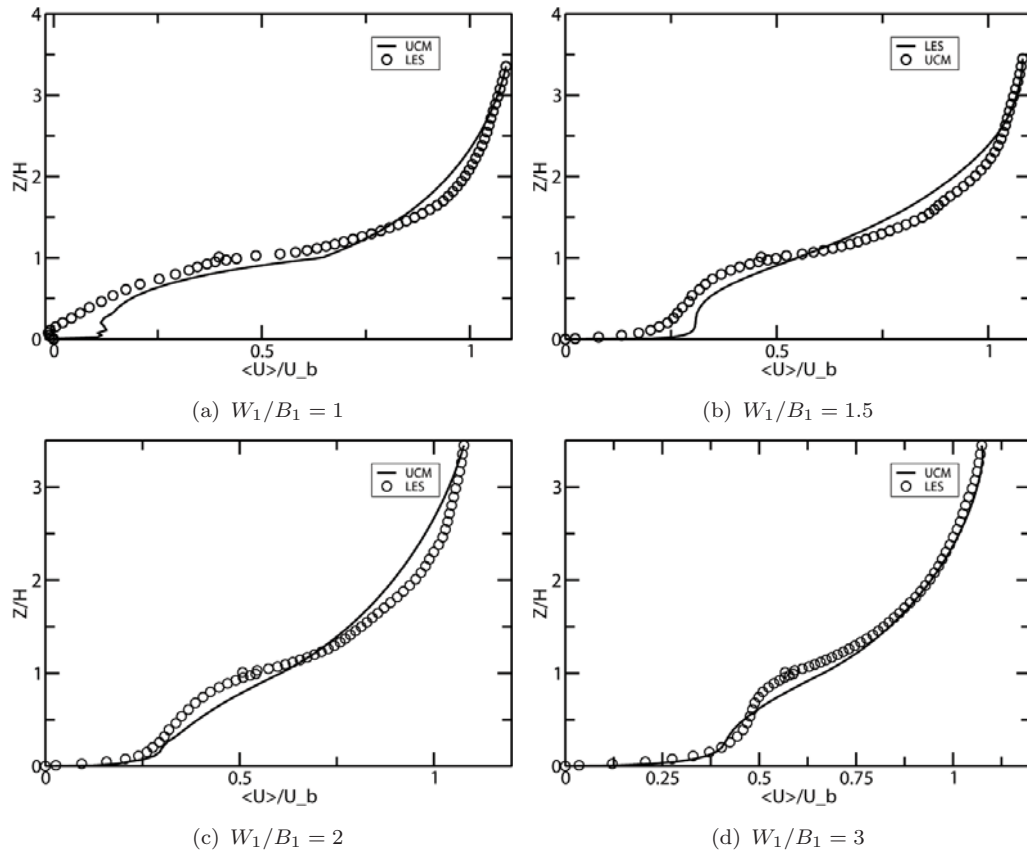
FIGURE 5.4: Comparision between the spatially averaged velocity profile obtained from LES and UCM

5.5.2 Offline tests

In Figure 5.6(a) a comparison between the velocity profiles predicted by the new model and the existing model due to Martilli is shown. From this we clearly observe that the old model considerably over predicts the velocity inside the canopy suggesting that the sources in the momentum and energy equations are in error, whereas the prediction by the new model clearly reflects the presence of buildings. We have also tested the sensitivity of the velocity profile inside the canopy to the building width to street width ratio , Figure 5.6(b). Quite expectedly the flow is retartded more when the streets are narrower.

(a) $W_1/B_1 = 1$

(b) $W_1/B_1 = 1.5$

(c) $W_1/B_1 = 2$

(d) $W_1/B_1 = 3$
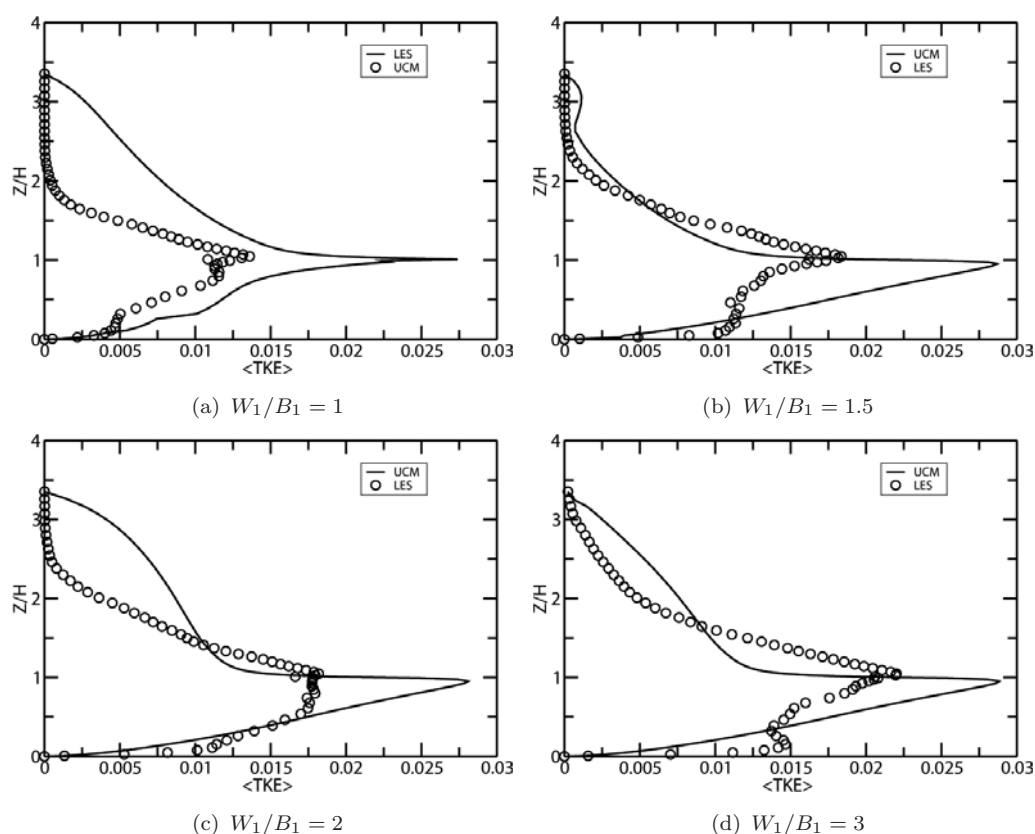
FIGURE 5.5: Comparision between the spatially averaged turbulent kinetic energy profile obatined from LES and UCM

5.5.3 Validation of the wall model

Two tests were conducted for both a steady and an unsteady case. In the first the inner and outer surfaces were maintained at two different temperatures. A comparison between the model result and the analytical result is shown in Figure 5.7(a). To test the accuracy of the model in an unsteady case a slab of a particular thickness initially at a temperature of $30C$ was suddenly subjected to a temperature of $250C$ on both the ends. A comparison of the time evolution of the temperature profiles predicted by the model and the analytical solution is presented in Figure 5.7(b), again showing perfect agreement.
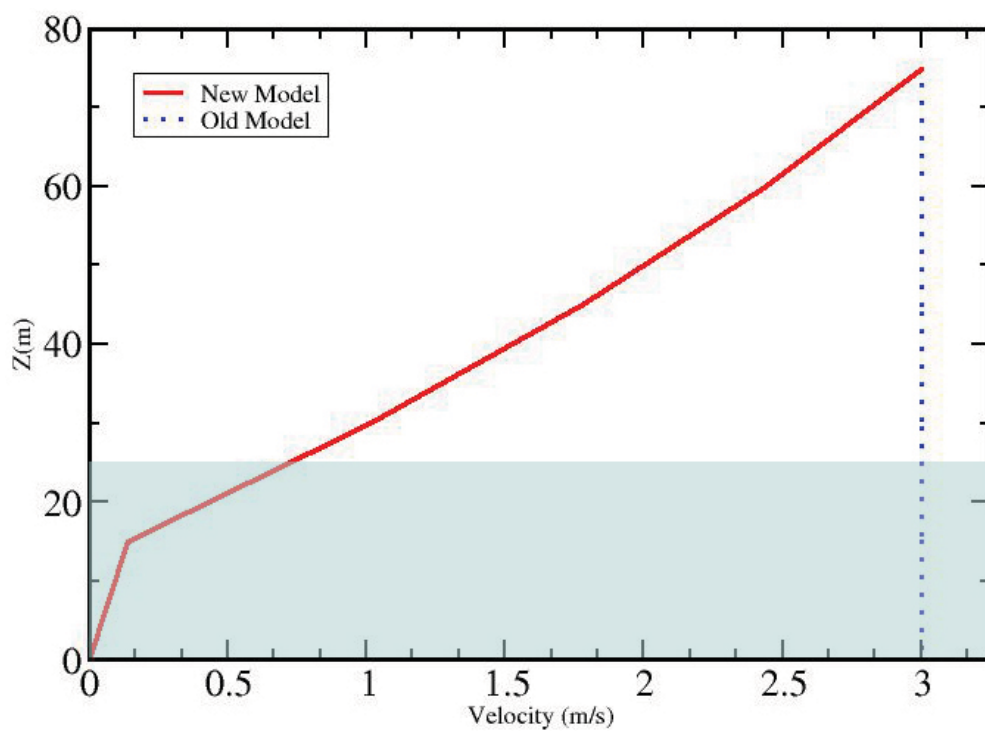
(a) Comparison between the new UCM and martilli's model
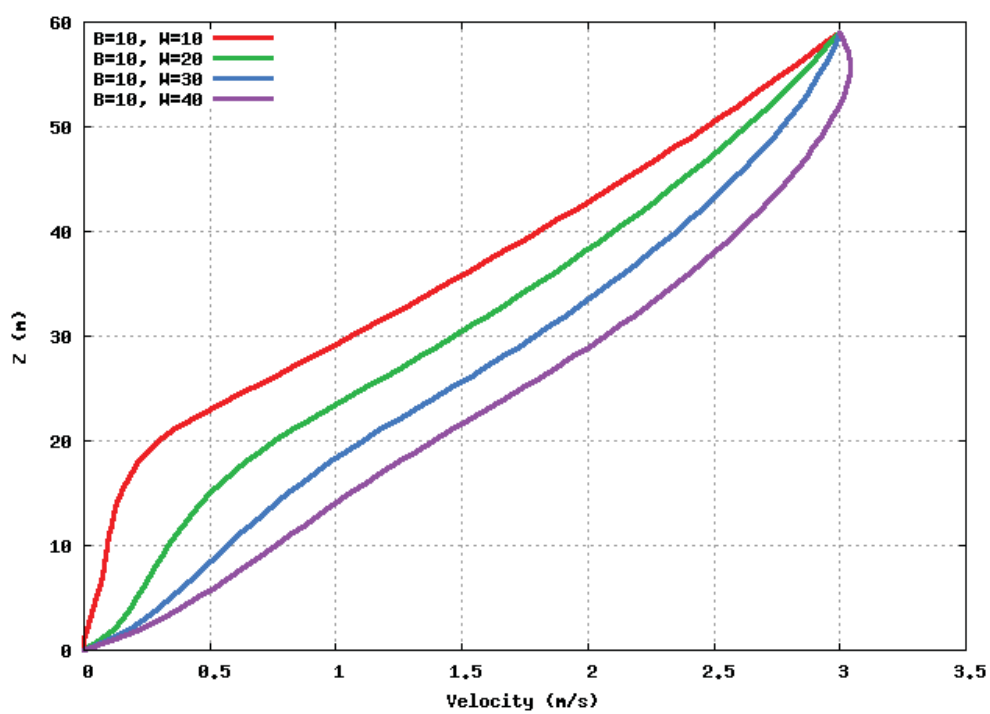
(b) Effects of changing the building to street width ratio

FIGURE 5.6: Off line tests

(a) Steady temperature profile   (b) Unsteady Temperature profile
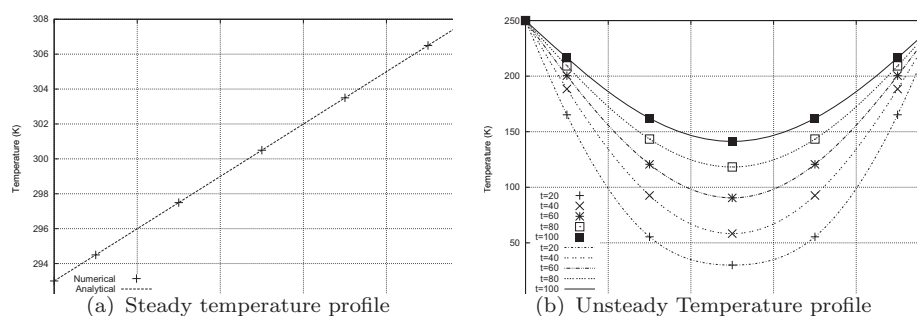
FIGURE 5.7: Comparison between the numerical and analytical results
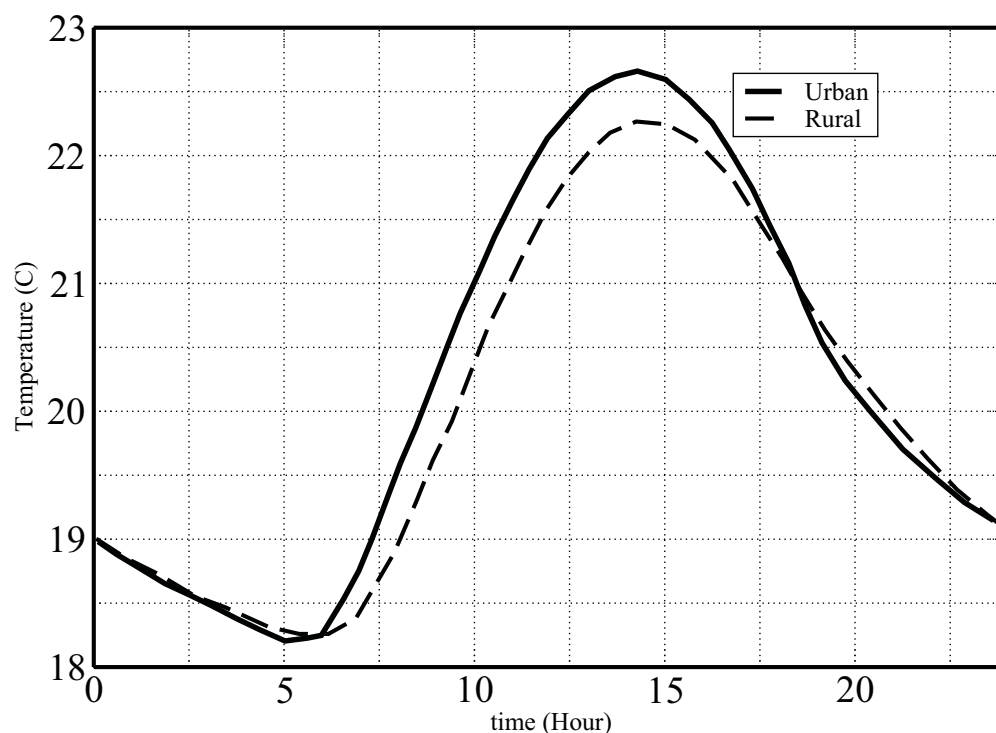
FIGURE 5.8: Daily profile of the temperature in the canopy

5.5.4   Daily profile of the temperature in the canopy

The daily profile of the temperature at $2m$ height in the canopy has been calculated with and without the Urban Canopy Model. In the urban case the area was assumed to be made up of a regular array of cubes with dimension $10m \times 10m$ having an inter-building spacing of $30m$ in both stream and spanwise directions. The temperature inside the building was set to $25C$ and the lower boundary condition was set $2m$ below the ground. The hypothetical test area was located in Basel and the radiation was computed assuming the mid June conditions. A geostrophic

wind of $15ms^{-1}$ and an initial lapse rate of $0.004Km^{-1}$ were introduced. The calculations was executed for 3days, and the result from the last day is presented so that the effects of initialization is minimal.

Figure 5.8 shows the effects of introducing the urban parameterization. Quite expectedly the temperature in the canopy has increased as a result of urban parameterization. This is due to the extreme retardation of flow caused due to the presence of urban structures and trapping of more radiation. The relatively stagnant air thus has more time to exchange energy with the buildings, thus becoming warmer. The lag in heating can be explained by the change in the thermophysical properties of the built material, particularly the specific heat capacity. These tendensies thus concur with those observed in the empirical UHI studies discussed in Chapter 1.

5.6 Linkage with the Mesoscale Model

The Urban Canopy Model, as explained in the last section, takes its boundary condition from the Mesoscale Model at 3.5 times the height of the highest building. The Urban Canopy Model, using these boundary conditions, computes the source or sink terms at the urban grid. These values are then interpolated back to the Mesoscale grid where they form the source or sink of the corresponding equations (mass, momentum and energy).

5.6.1 Results from the UCM coupled to the Mesoscale Model

In this section we present a sequence of simulation results demonstrating the added value of the new multi-scale modelling methodology. For this we have chosen the city of Basel. The meteorological data for forcing the model, landuse and topology following the procedures described in Chapter 7. In Figure 5.9(a) we have assumed
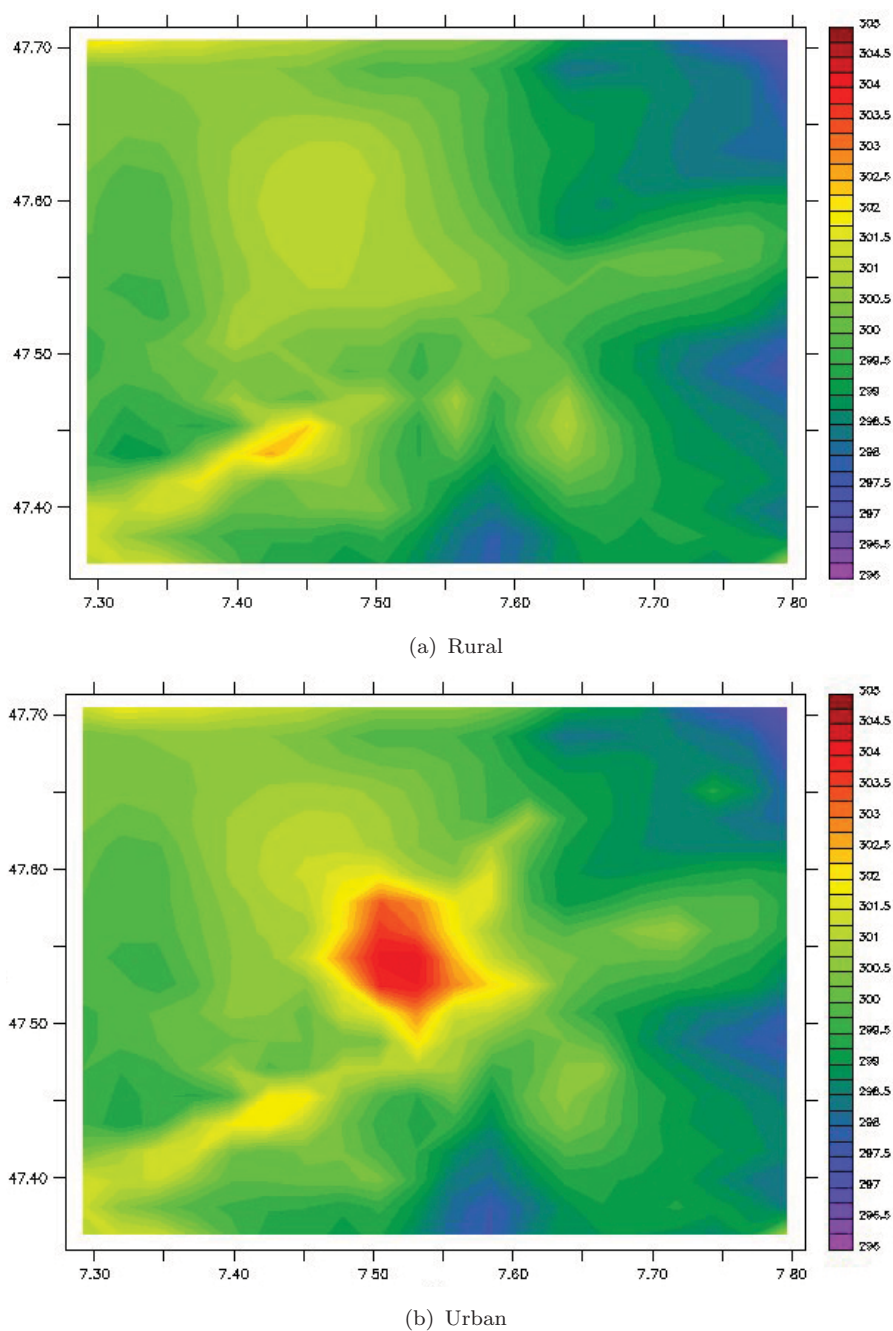
(a) Rural

(b) Urban

FIGURE 5.9: Contours of temperature (K)

a hypothetical situation where the whole of Basel and its surrounding area is 100% rural, implying no urban structures. In Figure 5.9(b) we present the impact of introducing a simplified urban representation of the city; the result corresponding to midday at a height of 5 meters from the ground. It should be noted here that the city has been represented by a regular array of cubes each of dimension $10m \times 10m$ with inter-building spacing of $30m$ each of height $15m$. The aim here is just to

show the impact of the introduction of this new canopy model. One can clearly see a rise in temperature in and around the city. Owing to the increased absorption of radiation by the urban structures, to the change in the thermophysical properties of the surfaces and a retardation of air flow in the city. The UHI intensity is around 5-6°C which can have a significant impact on energy demand for cooling or heating. Replacing the UCM model of martilli by the new model leads to a
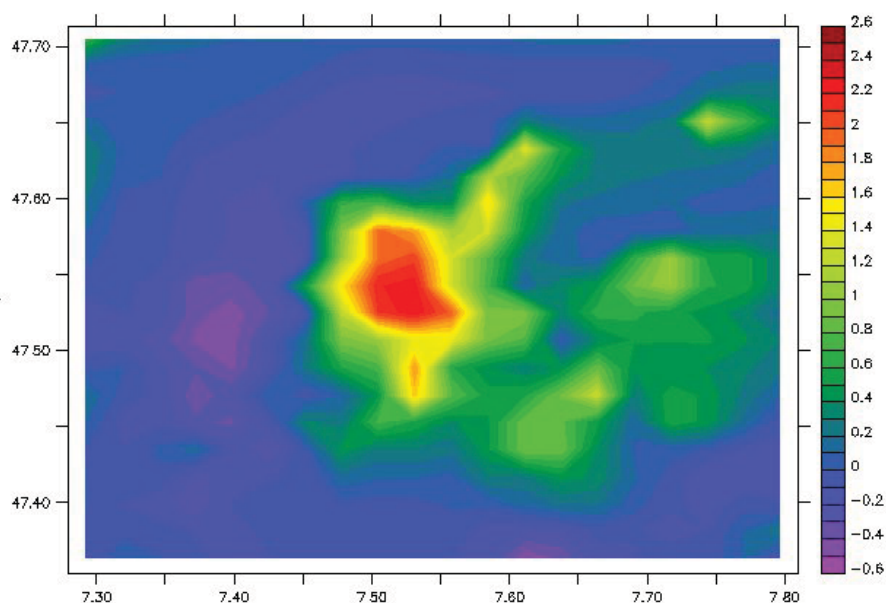
FIGURE 5.10: Relative difference in air temperature (in K) by substituting the Martili's UCM with the new UCM

further increase of temperature in the city. This is quite expected. We already saw that the model of Martilli overestimates the velocity in the canopy which implies that the heat emmitted or generated by the urban structures was more quickly exported by convection. In the new model the flow is retarded and hence the heat accumulates inside the canopies thus increasing the temperature of the air. Figure 5.10 shows the change in temperature by replacing the model of Martilli with the new model.

5.7 Conclusion

In the present chapter we have presented the development of a new Urban Canopy Model based on the results of Large Eddy Simulation explained in the last chapter. It has been shown that the new UCM predicts the spatially averaged velocity quite well when compared against LES data. However, for very narrow canopies the prediction is not very good especially near the ground. The effect of changing the building width to street width ratio was shown followed by the effect of the urban parameterization on the temperature profile inside the canopy in a hypothetical city. The model was then applied to a "real" city which has the same topography and landuse as Basel but was assumed to be comprised of simplified geometry. Finally, the difference in the model result (between Martillis model and the new one) for temperature was shown. From these comparisons the added value of a more rigorous treatment of momentum fluxes within the urban canopy is immediately apparent. One further distinguishing feature between this and previous UCMs is that this new model also allows us to represent urban geometries in a more realistic way (building and street width may differ in two directions). Thus we can divide a city into different types of urban class, each characterised by the aforementioned quantities as well as the thermophysical properties of the built material. Thus we have the flexibility to represent each mesoscale grid with a unique urban class having unique geometric and thermophysical properties for improved simulation resolution. A new method for estimating these geometric characteristics is explained in the next chapter. It should however be pointed out here that although this new UCM can be applied for simulating stable, unstable and neutral boundary layer, the validation against LES data has been conducted only for neutral boundary layer. This is partly due to the unavailability of experimental data.

Chapter 6

Simplification of Complex Urban Geometry

The parameterization that was developed in the last chapter can be applied to only those urban geometries which can be represented by a regular array of cubes. However, in a real city we tend to encounter complex geometries which do not obviously match such simplified geometries. Yet all of the urban parametrizations thus far developed share the assumption that a city is made up either of a regular array of cubes or of infinitely long canopies. The inputs to these models which include street width, building width, building density and a statistical representation of the buildings' heights, are generally obtained through quantitative field surveys (which are very slow and time consuming to perform) or qualitative estimates. But in performing this geometric abstraction there is no way to ensure that the total built surfaces and volumes of the simplified geometry match those of the actual city or more importantly that the energy and momentum exchanges are equivalent. In this chapter we aim to test the central hypothesis that cities can be accurately represented by a regular array of cubes or canopies. For this we investigate, for a particular scenario, the effects of complexity in urban geometry on the spatially averaged drag forces and shortwave radiation exchange. For drag computation we used the Immersed Surface Technique while for computing

the incident radiation we used the Simplified Radiosity Algorithm (as described in Chapter 3). After testing the above hypothesis we propose a new approach for fitting an array of cubes to any complex (realistic) geometry, so that new or existing urban parameterization schemes can be used with confidence.

6.1 Background

Almost all multilayer canopy models are mathematically represented by the following set of equations

$$\frac{\partial u}{\partial t} = \frac{\partial}{\partial x}\left(k_z \frac{\partial u}{\partial x}\right) + SOR_u \tag{6.1}$$

$$\frac{\partial v}{\partial t} = \frac{\partial}{\partial x}\left(k_z \frac{\partial v}{\partial x}\right) + SOR_v \tag{6.2}$$

$$\frac{\partial \theta}{\partial t} = \frac{\partial}{\partial x}\left(k_z \frac{\partial \theta}{\partial x}\right) + SOR_\theta \tag{6.3}$$

The basic assumption here is that a city is represented by a regular array of cubes, as shown in the Figure 6.1, and the terms k_z, SOR_u, SOR_v and SOR_θ represent the effects of drag, shear and other sources which are parametrized in terms of the geometric parameters $B1, B2, W1, W2$ and street orientataion. Moreover, the term SOR_θ represents the energy exchange with the buildings. Quite obviously it depends on the surface temperatures of the wall, ground and roof. The thermophysical properties of the material constituting these three types of surface may be quite different and hence the differential heating of these surfaces may lead to very different source terms. Keeping these things in mind we try to test the above stated basic hypothesis underlying almost all the multilayer canopy models.
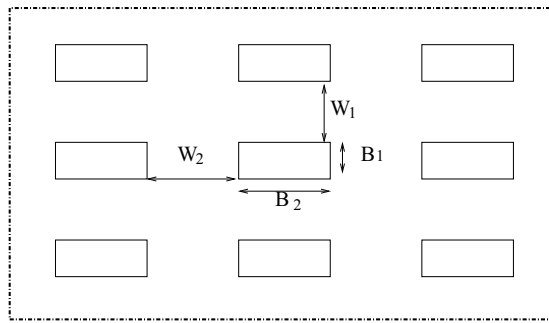
FIGURE 6.1: Regular array of cubes in an aligned configuration
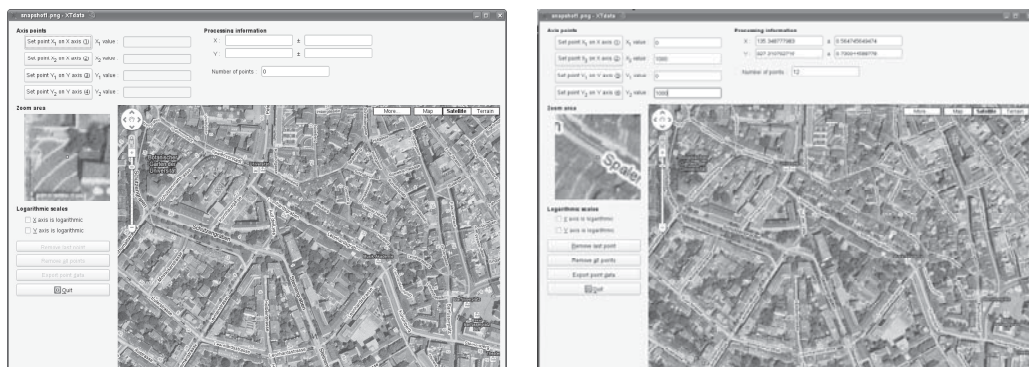
(a) Interface

(b) Interface

FIGURE 6.2: Sketching tool

6.2 Testing the hypothesis

As noted in the introduction deducing the geometric parameters of simplified representations of urban geometry can be a time consuming and erroneous process. To assist this process a tool was developed to sketch the geometry using ariel views of the city obtained from google earth, with building height being a user input, which may be estimated or calculated, for example using LIDAR data. In Figure 6.2 one can see how the geometry can be sketched and scaled to approximate actual dimensions. Clearly, the accuracy of this method depends on the clarity of the image and the patience of the sketcher.

TABLE 6.1: Geometric characteristic of built surfaces in the concerned domain

Horizontal built area (Roofs)	$144000m^2$
Vertical buit area (Walls)	$432000m^2$
Horizontal buit area (Ground)	$606000m^2$
Building Height	$15m$
Total Built Volume	$2160000m^3$

6.2.1 Test Set-up

For this study we have chosen a part of the city of Basel which has a dimension of $1000m$ by $750m$. A good approximation of the real geometry is sketched and it is assumed that all the buildings have a height of $15m$. Many of the buildings in this part of Basel, a very dense city, have been constructed to this maximum height, although they do not necessarily all have flat roofs. Nevertheless, this assumption doesn't undermine our ability to test the concept presented in this chapter. The total built vertical and horizontal surface areas are presented in Table 6.1. Three simplified representations of this geometry are also considered in the present investigation. These we refer to as long canopies, simple cubes 1, and simple cubes 2. The long canopies representation of the city consists of rows of 10 terraced buildings each of dimension $500m \times 30m$, with an interspacing of $67m$, as shown in Figure 6.3(b). Simple cubes 1 consists of 20×18, cubes each of dimension $20m \times 20m \times 15m$ and aligned in a regular array with a spacing of $30m$ in the stream wise direction and $20m$ in the span wise direction, as shown in Figure 6.3(c). Similarly the simple cubes 2 representation consists of 20×18 cubes each of dimension $26.7m \times 15m \times 15m$ aligned in a regular array with a spacing of $23.3m$ in the stream wise direction and $25m$ in the span wise direction, as shown in Figure 6.3(d). This simulation was conducted for the 7th of January.

(a) Rendered Complex Geometry

(b) Rendered Long Canopies

(c) Rendered Simplified Geometry

(d) Rendered Simplified
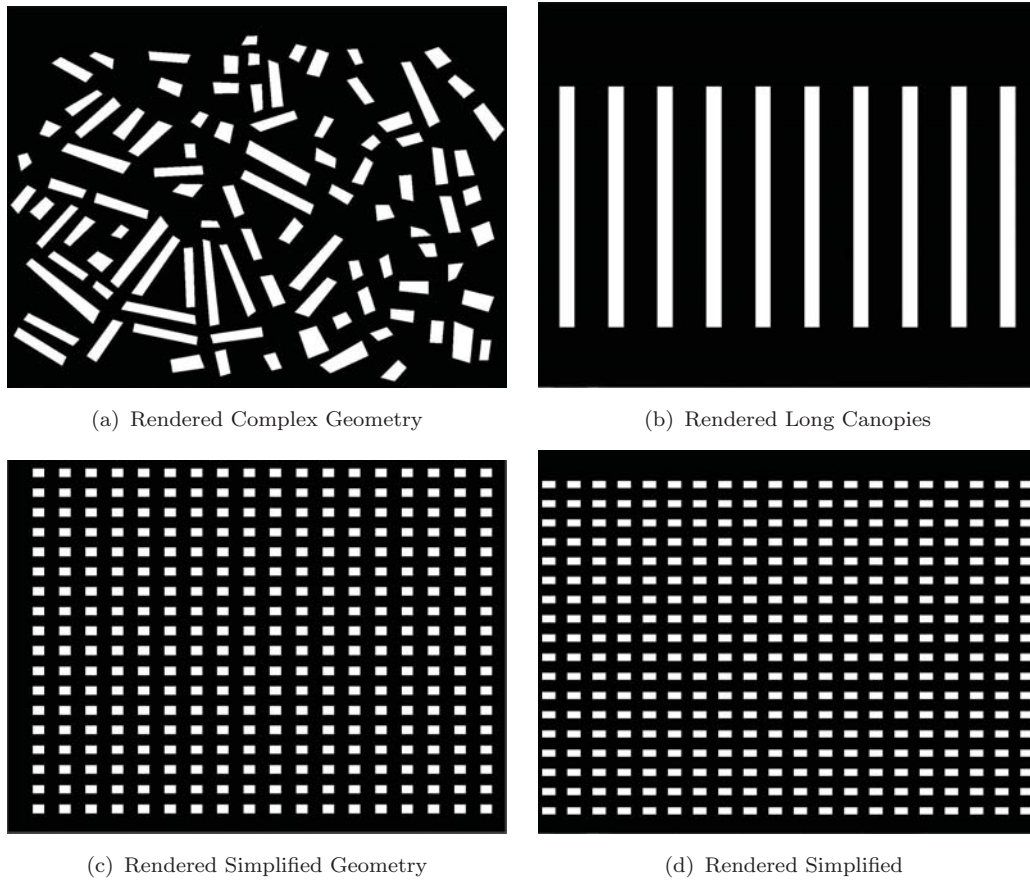
FIGURE 6.3: Rendered Simplified Geometry

TABLE 6.2: Number of triangles to discretize different surfaces

	Roofs	Ground	Walls
Complex	992	870	2658
Simple cubes 1	2160	2242	7520
Long canopies	420	284	400
Simple cubes 2	2160	2396	8640

6.2.2   Radiation

6.2.2.1   Set up:

For radiation computation the surfaces in each of the representations are tessellated into smaller surfaces (Figure 6.4). The details of the tesselization are shown in Table 6.2. The tesselized geometries are show in Figure 6.4

(a) Surface tesselization of Complex Geometry

(b) Surface tesselization of Long Canopies

(c) Surface tesselization of Simple Cube 1

(d) Surface tesselization of Simple Cube 2
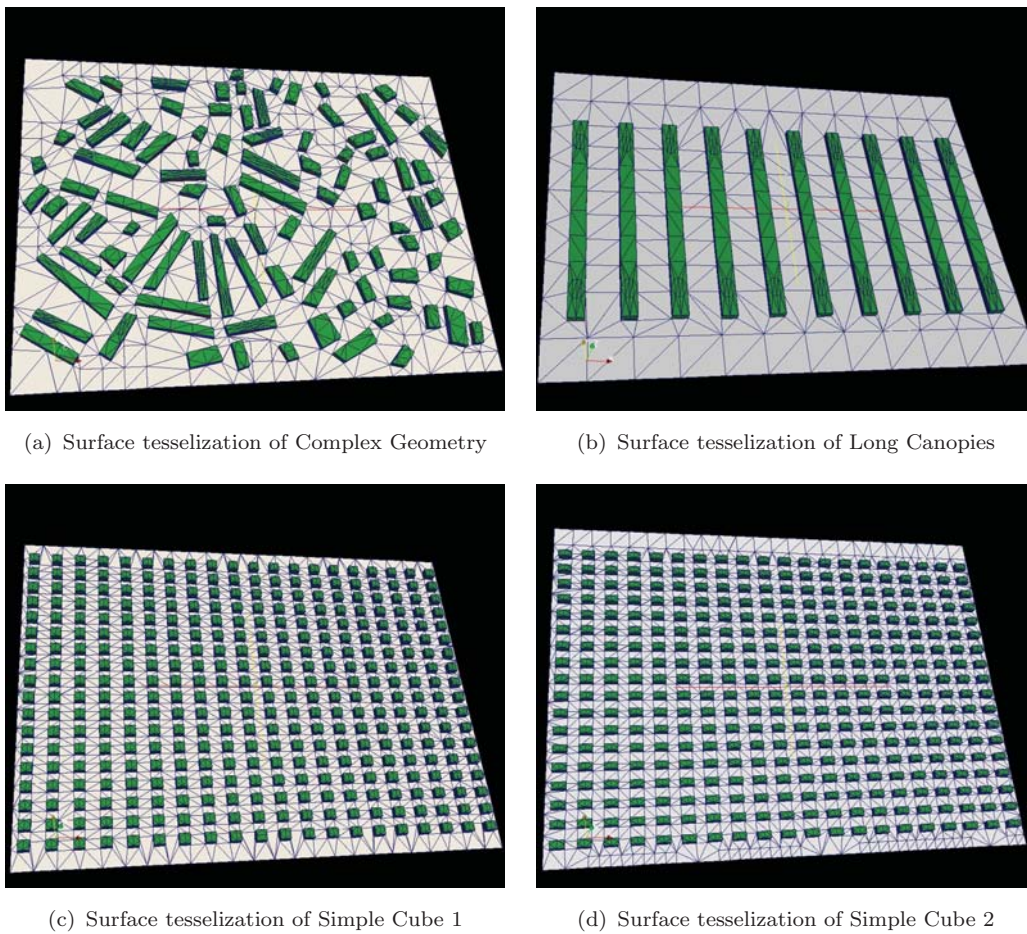
FIGURE 6.4: Surface tesselization of geometries

6.2.2.2 Results:

All domains of the same size will have the same amount of solar radiation entering them. However, for mesoscale modeling, the correct calculation of the distribution of the radiation amongst the wall, roof and ground surfaces is very important as this determines the total absorption of radiation within our domain and the corresponding energy that is transferred to the adjacent air. Variations in the spatial distribution of absorbed solar energy may also modify momentum transfers. From Figure 6.5, 6.6 and 6.7 we make the following observations:

1. Roofs: Since the horizontal roof surface areas in all four of our representations are the same and all the buildings are of the same height (and hence there is
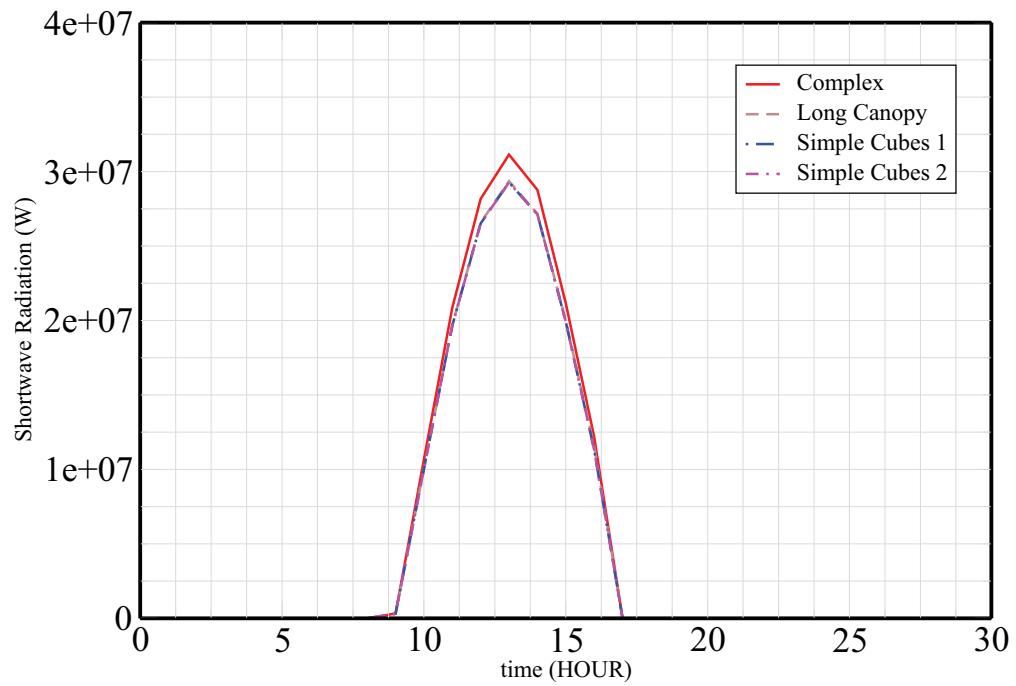
FIGURE 6.5: Comparison of the amount of Shortwave Radiation incedent on roof every hour for the four cases
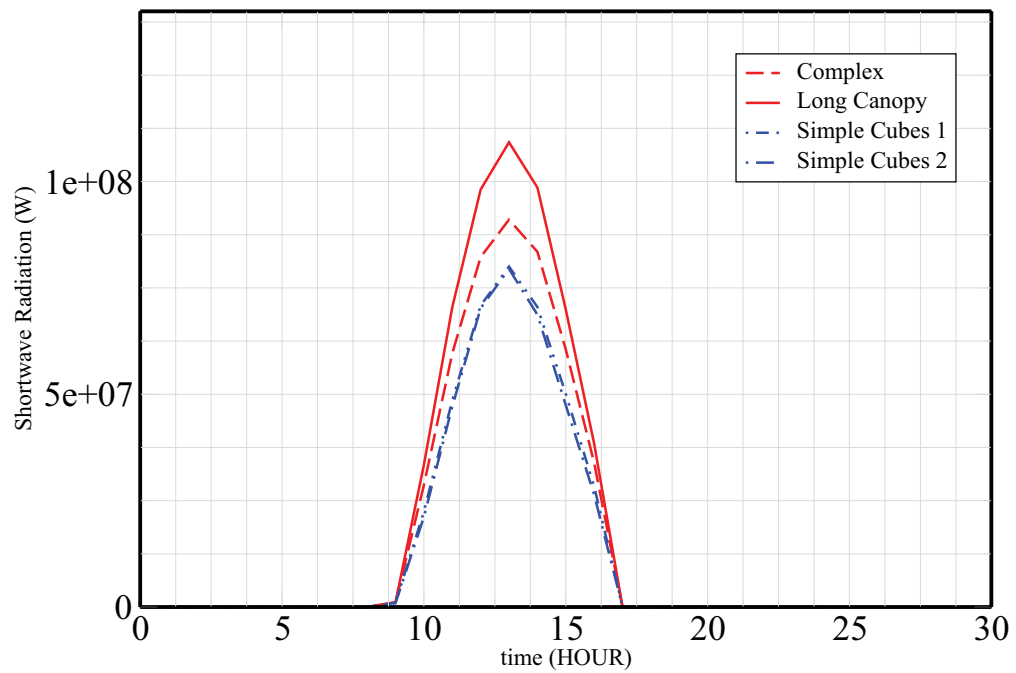
FIGURE 6.6: Comparison of the amount of Shortwave Radiation incedent on ground every hour for the four cases
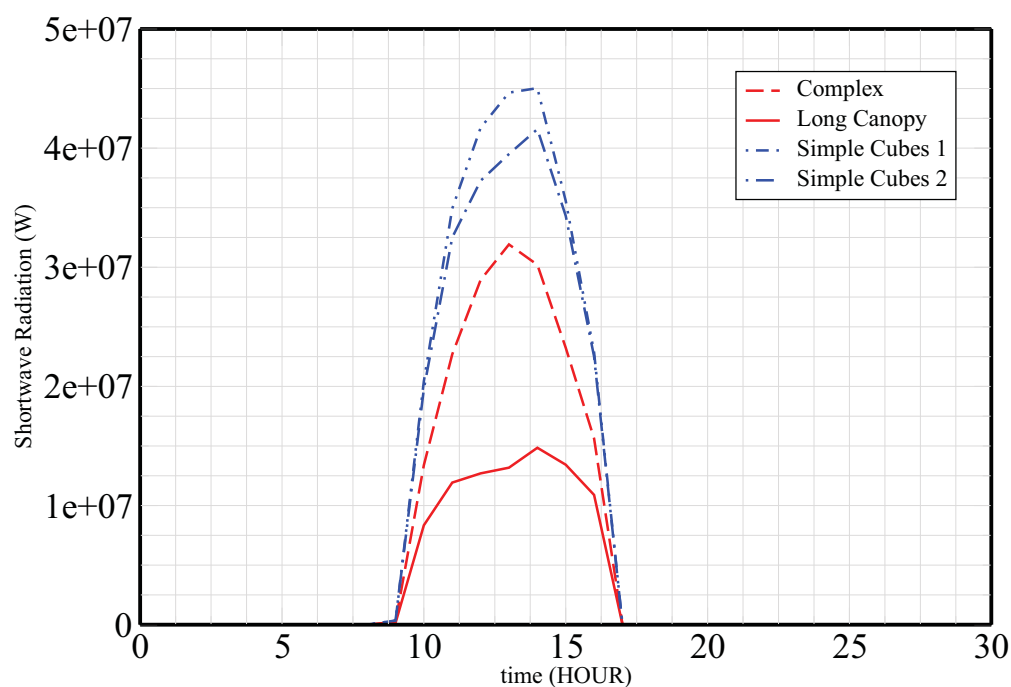
FIGURE 6.7: Comparison of the amount of Shortwave Radiation incedent on wall every hour for the four cases

no obstruction to the sky) we observe that the amount of radiation absorbed during the whole day is similar, as expected.

2. Ground: In the particular case of long canopies the ground receives more solar radiation than either of the cube layouts, as views to the sun and sky are relatively unobstructed. In the complex representation these views are relatively obstructed so that the radiation incident on the ground decreases. In the case of the two cube representations views are even further obstructed, so that even less solar radiation is incident on the ground of our domain.

3. For walls: The two simplified cubic representations receive more shortwave radiation than the complex and long canopy representation. This is due to an increased reflected contribution and an increased south facing surface area. Thus, for this particular day, the walls in the simplified representation will be much hotter than in the complex one. The opposite will be true for the ground surfaces. This will result in very different surface temperatures

(a) Mesh for Complex Geometry

(b) Mesh for Simple Geometry

(c) Mesh for Simple Geometry

(d) Mesh for Complex Geometry
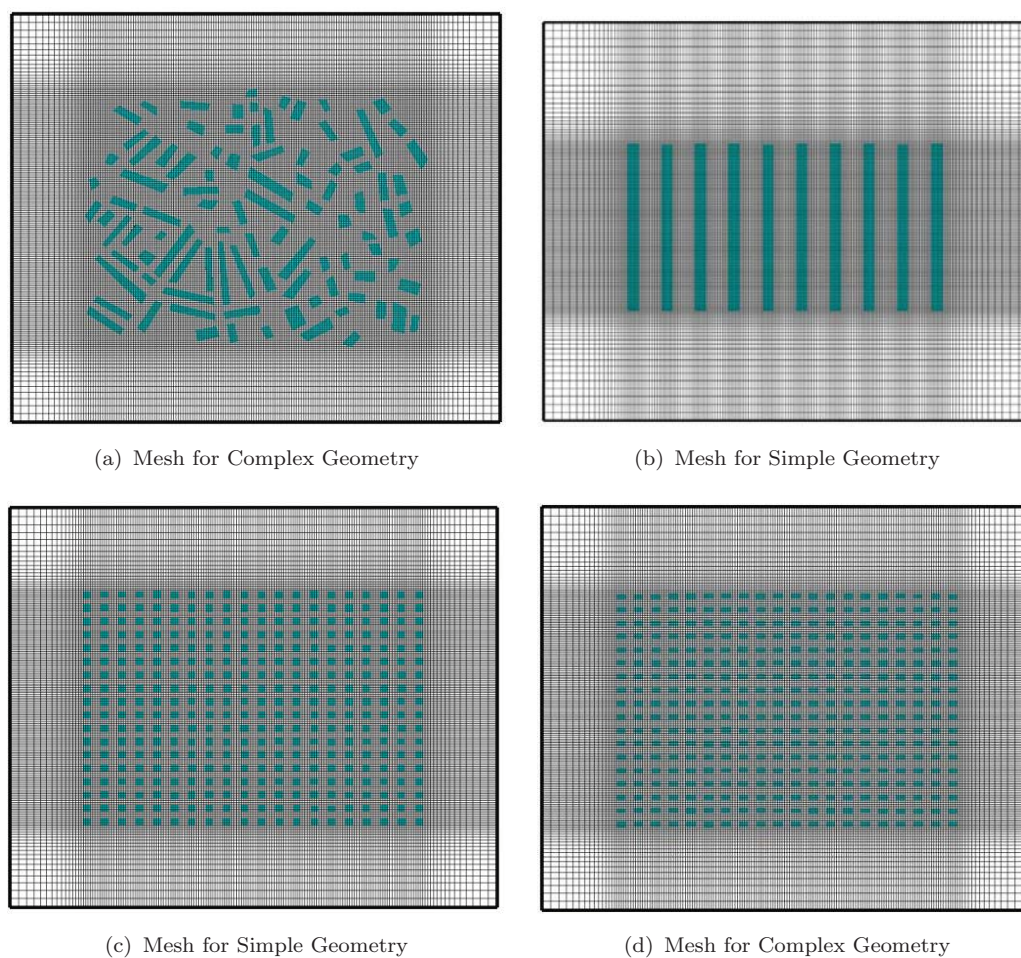
FIGURE 6.8: Mesh for CFD simulations

of walls and ground and may influence the energy exchange in a significant way.

6.2.3 CFD simulations

6.2.3.1 CFD simulation set up

For the CFD simulations the geometrical representation is the same as for the radiation calculations. However, the domain has been extended at all four boundaries by an additional 200m, to allow the inflow to develop before encountering urban structures. The domain is discretized into $175 \times 175 \times 40$ cells (stream wise $\times$ span wise $\times$ vertical) (Figure 6.8). For the complex geometry one more simulation was

(a) Complex Geometry

(b) Simple Geometry: long canopy

(c) Simple Geometry: Cube 1

(d) Simple Geometry: Cube 2
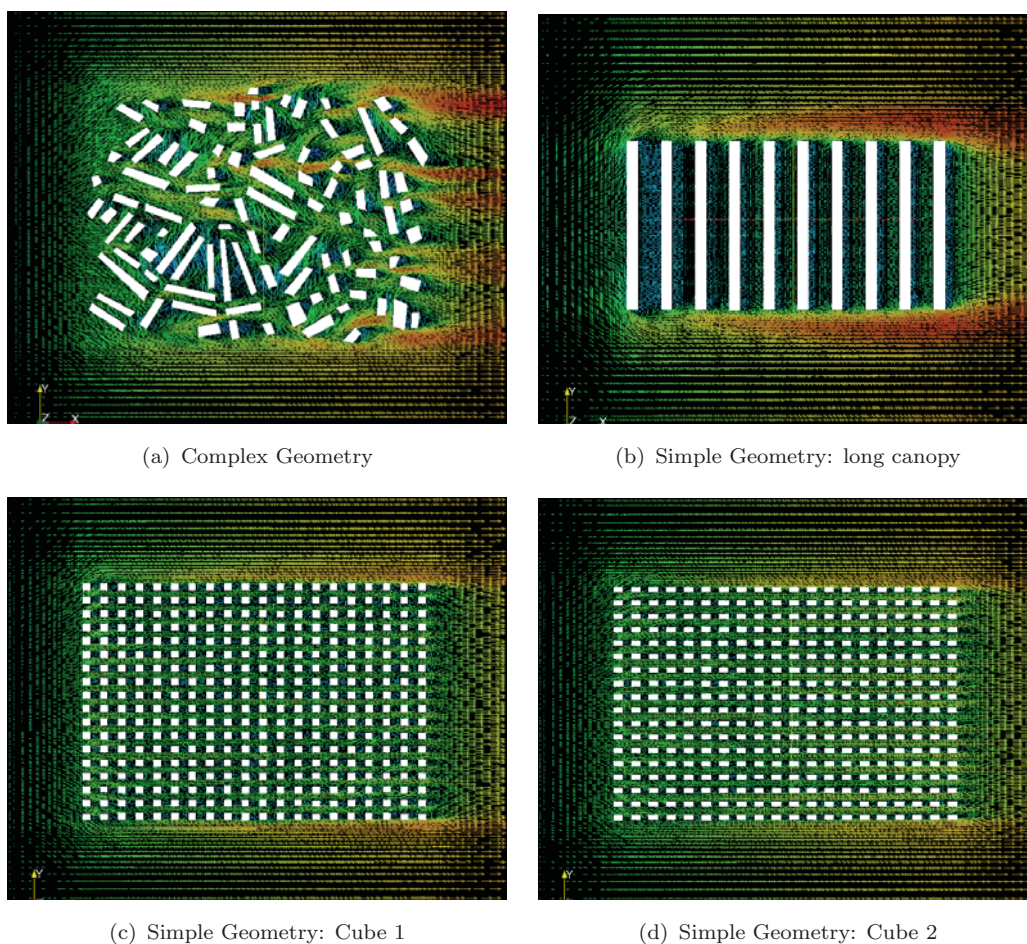
FIGURE 6.9: Velocity field at 5.6m above the ground level

conducted using $225 \times 225 \times 60$ cells. Very little difference was observed implying grid independence and hence subsequent simulations (presented in this chapter) for other geometries were conducted using the former resolution. An inlet boundary condition with a $1m/s$ velocity in the streamwise direction is imposed on the left side of the domain and an outlet boundary condition is applied at the right end. For the bottom side of the domain a wall boundary condition is specified and for the rest of the surfaces symmetry boundary conditions are imposed. The turbulence model used in this simulation is the standard $k - \epsilon$ model, while the convective scheme used for density and velocity is the HYBRID. A preconditioned (multigrid) GMRES pressure solver is used for solving for the pressure field. The flow is solved in a steady state with convergence criteria of $E - 4$ for velocities and kinetic energy and $E - 03$ for dissipation.

TABLE 6.3: Space averaged drag (F_x, F_y) and shear forces(S_x, S_y)

-	F_x	F_y	S_x	S_y	$S_x + F_x$	$F_y + S_y$
Complex	8207	157	985	2.5	9194	160
Simple cube 1	4931	-46	754	1.3	5658	-45
Long Canopies	1409	38.52	1424	1.95	15507	40.5
Simple cube 2	2911	-35	665	-3	3577	-38

6.2.3.2 CFD results

In Figure 6.9 we present the velocity field for all four geometric representations at a height of $5.6m$ above the ground plane. The more complex (real) representation is characterized by the formation of large vortices formed in the inter-building spaces. There is also a tendency for the flow to be deflected in the spanwise direction, due to the irregular orientation of the buildings. Long canopies strongly retards the flow, which tends to stagnate within the canopies. There is also an acceleration of flow near the top and bottom edge of the long blocks. Within the simplified representations, Cube 1 and 2, vortices are formed on the leeward side of the cubes, which are small and well isolated from each other. Also, because these obstructions are non-continuous the fluid motion remains essentially unidirectional in the streamwise sense. These observations are also evident from the magnitude of the spatially averaged drag forces presented in Table 6.3

6.3 Concept of an Equivalent City

From the previous section it appears to be clear that the form and layout of buildings has important implications for the imposed drag forces and the distribution of absorbed radiant energy which might lead to differential heating of surfaces and hence to differences in the total energy exchange with the surrounding air. It should be noted here that we have not yet analyzed the long wave radiation distribution which, being a function of surface temperature, may be more influenced by the geometric complexity. It is thus important to identify an arrangement of a simplified geometry (as used in urban parameterization scheme) for which these

two quantities (drag and radiation absorption) are roughly equivalent to those experienced by the corresponding real geometry. For this purpose we introduce a new technique for fitting such an equivalent simplified geometry. (Figure 6.10). In this we define *An "Equivalent Geometry" as that geometry which has the same built volume, horizontal and vertical built area, offers the same drag and absorbs the same radiation on vertial and horizontal surfaces as the complex/real representation.*
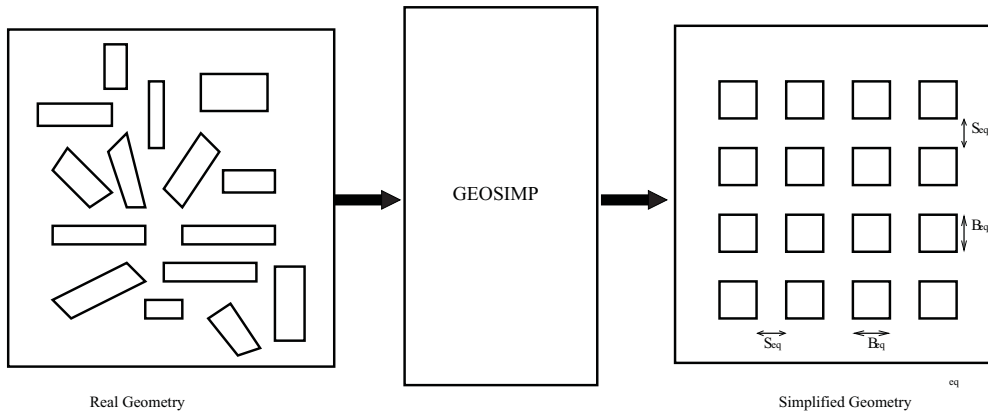
FIGURE 6.10: Simplification of Complex Urban Geometries

Using the Sketching tool as shown in Figure 6.2 the region to be simplified is loaded in to the interface. The scale of the domain is selected and then the outline of each building geometry is sketched. The three dimensional solids are then created given the corresponding building height (kept constant at present). This geometry is then automatically digitalized and parsed on to the solver, which then identifies the corresponding simplified geometry. The constraints here are that the total built surface area and volume in the domain consisting of complex geometries should be equal to those of the simplified form. Mathematically:

$$S_{complex} = S_{simplified} \tag{6.4}$$

$$V_{complex} = V_{simplified} \tag{6.5}$$

And the objective functions to be minimized are:

$$f1 = Radiation^{wall}_{complex} - Radiation^{wall}_{simplified} \tag{6.6}$$

$$f2 = Radiation_{complex}^{ground} - Radiation_{simplified}^{ground} \qquad (6.7)$$

$$f3 = Drag_{complex} - Drag_{simplified} \qquad (6.8)$$

6.4 Algorithm

The whole algorithm can be enumerated as follows

Step 1: Sketch the complex geometry using the sketching tool

Step 2: Load the digitalized geometry and compute the volume, horizontal and vertical surface area of each building.

Step 3: Compute the total built volume and surface area in a city.

Step 4: Compute the radiation incident on vertical and horizontal surfaces

Step 5: Compute the space averaged drag and shear forces for the whole domain (with complex geometry)

Step 6: Using the number of buildings sketched n, total volume V compute the building widths ($B1$, $B2$) and street widths ($W1$, $W2$) within the prescribed limits which can be the maximum and minimum dimensions of the buildings found in the domain of investigation

Step 7: Generate a simplified scence in terms of a regular arrray of cuboids

Step 8: Compute the total radiation incident on the simplified scene

Step 9: Compute the space averaged drag and shear forces for the whole domain (with simplified geometry)

Step 10: See if the objective functions are below the convergence criteria. If yes then you have the equivalent geometry, otherwise goto **Step 6** and iterate.

6.5 Result

After several iterations we have identified a geometry which satisfies our definition of "equivalent geometry" (Figure 6.12(b)) for our case study of Basel. We can see

TABLE 6.4: Drag, Shear and Total forces

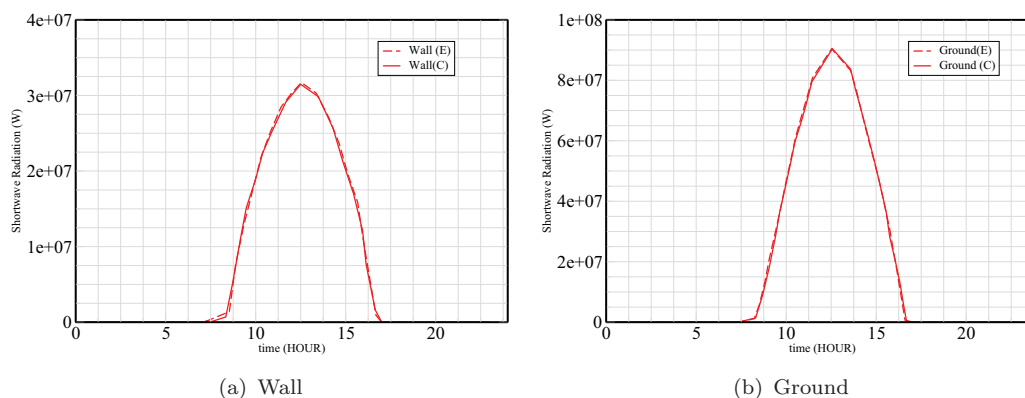| -	Fx	Fy	Sx	Sy	Fx+Sx	Fy+Sy
Complex	8207	157	985	2.5	9194	160
Equivalent	7731	-346	894	5.8	8625	-340

(a) Wall

(b) Ground

FIGURE 6.11: Shortwave radiation incident on different surfaces for wall and ground

from the Table 6.4 that the streamwise drag forces for both geometric models are comparable. Although the forces in the spanwise direction do differ, their magnitudes compared to the streamwise forces are negligible. Furthermore, from Figure 6.11 we see that the profiles of radiation incident on the ground and wall surfaces for the compex and equivalent representations are now precisely superimposed. The radiation incident on the roof surfaces is not presented: it is proportional to the horizontal roof surface areas, which are identical for both representations. The equivalent representation of the complex geometry is shown in Figure 6.12(b). Each cube in the equivalent representation has a dimension of $26.7m \times 15m \times 15m$ (Width $\times$ Breadth $\times$ Height). The West-East street width is $23.3m$ and it is aligned at an angle of 30 degrees to the east, while the South-North street width is $25m$ and is aligned orthogonal to the other street. This geometric representation can be used to substitute the complex representation shown in Figure 6.12(a)
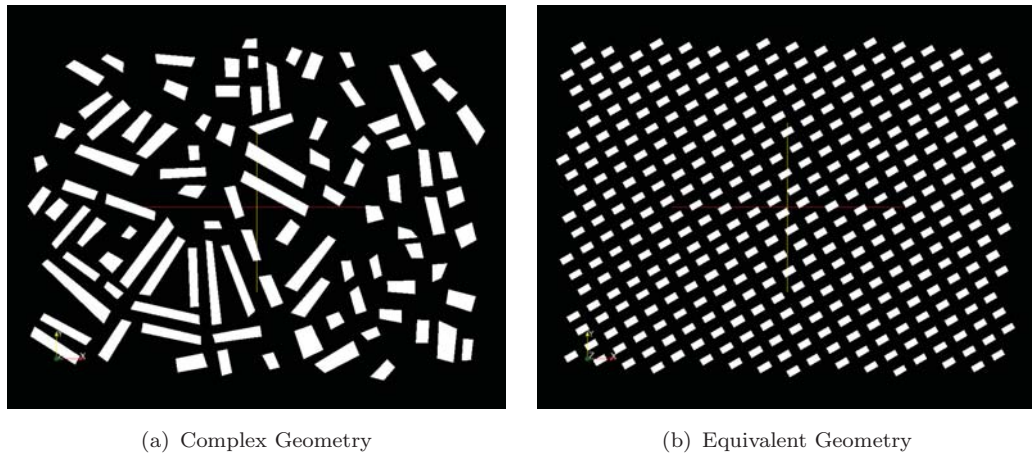
(a) Complex Geometry   (b) Equivalent Geometry

FIGURE 6.12: Simplification of Complex Urban Geometries

6.6 Conclusions

In this chapter the importance of the complexity of urban geometry on the spatially averaged quantities (radiation incident on walls, roofs and ground) and drag force is studied. It is found that the error in the estimation of these quantities can be quite significant. We then introduce and test a new algorithm for fitting an equivalent geometry (of the type used by urban canopy models) to any real complex geometry based on minimising the error in drag force and absorbed radiation. This new method may be used to calibrate the geometric inputs to any multilayer canopy model in a rigorous way. Although lidar data does exist for the city of Basel, the resolution (20cm) of this data is incompatible with our modelling needs - requiring a significant amount of geometric simplification. For this reason we have sketched the geometry of the complex city using google earth images and then extruded them to a particular height based on field measurement. However, the algorithm which is explained in this chapter can handle non-uniformity in building height so that with 3-D laser scanned geometries becoming more and more accessible we can further improve the accuracy of our equivalent representation.

Chapter 7

Application

In the present chapter we apply the Multiscale Modelling approach to a real three-dimensional configuration. The aim of the work in this chapter is to see if the newly developed approach can mimic the most important features of Urban Heat Island phenomena. A further aim is to study and evaluate the capability of the tool to be used as a city planning tool. For this, the model is applied to the city of Basel which is located in the North-Western part of Switzerland on the Rhine river, surrounded in the north-east by the German Black Forest, in the south by the jura range, and in the west by the French Vosges mountains. These surrounding mountains generate diurnal slope winds, and the corresponding topographic situation makes the area of Basel one of the warmest in Switzerland. Basel is Switzerland's third most populous city ($166, 209$ inhabitants (2008)). With $731, 000$ inhabitants in the tri-national metropolitan area (as of 2004), it is Switzerland's third largest urban area. Another important justification in choosing Basel for testing the model is the fact that an intensive measurement campaign was undertaken between August 2001 and July 2002. This project consisted of a large Urban Planetary Boundary Layer (PBL) experiment carried out under the auspices of the European COST 715 action. Its aim was to investigate the exchange processes occurring near the urban surface as well as the flows occurring in the upper part of the Urban Boundary
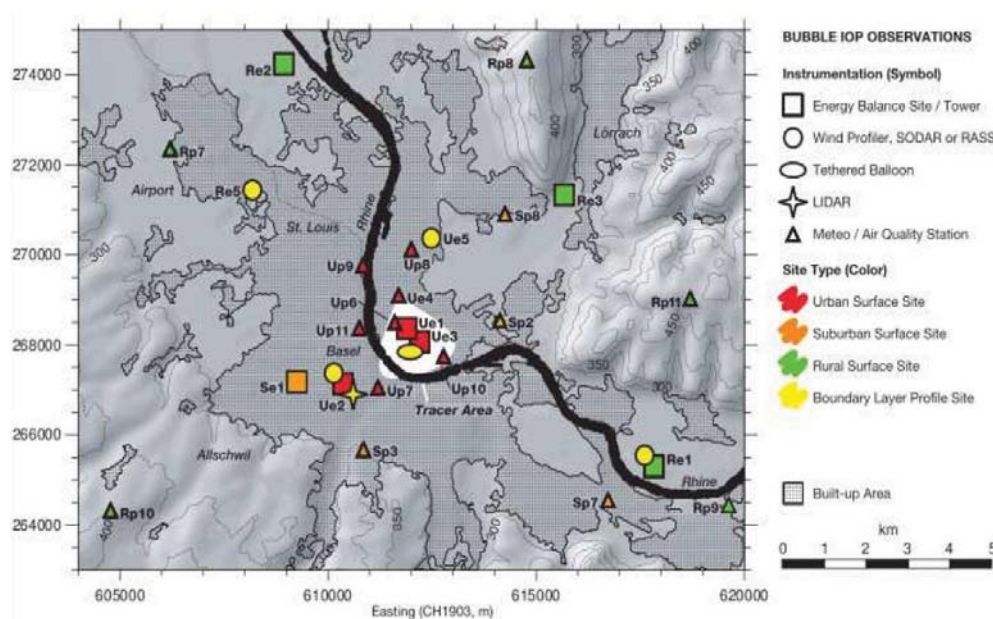
FIGURE 7.1: Measuring station in Basel Source: Bubble Project website

Layer (UBL). As one can see in Figure 7.1[1], different measuring weather stations were in use, located either on urban, suburban, or rural sites. A detailed list of the different stations is presented in Appendix B. The time resolution was 10 min for most of the measurements while a few stations had a resolution of 30 min. The principal urban site was "Basel-Sperrstrasse" (Ue1 in Figure 7.1), and was of particular interest due to its location within an urban canyon. A detailed description of the characteristics of this measuring site can be found in Roulet et al. (2005). The possibility of having direct access to a wide range of measured data,thus provides us with the considerable advantage to compare our numerical mesoscale model results to real observations.

7.1 Simulation Set-up

In this section we present the characteristics of the mesoscale domain and its discretization along with the way the model inputs are prepared. The model inputs consist of topographical and landuse information as well as the meteorological

---

[1]http://pages.unibas.ch

(a) $30km \times 30km$ (b) $15km \times 15km$

(c) $5km \times 5km$ (d) $1.5km \times 1.5km$

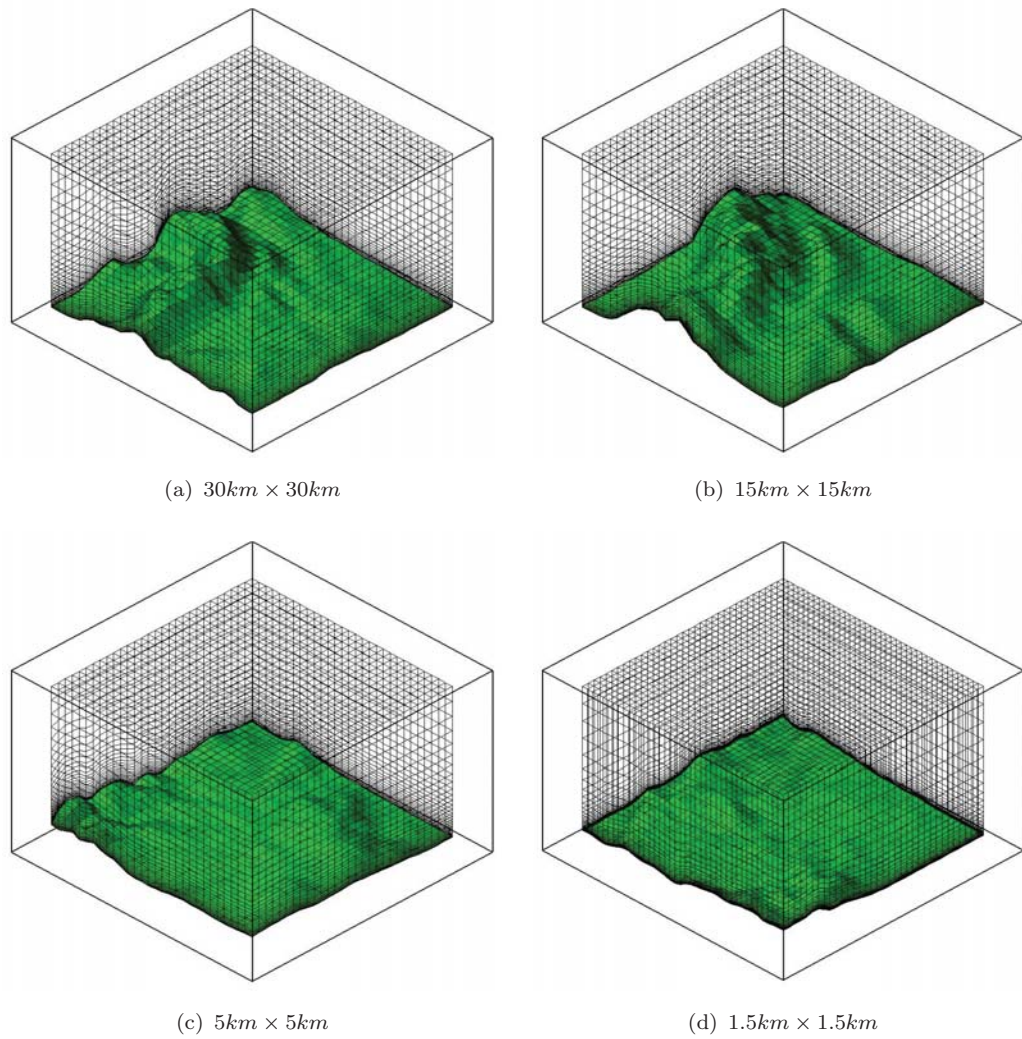FIGURE 7.2: Terrain following mesh

data used for forcing, and the thermophysical properties of built as well as natural environment (rural surfaces).

7.1.1 Time and duration of simulation

The starting time of our simulation was $00:00H$ on 25.06.2002. The simulation was run for three days. The first 6 hours were considered the initialization period and hence was not considered in the following analysis.
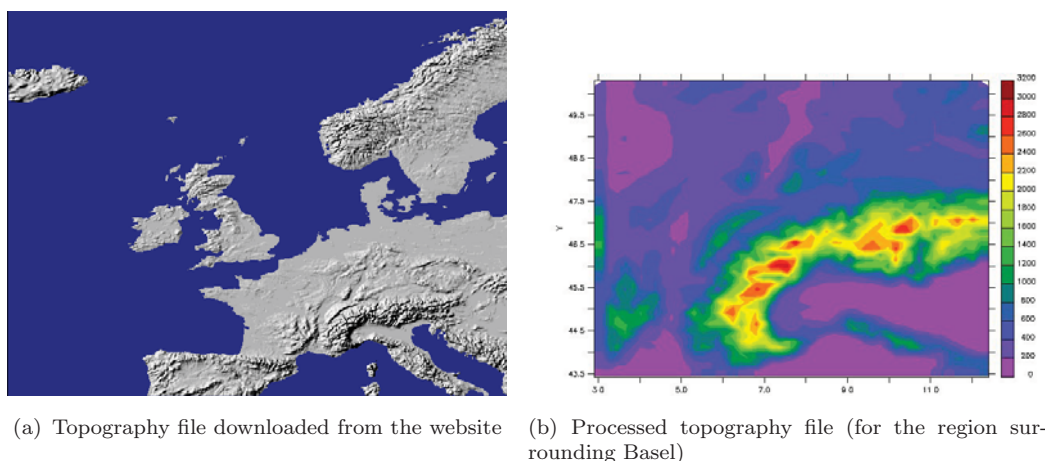
(a) Topography file downloaded from the website

(b) Processed topography file (for the region surrounding Basel)

FIGURE 7.3: Interpolation of Topography

7.1.2 Data Acquisition

For conducting a realistic simulation input data like the topographical, landuse and urban geometry are required. Furthermore, to force the effects of the scales larger than the one that can be handled by the mesoscale model appropriate meteorological data are required as boundary conditions. These data are fortunately, available on the Internet to be used by the scientific community. However, before using them in the simulations these have to be processed. Below we explain briefly how and in what format the data is obtained and how it is processed into a usable form.

7.1.2.1 Topography

A mesoscale domain may range from a few kilometers to a few hundred of kilometers. Over such a large expanse chances are that the topography will vary significantly. It is well known that the topography of a region can significantly alter the air flow as well as the temperature of the region under investigation. Fortunately, such variations in the topography can be taken into account in our mesoscale model. The topographical information can be downloaded from the website [2]
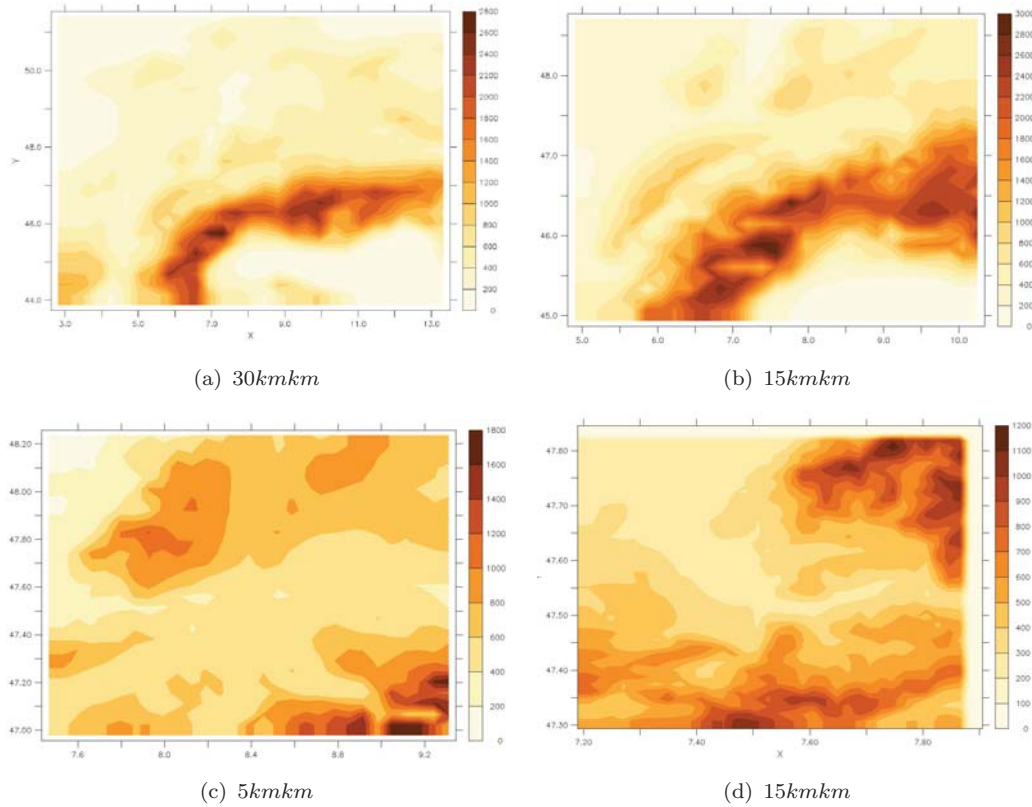
---

[2]http://edc.usgs.gov/products/elevation/gtopo30/gtopo30.html

(a) 30*kmkm*

(b) 15*kmkm*

(c) 5*kmkm*

(d) 15*kmkm*

FIGURE 7.4: Interpolated topographies

GTOPO30 it is a global digital elevation model (DEM) with a horizontal grid spacing of 30 arcs seconds (approximately $1km$). It is derived from several raster and vector sources of topographical information. For easier distribution GTOPO30 is divided into tiles which can be selected according to the need. This data is then processed to extract the topographical information of the region and domain we want to simulate. The raw data and the processed data is shown in Figure 7.3. Topographies of the four nesting domains are shown in Figure 7.4. To account for topographical non-uniformity, the mesh has been deformed. The deformation is maximum near the ground and decreases linearly to zero near the top of the domain. The mesh used for each of the four cases is presented in Figure 7.2

7.1.2.2 Landuse

A major aim of this project is to study the interaction between the climate of a region and the urban texture. It has been well established through various field

(a) Landuse tile downloaded from the website

(b) Processed landuse data for the area around Basel (legend represents fraction of urban area)
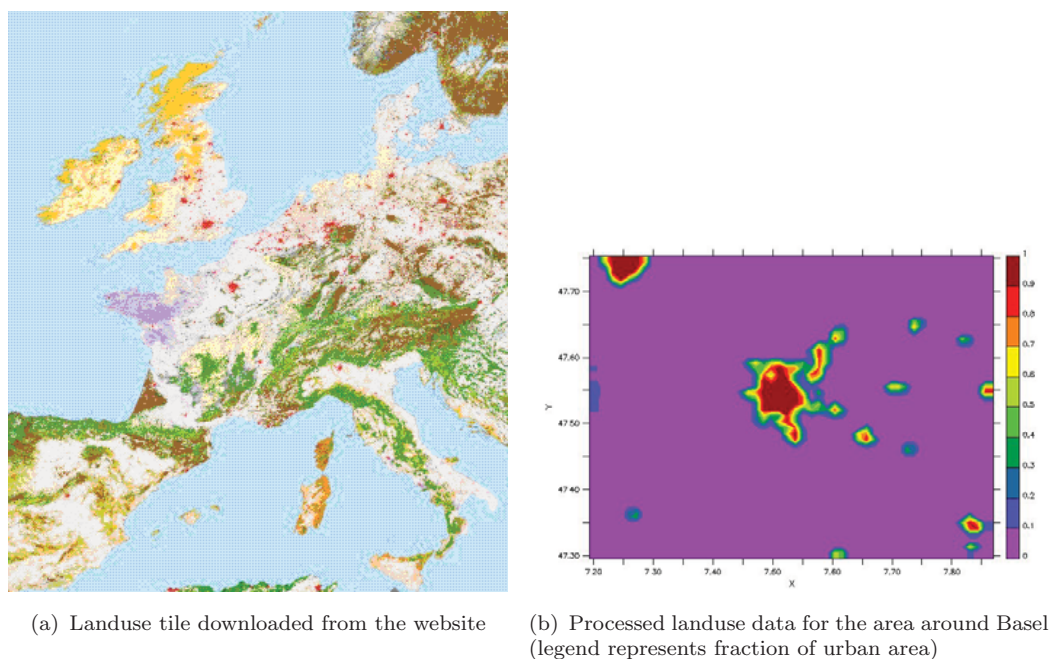
FIGURE 7.5: Interpolation of Landuse data

experiments and numerical simulations that an urban texture significantly affects the urban microclimate. The phenomenon of Urban Heat Island Effect is well explained in Chapter 1. Since, the mesoscale model that is developed is intended to address this phenomenon, relevant simulations are possible only when we input the correct landuse data into the model. This landuse data which comes in the form of a harmonized land-cover database over the whole globe is provided and maintained by the Global Vegetation Monitoring Unit [3] of the Joint Research Center, European Commission. From this data we extract the information about the percentage of artificial surfaces.

In Figure 7.5(a) one can see the graphical representation of the data obtained from the net. This has been processed into the required form for the simulation and presented in Figure 7.5(b). However, the data doesn't give any idea about the geometrical alignments of various urban elements. To sensitize the mesoscale simulations to the urban geometry, the concept of equivalent geometry (discussed in Chapter 6) is applied to extract the equivalent building and street width and

---

[3]http://www-tem.jrc.it/glc2000

street orientation. For the height, following the work of Roulet (2004) we assumed
the following:

- dense urbanized area: mean building height over 11m, building density
  higher than 50% (class 1)

- transition zone (suburban and industrial areas): mean building height be-
  tween 8 and 11m, building density 40 and 50% (class 2)

- villages cores and single houses: mean building height below 8m, building
  density lower than 40%

Very little information is available to us regarding the neighboring cities. We
have therefore, assumed that the neighboring cities have no influence on the local
climate of Basel. Thus the area surrounding the city of Basel is considered to be
100% rural.

7.1.2.3 Meteorological Data

The scales bigger than the domain or lying outside the domain can't be parametrized
or resolved. Their effects are captured in the mesoscale model using a procedure
called nesting via the boundary conditions. The effects of ocean and huge moun-
tains are taken into account by the Global model like NCEP (National Center for
Environmental predictions). The data (velocity, humidity, temperature, pressure)
from the global models are made available via a web portal [4] . The global model
generating these data has a horizontal resolution of $270km \times 270km$. The vertical
resolution is given in terms of 17 different pressure levels. The data on the Internet
is available every six hours ie. four times a day. To use these data to force the
mesoscale model having a much finer spatial and temporal resolution these raw
data are interpolated over space and time Roches (2007). Moreover, owing to a
large difference in the resolutions of a global and our mesoscale model with which

---

[4]http://www.cdc.noaa.gov/cdc/reanalysis/reanalysis.shtml
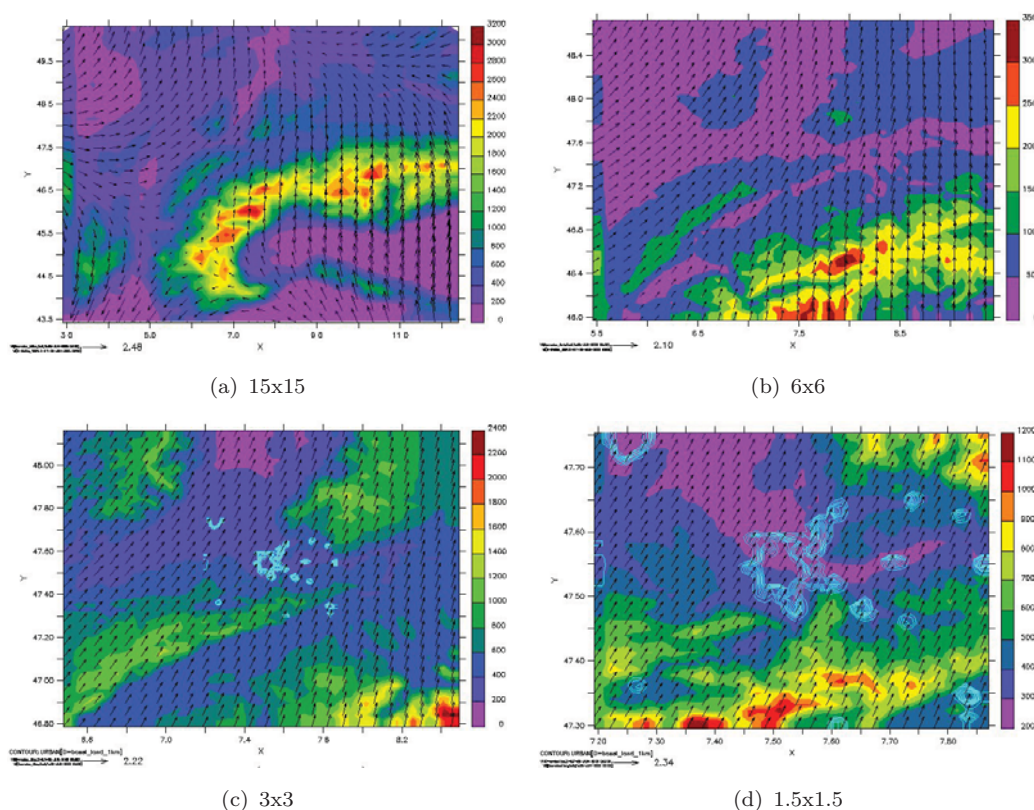
(a) 15x15

(b) 6x6

(c) 3x3

(d) 1.5x1.5

FIGURE 7.6: Stepwise interpolation of Meteorological Data

we intend to simulate a city and its surrounding, the boundary conditions that are obtained through interpolation are not of good quality hence, an approach of nesting different sized domains with progressively increasing resolution to go from global to mesoscale is used. After the interpolation the FVM solver is run to ensure mass, momentum and energy conservation. This not only improves the quality of the boundary conditions but also helps in accounting for the phenomenon that happens outside the domain of interest.

The whole concept of nesting and its importance is demonstrated for the case of Basel in Figure 7.6 The meteorological data downloaded from the Internet has a resolution of $270km \times 270km$. The velocities, temperature and humidity is to be interpolated to a grid having a resolution of $1km \times 1km$. For this we go in step we first construct a domain with a resolution of $30km \times 30km$ and assuming it to be 100% rural area we run a simulation to generate an output file. This output file is used to force another smaller domain with higher resolution. Thus we go in a

(a) $30km \times 30km$

(b) $30km \times 30km$

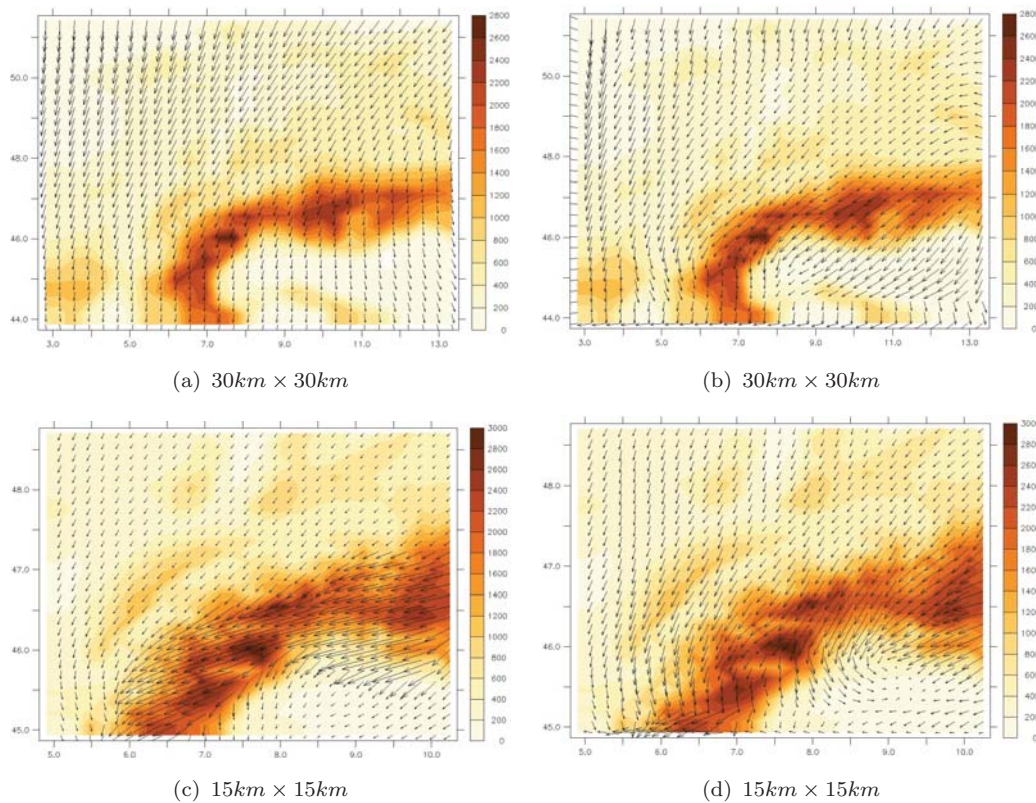(c) $15km \times 15km$

(d) $15km \times 15km$

FIGURE 7.7: Interpolated Meteorological Data

few steps from the Global model to the mesoscale model domain as shown in Figures 7.6. Meteorological data for forcing the $30km \times 30km$ domain comes from the global model (NCEP) (already explained in Chapter 2). Figure 7.7(a) presents the interpolated data from NCEP on the $30km \times 30km$ grid. Because of the large difference in spatial resolutions this simple interpolation doesn't guarantee mass and energy conservation. The velocities and temperature fields are therefore corrected using the FVM solver. The corrected velocity field is presented in Figure 7.7(b) in which richer topographically induced velocity variations are clearly evident. Indeed because of the comparatively finer resolution of this solution the bifurcation of the flow due to the mountain is visible at the right corner of the domain. After the computation of this new velocity, temperature, turbulent kinetic energy etc the output is interpolated to the next finer grid of $15km \times 15km$ resolution (Figure 7.7(c)). Once again the field is corrected and one can now see the vortices formed on the leeward side of the mountain (Figure 7.7(d)). The same is repeated at the resolution of $5km \times 5km$ and finally the output is used to force the domain of
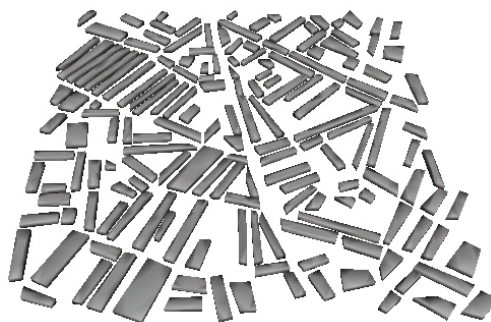
(a) Topography file downloaded from the website   (b) Processed topography file (for the region surrounding Basel)

FIGURE 7.8: 3D geometry

interest. It should be pointed out, that for simplicity, while correcting the fields it is assumed that the domain of simulation has no urban area (it is 100% rural area)

7.1.2.4 City Geometry

The 3-D model (Figure 7.8(b)) of the city is generated in NURBS (Non-Uniform Rational B-Spline) based 3-D modeling software Rhinoceros. The aerial view of the city is obtained from Google Earth (Figure 7.8(a)) and then the whole geometry is sketched manually in the mentioned software. The heights of the buildings are obtained from the results of field survey. The 3-D geometry thus sketched is then exported as a STL (Sterio Lithography) file which consists of a number of triangles forming closed volumes. This file is used to compute the radiation and fluid flow around buildings for finding the equivalent geometry to be used in the mesoscale model.

TABLE 7.1: Thermal properties of built material(thickness d(m), heat capacity $C_m(MJ/m^3K)$, thermal conductivity $\lambda(W/mK)$)

Roof Layer	1	2	3	4
d	0.02	0.02	0.02	0.04
C	0.128	0.276	0.382	1.745
λ	0.14	0.129	0.090	0.984
Street Layer	1	2	3	4
d	0.010	0.040	0.025	0.975
C	1.940	1.940	1.550	1.350
λ	0.750	0.750	0.934	0.275
Wall Layer	1	2	3	4
d	0.01	0.03	0.08	0.02
C	1.778	1.780	1.764	1.779
λ	1.070	1.076	1.071	0.651

7.1.3 Thermophysical Properties of the built environment

The physical characteristics of the building materials are established using data from the BUBBLE measuring campaign (Rotach et al. (2005)). The thermal characteristics of building materials (presented in Table 7.1) considered in this work are taken from the data collected at the Sperrstrasse station. More details concerning the characteristics of urban surfaces can be found in Christen (2005), Salamanca and Martilli (2008).

7.2 Results

7.2.1 Urban vs Rural

With the set-up described above, two simulations were conducted one without any urban parameterization and another with urban parameterization, using equivalent geometry representation. The results are shown in Figures 7.9 and 7.10 at 4 hourly intervals. The contours in the figures represent the air temperature $10m$ above the ground, whilst the arrows represent the velocity field at the same height. From these figures we observe the following:

(a) 09:00 Rural

(b) 09:00 Urban

(c) 13:00 Rural

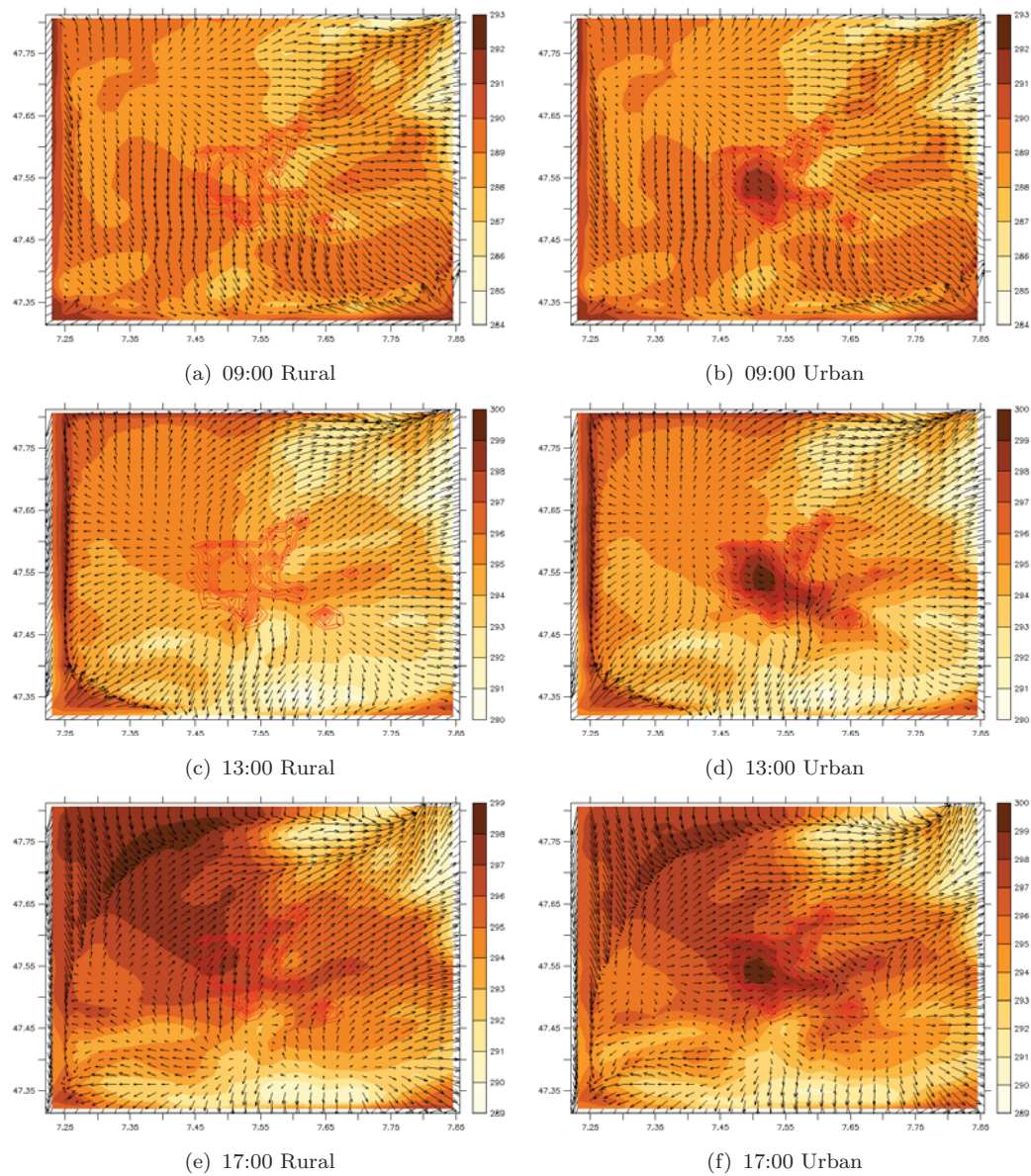(d) 13:00 Urban

(e) 17:00 Rural

(f) 17:00 Urban

FIGURE 7.9: Rural vs Urban (25th June 2002)

- The city core is always hotter than its rural surrounding, a fact that was observed in the field experiment cited in Chapter 1.

- The temperature increases as one moves towards the city core.

- The eye of the Urban Heat Island is shifted in the direction of the wind.

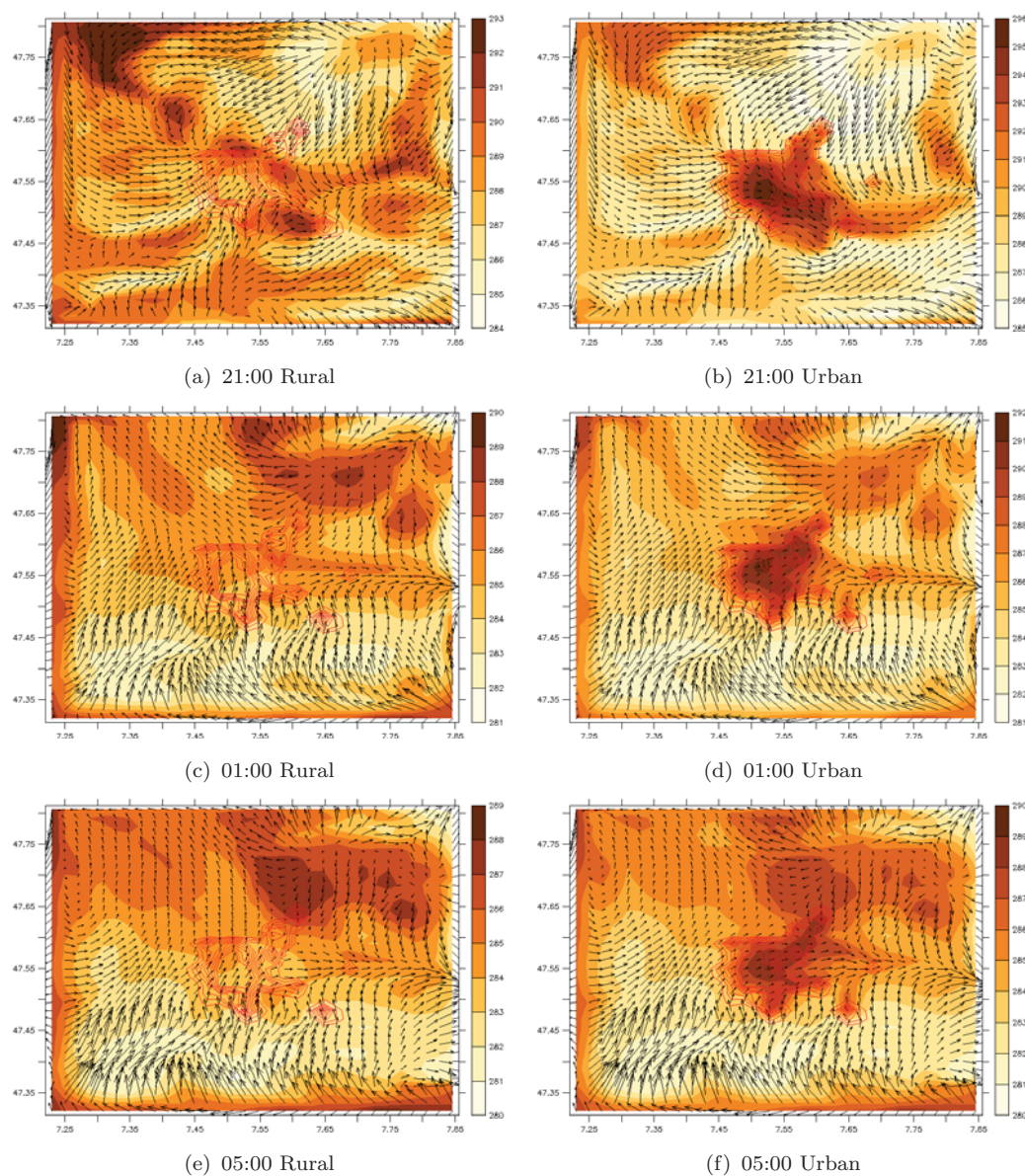- There is an entrainment of cold air toward the hot core of the city.

(a) 21:00 Rural

(b) 21:00 Urban

(c) 01:00 Rural

(d) 01:00 Urban

(e) 05:00 Rural

(f) 05:00 Urban

FIGURE 7.10: Rural vs Urban (25th-26th June 2002)

7.2.1.1 Comparison with measured data

Since, the measurement from a single measuring site could be erroneous, the data collected from different weather stations (corresponding stations considered for averaging are emphasized in the Appendix B) are averaged (Muller (2007)) and then used for comparison. Likewise, the simulation data are also averaged over several nodes. In Figure 7.11 a comparison between the simulated and measured urban

temperature is presented. It is clear from this figure that the trend of the temperature profile over the three days is well predicted, but that the absolute value of the temperature is over-predicted, especially around mid-day. This is quite expected too because in the modeling we have completely ignored the cooling effects caused by evapotranspiration and obstruction of radiation due to the presence of cloud the later being more pronounced on the third day. Accumulation of numerical errors over such a long duration can be another reason for the diverging profile.

In, Figure 7.12 we compare the measured and simulated UHI intensity. From this it is apparent that in both cases, the maximum UHI intensity is observed at night as expected. This is due to the fact that the built surfaces have high specific heat capacity and hence stores huge amount of heat which is restituted back to the surface layer at night making it hotter. Also at night the turbulence is significantly reduced due to the absence of any surface heating due to radiation and hence the heat transfer by convection is also greatly reduced resulting in hotter city core. It also appears that the measured UHI intensity profile is smoother than the simulated profile. The simulated UHI also predicts a short lived negative UHI which was not observed in the measurement. However, such negative UHI is not uncommon. Finally, the time average value of the UHI predicted by the model (2.179) is very close to the measured value of $2.5C$.

The mismatch between the measured and simulated result can be attributed to several reasons enumerated below:

1. Neglection of the evapotranspiration effects in the models that could have a cooling influence and could have reduced the temperature during the day

2. Uncertainties involved with the modeling of turbulence

3. Uncertainties involved with the input data (particularly material thermo-physical properties)

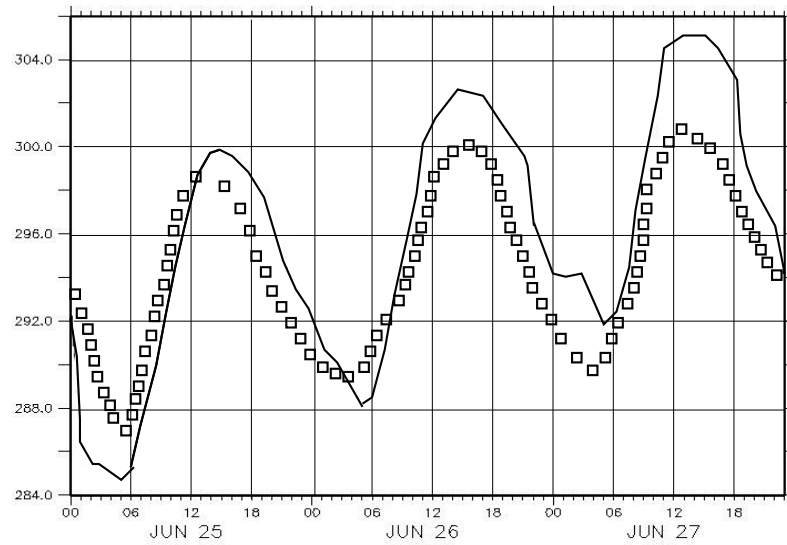4. Numerical errors arising due to discretization

FIGURE 7.11: Comparison of predicted and measured temperature profiles: The solid line relates to simulated results and the squares to measured data
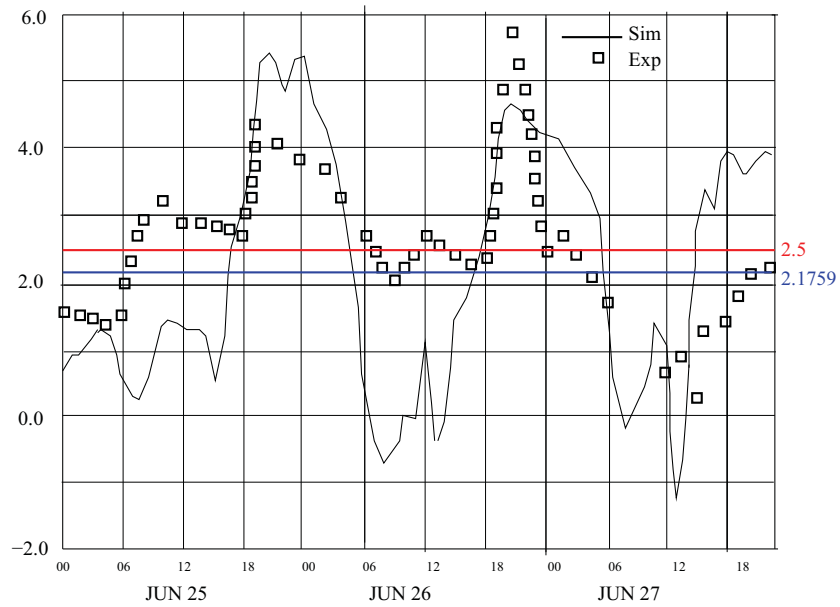

FIGURE 7.12: Urban Heat Island Intensity

5. Neglection of various phenomenon occurring in the atmosphere like green house effect, precipitation and cloud formation.

However, it would be harsh to conclude that the mismatch is solely because of the error in numerical modeling. The mismatch can as well be attributed to to the uncertainty and error involved in experimentation itself. Nevertheless, this comparison does give us cause for confidence that the physical basis of the new multiscale modelling approach is reasonable.

7.2.2 Sensitivity to boundary conditions

To run the model we needed the meteorological data. Since, it is computationally expensive to run an hourly simulation for the whole year, there is a need to statistically reduce the number of simulations. The question then arises is that how many simulations are sufficient enough to deduce something concrete and what factors wind speed, wind magnitude or topography might impact UHI the most. Although, this is outside the scope of the present work, here we made an attempt to see the effect of the boundary condition on the UHI Intensity. Two simulations were conducted one with a wind speed of $3km/hour$ from west to east and the other with the same speed but from north to south. In the Figure 7.13 we present the difference of temperature in the two cases. It is clear from the figure that the boundary conditions are not much affecting the temperature contours inside the city. This observation can be attributed to the fact that air flow near the vicinity of Basel is very much dictated by the topography of the region. One can see in Figure 7.14 that the difference in wind speed between the two cases are more pronounced near the boundaries but inside the city the difference is negligible. This observation is a little intuitive too. For example in a region with highly non-uniform terrain the eddy formation will be more governed by the topography and less by the boundary condition. Valleys, for example will be characterized by large eddies irrespective of the flow direction at the top of the mountain. In the case we simulated this appears to be true. Thus when we know that the flow in a
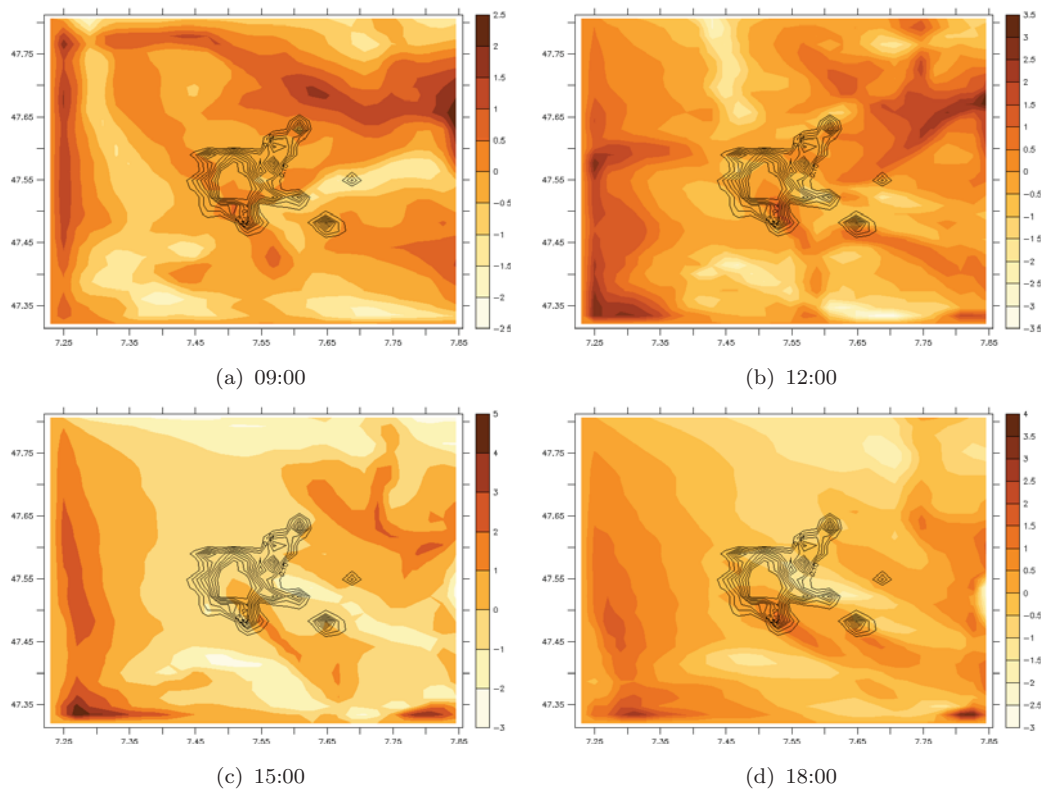
(a) 09:00

(b) 12:00

(c) 15:00

(d) 18:00

FIGURE 7.13: Effect of boundary condition on ambient temperature (East-West)-(North-South)

city is driven more by the topography then probably, the number of simulations to generate an yearly data set can be decreased significantly. However, more simulations on cities with relatively flat topography is required to design methodologies for statistical reduction.

7.2.3 Effects of UHI mitigation strategies on cooling energy demands

In this section we attempt to determine the consequence of UHI for buildings energy demands for space conditioning and also to examine ways in which this might be modified by altering the properties of our urban fabric. The purpose of these hypothetical tests is to understand the potential for urban planning interventions to modify the urban climate.
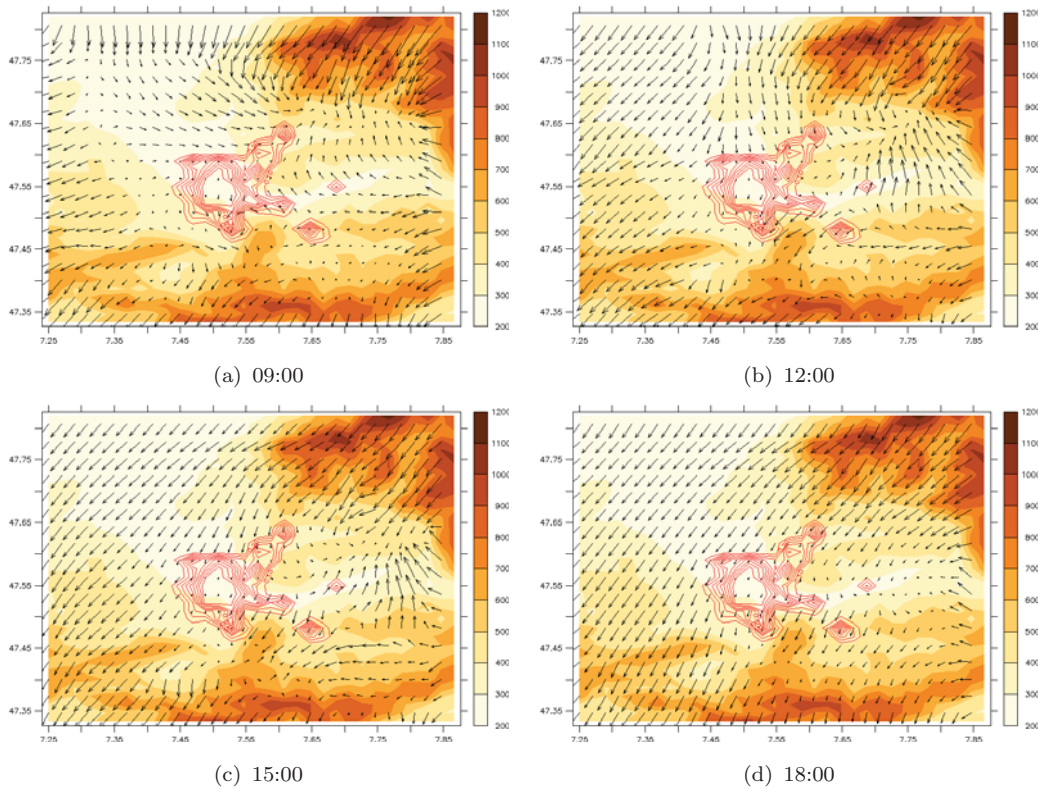
(a) 09:00

(b) 12:00

(c) 15:00

(d) 18:00

FIGURE 7.14: Effect of boundary condition on wind in the city (East-West)-
(North-South) (colours show topography in m)

Energy consumption for the cooling of buildings may be determined by the simpli-
fied expression $Q_c = 24C_o.DD_c.10^{-3}/\eta_b$ (kWh), where C_o is the total building con-
ductance (WK^{-1}). DD_c are the cooling degree days ($DD_c = \sum_{i=1}^{24}(T_i - T_{base}/24)$,
η_b is the boiler efficiency and T_{base} is the base temperature above which cooling
is required: assumed to be $291K$ in these simulations. Since the ratio of energy
consumption for cooling is linearly proportional to the corresponding degree days,
the normalized DD_c gives and indication of the relative increase in the energy
demand for cooling purpose between two different scenarios (eg. with and with-
out urban parameterization). Using the definition of DD_c we present in Figure
7.15 the DD_c of the urban area normalized by that of the rural area. It is clear
from this figure that urbanization can lead to about a 40% increase in the energy
demand for cooling purposes.
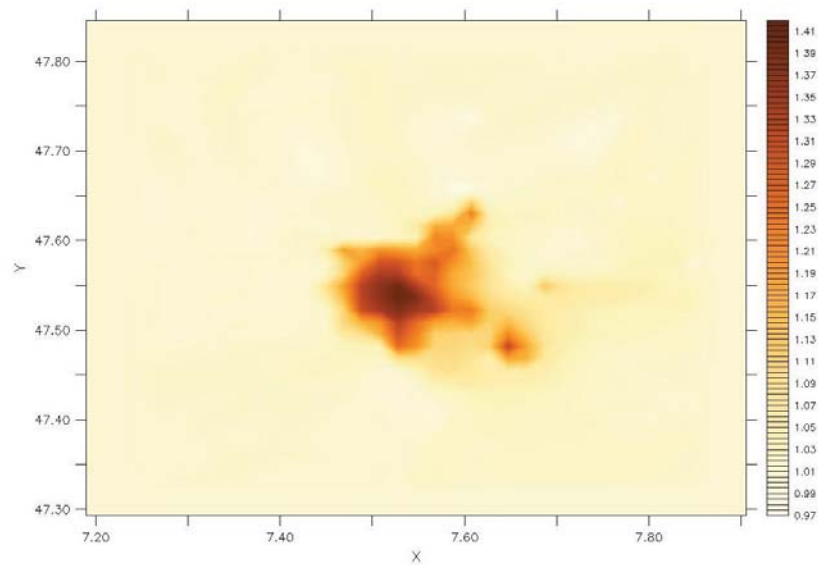
FIGURE 7.15: DD_{curban}/DD_{crural}

7.2.3.1 Effects of changing the Conductivity of the built material

The simulation of our base case (with urban parameterization) was then rerun with the conductivity being reduced, to reduce the rate of heat transfer across the (better insulated) envelope and alter its outside surface temperature. In this case a lower wall temperature results in less energy being transferred to the surroundings, resulting in lower ambient temperatures. Figure 7.16 shows the corresponding effect on the DD_c. From the figure it is apparent that a 25% variation in the value of thermal conductivity of the walls resulted in an offset of cooling energy demand by upto 10%.
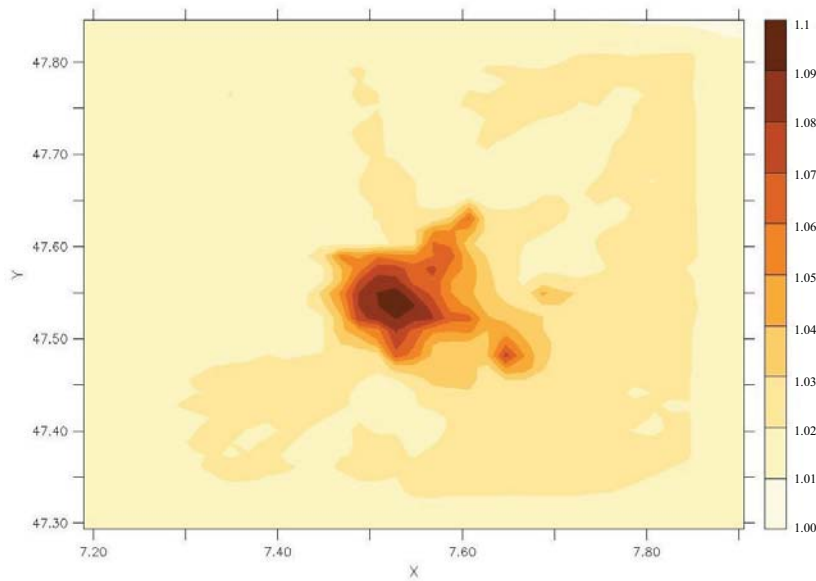
FIGURE 7.16: Effects of changing the conductivits of built material on CDD

7.2.3.2 Effects of changing the Specific Heat Capacity of the built material

Three further simulations were conducted with different values of specific heat capacity (0.894 (low), 1.788 (base) and 5.364 (high) $[MJ/m^3K]$) of the walls to study its effect on city temperature. The results are plotted in Figure 7.17, in which one can see that increasing the heat capacity of the built material tends to decrease the diurnal variation of temperature and positively shifts the phase of the profile. This is because during the day buildings with high specific heat capacity will absorb more heat and hence less heat is available for heating the air resulting in a lower temperature during the day; the converse being the case at night so that the night time temperature is increased. Figure 7.18 shows the effet of change in specific heat capacity on the cooling degree days. It appears that a 200% increase in the specific heat capacity of the walls results in up to 27% increase in the cooling energy demand.
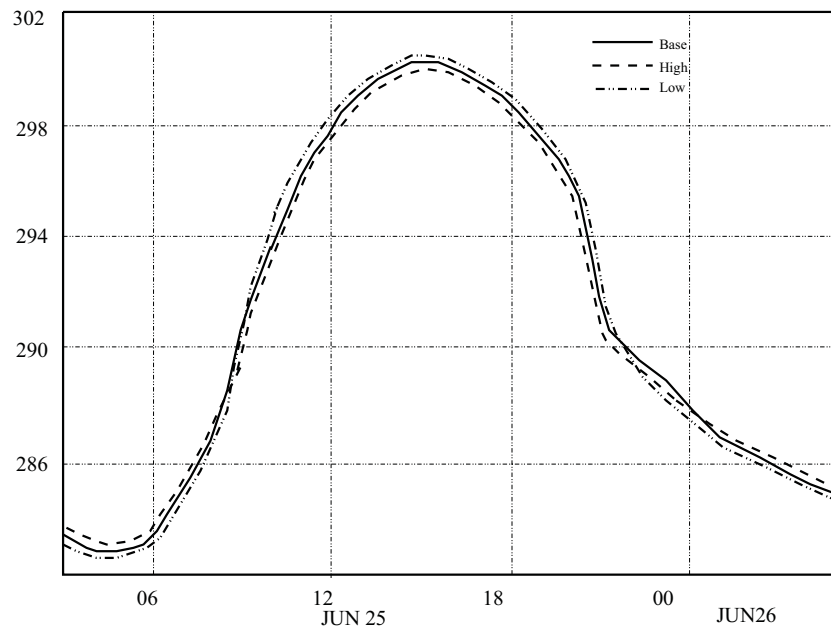
FIGURE 7.17: Effects of changing the specific heat capacity of the built material
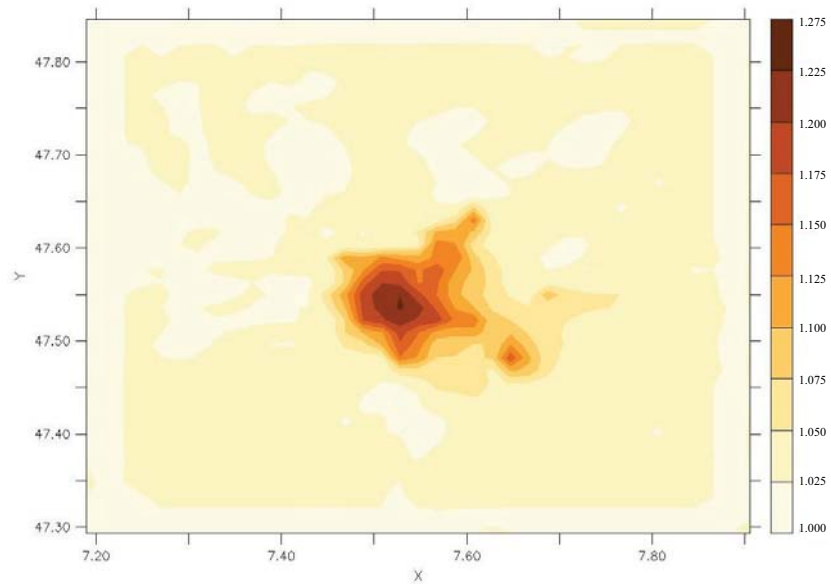

FIGURE 7.18: Effects of changing the specific heat capacity of built material on CDD
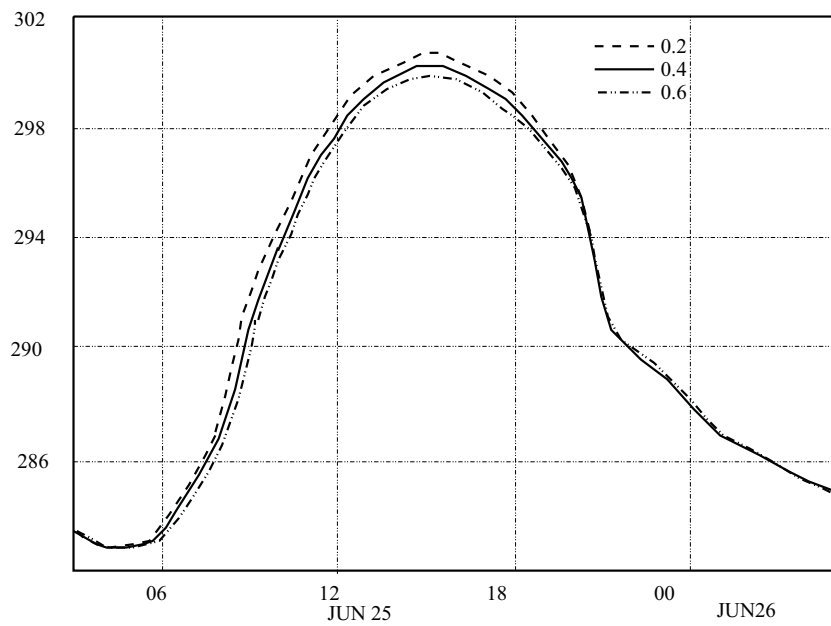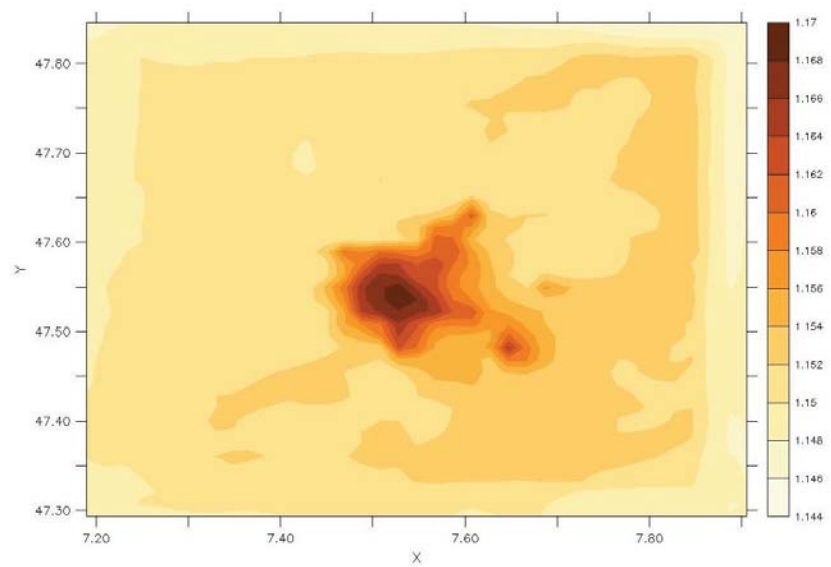
FIGURE 7.19: Effects of changing the albedo of the built material

FIGURE 7.20: Effects of changing the albedo of the built material on DD_c

7.2.3.3 Effects of changing building surfaces albedo

Albedo is the fraction of solar energy (shortwave radiation) reflected from a surface back into space. Since the shortwave radiation is present only during the day its effect is also confined to the day time. This can be seen in Figure 7.19. According to Equation 5.17 a lower value of albedo results in a higher surface temperature and hence more heat being transferred to the air, resulting in a higher temperature. It is for this reason that the temperature in the city in Figure 7.19 decreases with increased albedo. Figure 7.20 also shows the impact of albedo on cooling degree days. In particular this presents the DD_c of a city with albedo equal to 0.2 divided by the DD_c of the same city with albedo equal to 0.6. The result shows that difference of 0.4 in albedo offsets the cooling energy demand by as much as 17%.

7.3 Conclusion

In this chapter a range of scenarios have been simulated to better understand the magnitude of the UHI effects, its impact on buildings' space conditioning demands and ways in which this impact can be mitigated by modifying certain characteristics of the urban fabric. In the case of Basel we have shown that due to the various heat transfer mechanisms discussed earlier in this thesis the city induces an average warming of as much as 5^oC which can lead to a 40% increase in cooling energy demand. Most of the important characteristics of UHI (hotter city core, entrainment of air towards the city center, more pronounced UHI during the night, eye of UHI shifted along the direction of the wind) are well reproduced by the model. In a city like Basel where the flow is very much influenced by the topography, the wind directions at the boundary of the domain seems to have minimal influence on the UHI intensity. From the comparisons of the results with with the field measurement data, it was observed that the UHI intensity as well a the urban temperature was somewhat overestimated and hence that there is a need

to include the effects of vegetation and evapotranspiration in the model for more accurate predictions. The effect of changing the thermophysical properties on the buildings cooling energy demand was studied and it was concluded that it can be significantly altered by changing the values of specific heat capacity, thermal conductivity and surface albedo.

Chapter 8

Conclusion

8.1 Highlights of the research work

- A new Multiscale Modelling approach has been developed to simulate urban climate. In this results from Global Model are used to force appropriate regional boundary conditions onto a Mesoscale Model. Subgrid scales in these models are simulated using a newly developed Urban Canopy Model coupled with a simple Building Energy Model. The model accounts for the topography, landuse data and is also sensitized to the complexity in urban geometry via the concept of equivalent geometry. Thus the MM-UCM-BEM coupled model can properly account for the macro and meso scales while solving for a city's local climate at a horizontal resolution of $1km$ approximately.

- In order to understand the flow over bluff bodies (cuboidal structures) generally encountered in a city, Large Eddy Simulation was conducted over an array of cubes. A careful analysis of the data led to a better understanding of the flow. The result showed that the dispersive fluxes which result from spatial averaging are as important as the turbulent fluxes. The strange behaviour of these fluxes was observed to be related to eddy formation between cubes.

- Following from the above conclusions a new Urban Canopy Model was developed in which the principle energy and momentum exchanges between ambient air and built surfaces are parameterized as functions of simplified urban geometry. With a coherent physical basis, this new validated UCM accurately models the vertical velocity profile within the urban canopy. This model is integrated with a mesoscale atmospheric flow model to facilitate accurate mesoscale predictions of the urban climate.

- One of the problems associated with the use of Urban Canopy Models is the considerable simplification that is required in the representation of urban geometry. No sound basis existed for the choice of such simplifications. To resolve this issue the concept of "Equivalent geometry" has been introduced. The concept is the first of its kind and provides a sound basis for the choice of a simplified representation of a complex city. The new approach also reduces the need for time consuming field surveys. Further efficiency improvements can in principle be made by using laser scanned data of building geometry.

- For extracting the equivalent geometry two new tools are introduced which were not previously used within the field of atmospheric modelling. The Simplified Radiosity Algorithm and Immersed Surface Technique have been first tested for their accuracy against numerical / experimental data and then used extensively for extracting equivalent geometries for mesoscale simulations. The Immersed Surface Technique coupled with a Simplified Radiosity Algorithm can be used as a microscale model for simulating flow around a group of buildings for evaluating wind and thermal comfort.

- One of the main problems associated with atmospheric prediction tools is the difficulty in their usage. Since one of the main aims of this work was to bring the atmospheric modelling and building physics communities closer together, a GUI was developed to make the task of simulating the Urban Climate simpler. With this simple GUI the setup time for mesoscale simulations is reduced significantly. A small tutorial is discussed in Appendix A

Our practical conclusions relate to applications of the urban climate model to the city of Basel. From this we conclude that:

- The physical phenomena responsible for the urban heat island (UHI) of Basel have a combined intensity of some 5-6 C.

- This UHI intensity can be adjusted by: $0.5C$ to $2C$ with plausible adjustments to the thermophysical properties of building materials and by $0.5C$ by modifying the reflectance of building envelopes.

It should be noted however, that these simple scenarios have been conducted more to demonstrate the potential of the new multiscale urban climate model. Further work is required to produce detailed systematic guidance for urban climate planning.

8.2 Future work

- Introduction of the humidity equation as well as means of representing anthropogenic heat sources within FVM (and a model for evapo-transpiration) or the usage of well established models like WRF which can also simulate precipitation.

- The new concept of "Equivalent Geometry" is quite promising as it is perhaps the only way to sensitize a mesoscale model to the complexity in real urban geometry. At the moment this is done by running several simulations manually. However, several stages in this procedure could be automated by using optimization techniques and by automating the generation of solid geometries in STL file format.

- At the moment the simulation can't be run for more than 3-4 days due to the accumulation of numerical errors. However, to use the tool as a preprocessor for generating climate files for building simulation tool, simulations for considerably longer time periods will be necessary. City planners might also be

interested in studying the performance of that city throughout the year, depending upon meteorological data. This also calls for long term simulations. One pragmatic solution is through statistical reduction: Simulating the city in question for a set of most probable wind direction and magnitudes and sun positions and then reconstructing hourly time-series results.

- With the increasing availability of the 3-D laser scanned city geometry, height information will also be more accurate; thus the equivalent representation of actual city geometry can be further improved. By doing so the uncertainty arising from the geometrical representations can be minimized significantly.

- At the moment the power consumption in the buildings in a city is not accounted for in the model because of the uncertainties involved with their estimation. However, with the Google Power meter [1] coming in to public domain it will be fairly easy to make this estimation and then modify the sources of the energy equation to account for this.

- One of the biggest difficulties in the development of the Multiscale Model was the dearth of experimental data for validation. To develop a strong faith in such tools their performance needs to evaluated against controlled experiments (conducted inside wind tunnels) as well as field experiments. The later should involve measurements (of wind, temperature and humidity) at fine spatial and temporal resolution for an appropriate spatial grid throughout the entire city. This should ideally also be backed up by simultaneous energy consumption measurements due to both buildings and transport.

- In our Multiscale Modeling approach various models are unidirectionally coupled to each other via the boundary conditions. Because of this unidirectional coupling there is no feedback-mechanism. To further improve this modeling approach it is important to do some sensitivity test to study the importance of such feedbacks. This again calls for nestings at different levels

---

[1]http://www.google.org/powermeter/

where all the models run simultaneously. However, such features are already supported by Atmospheric models like WRF.

Appendix A

MesoSim Graphical User Interface: Tutorial

To launch the MesoSim tool just launch the program from the command line using the command 'mesosim'.

To start a new simulation click on the button "New Simulation". The New Simulation Wizard (Figure A.2) should appear on the screen. If you wish to work with an existing parameter file then check the "Use existing parameter file" checkbox and choose the required parameter file. Alternatively, a new project can be created by choosing a project name and the destination directory. Click "Next" after making an appropriate choice.

The mesh input dialogue (Figure A.3) then appears. Enter the number of nodes and the cell dimensions in the three directions with Z pointing in the vertical direction. To choose a uniform grid size check the appropriate checkbox and enter the corresponding cell dimension. Click on "Next"

A sheet to enter the cell dimension (Figure A.4) is provided, if in the last step a non-uniform resolution was chosen for any direction. Enter the required dimension. Generally in the vertical direction (Z direction) the resolution should be finer near the ground and coarser as one recedes away from the ground. Click on "Next".

The Boundary Condition dialogue box (Figure A.5) now appears. Enter the types of boundary conditions experienced at the six faces of the domain. A "Column" boundary condition implies external forcing using data from a global model and a "Wall" boundary condition corresponds to a slip boundary condition. Also enter the longitude and latitude of the bottom left corner of the domain. Click on "Next".

Now the Topography dialogue box (Figure A.6) appears. Enter the path where the topographical data downloaded from the internet is stored. Choose the data format (GTOPO30 in this case). Choose the latitude and longitude shift. Enter the value of the Interpolation factor. Also enter the name of the output file. Click on "Next".

Now into the Landuse dialogue box (Figure A.7) appears. Enter the path of the directory where the landuse data downloaded from the internet is stored. Enter the format of the landuse data (GLC2000) in this case. Also enter the name of the output interpolated landuse files. Click on "Next"

Now complete the Forcing dialogue box (Figure A.8). For this enter the path of the meteorological data downloaded from the internet. Also enter the name of the output interpolated forcing file. Click on "Next".

The Calculation Control Parameters dialogue box then appears (Figure A.9). Choose the start date and time of the simulation and the duration of simulation. Also choose the frequency of output files and time steps for various phenomena. Click on "Next".

Now the initialization dialogue box appears (Figure A.10). Choose the values to initialize wind speed and temperature. Click on "Next".

Finally, the solver parameters dialogue box A.11 appears. Select all the checkboxes and choose the directory for the Result file. Click on "Finish"

Click on the "Topography" button. An "Interpolating Topography" dialogue box (Figure A.12) with a status bar appears. Click "Abort" to kill the interpolation process or click close when the interpolation successfully finishes.

Click on the "Landuse" button. An "Interpolating Landuse" dialogue box (Figure A.13) with a status bar appears. Click "Abort" to kill the interpolation process or click close when the interpolation successfully finishes.

Click on the "Forcing" button. An "Interpolating Topography" dialogue box (Figure A.14) with a status bar appears. Click "Abort" to kill the interpolation process or click close when the interpolation successfully finishes.

To visualize the mesh go to File > Load Mesh File. Choose the required *.grda file. The mesh view along with the topography (Figure A.15) will appear. Zoom and rotate the view to inspect the mesh. Once satisfied click on the "Solver" button. Simulation will start.

To visulize the progress load the file *.res "File > Load Simulation result file". A visualization tool kit (Figure A.16) will appear. Choose the plane (xy, yz or zx) and the variable of interest (U,V,W,T,...) to show the contours (Figure A.16). Also check mark vector if you wish to superimpose the vector plot on the contours (Figure A.17).

All the results are also written to a netcdf file which can be visualized using Ferret, an open source software.
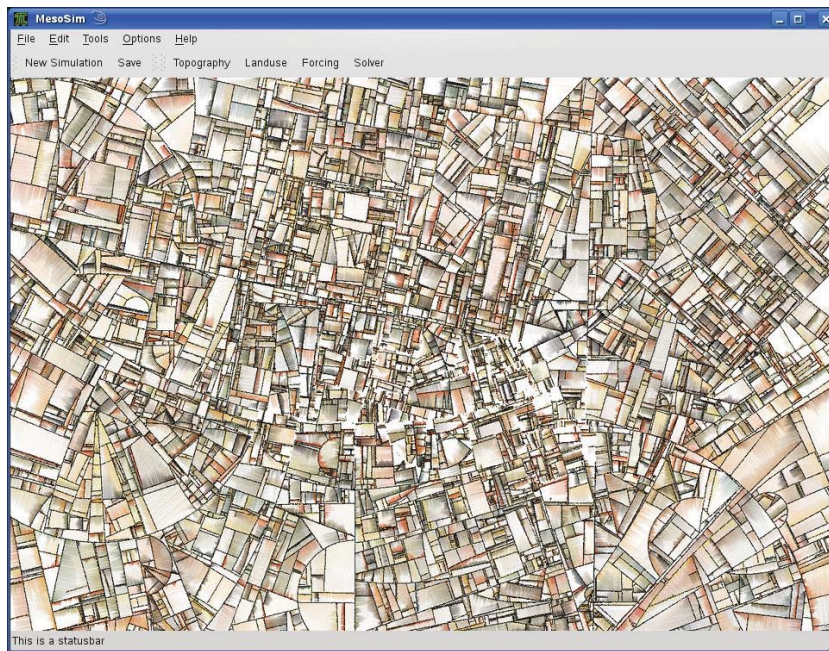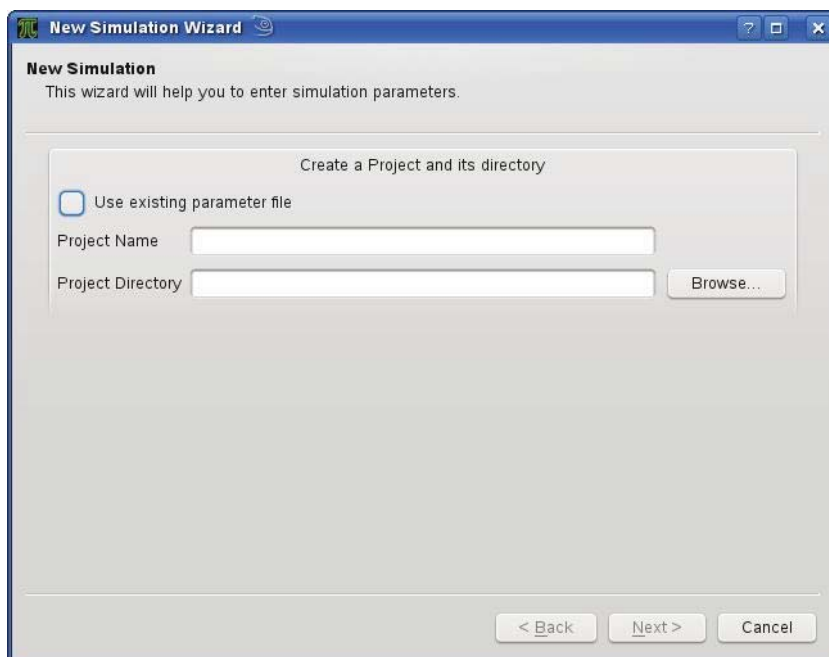
FIGURE A.1: MesoSim starting window

FIGURE A.2: New Simulation

FIGURE A.3: Nodes and uniform resolutions input dialogue box

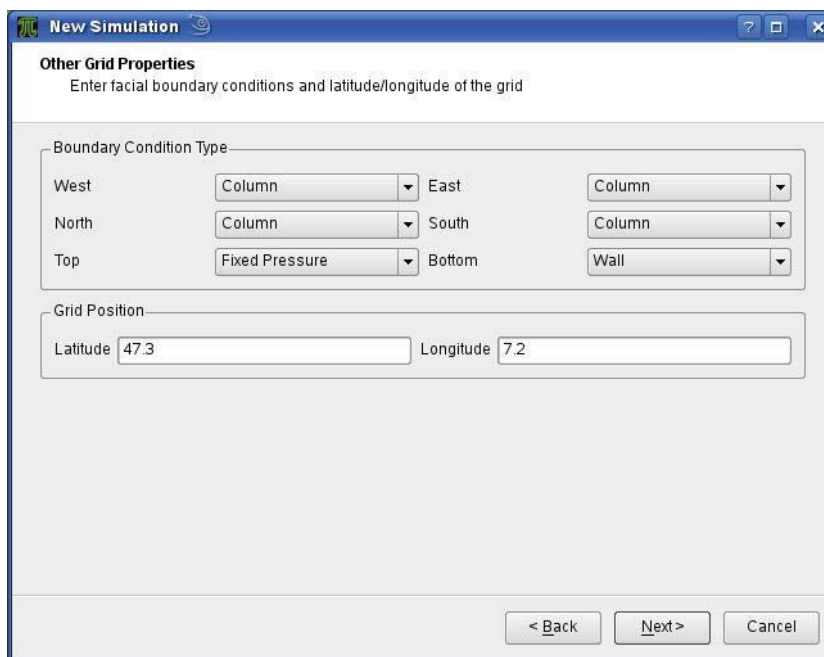FIGURE A.4: Non-uniform resolutions input dialogue box
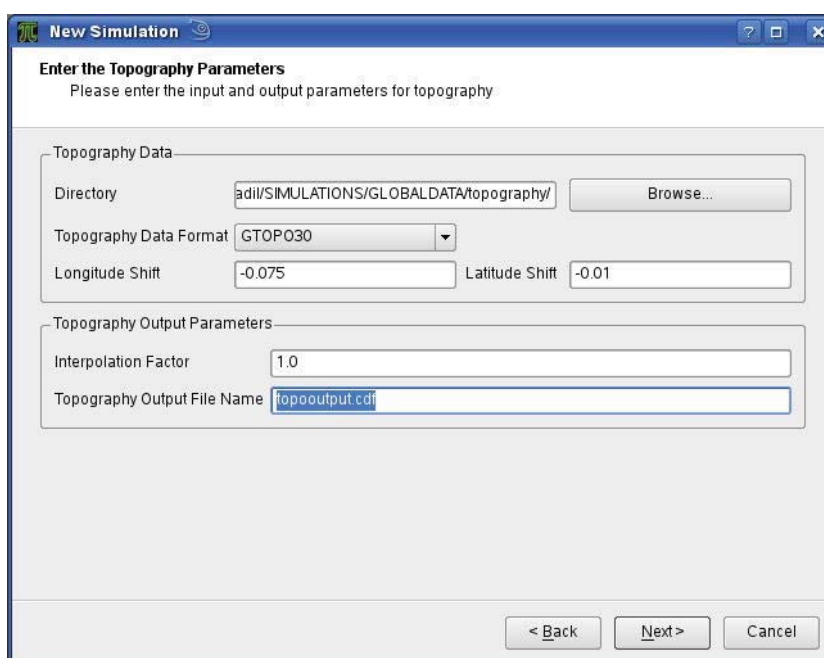
FIGURE A.5: Boundary Condition dialogue box

FIGURE A.6: Topography Setting dialogue box
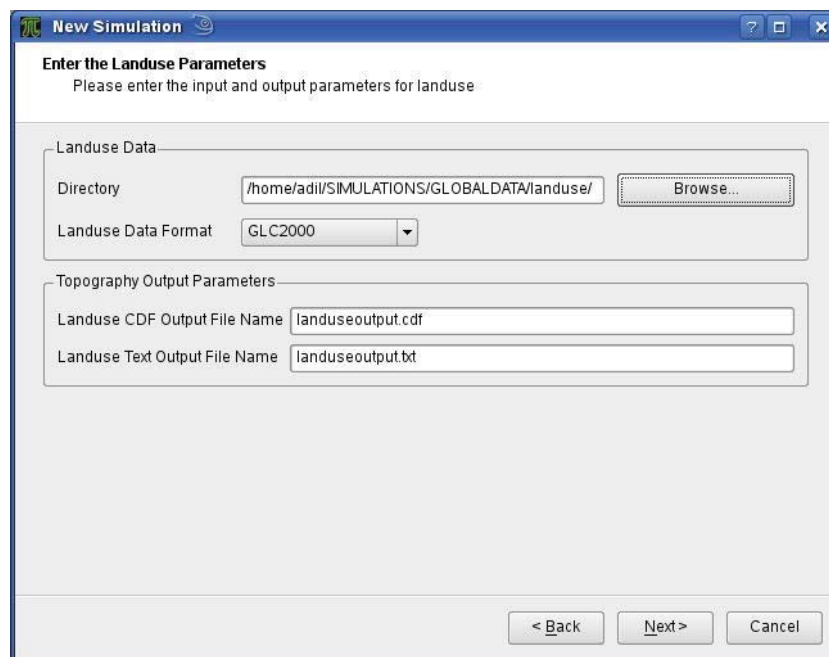
FIGURE A.7: Landuse Setting Dialogue Box
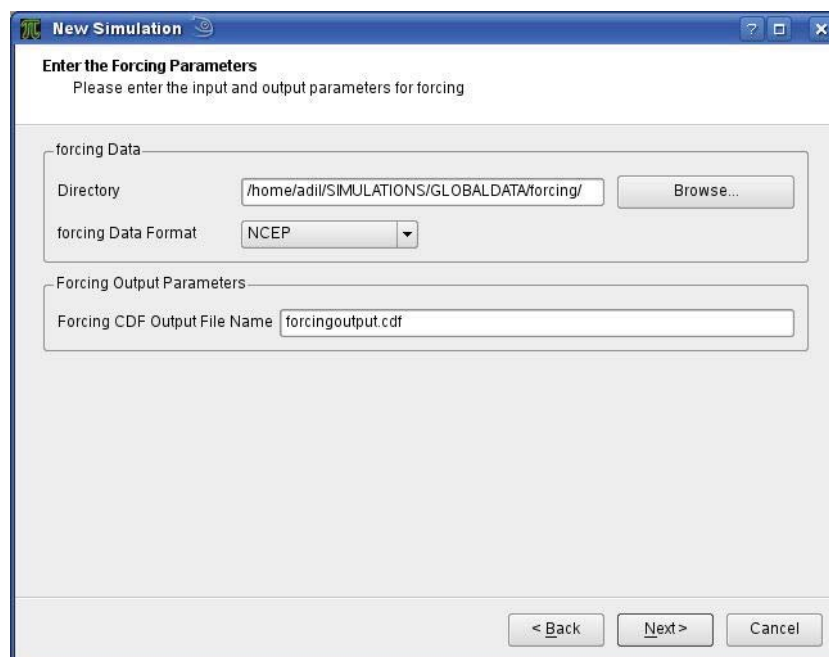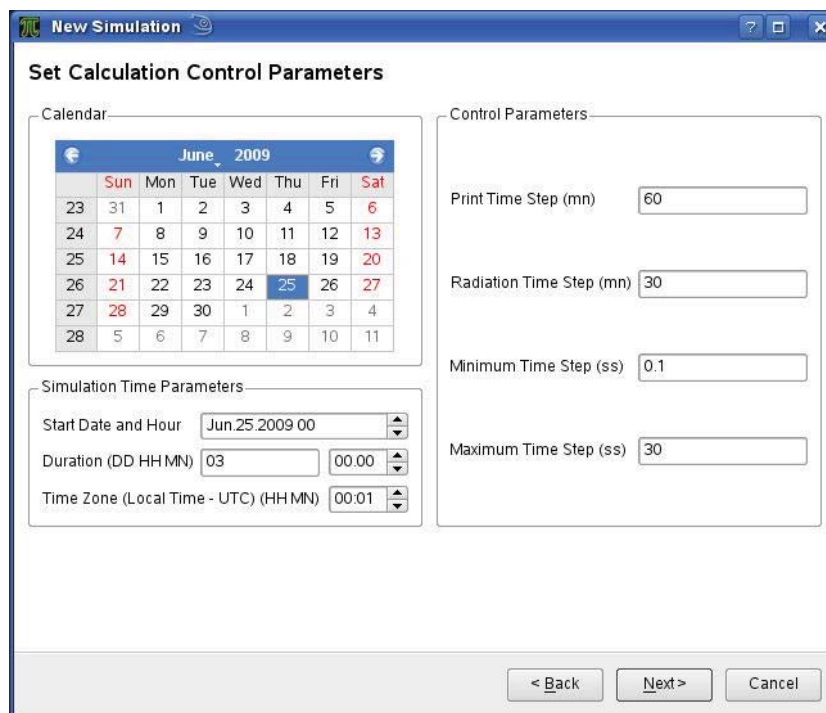
FIGURE A.8: Meteorological Setting Dialogue Box
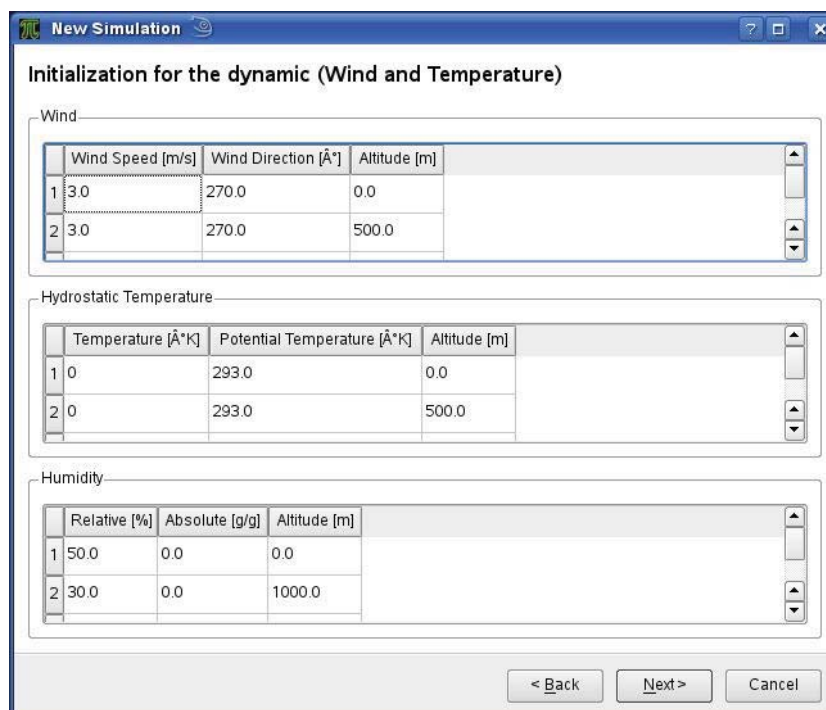
FIGURE A.9: Date and duration of simulation Dialogue Box

FIGURE A.10: Initialization or Sensitivity test dialogue box
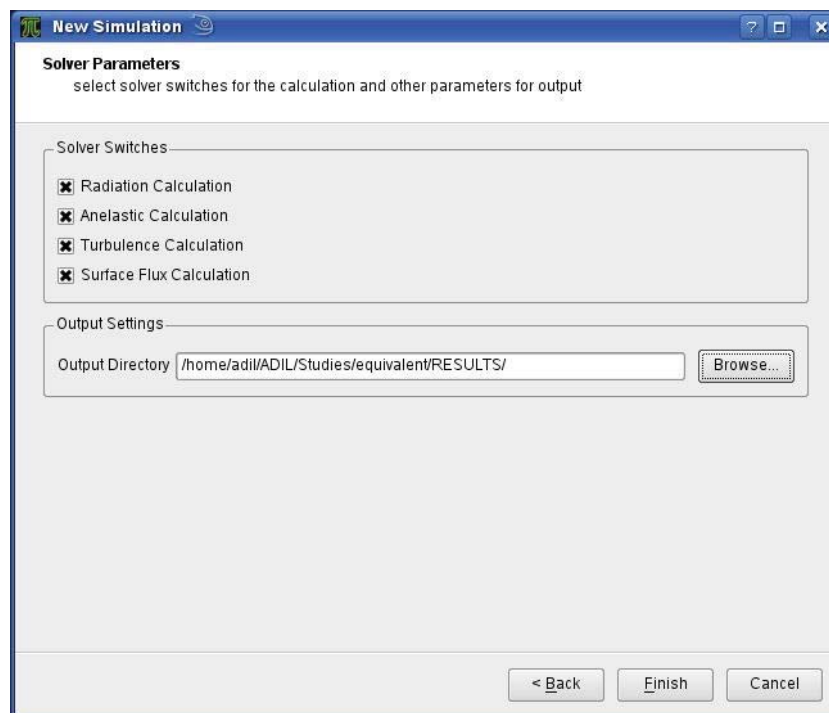
FIGURE A.11: Switches dialogue box
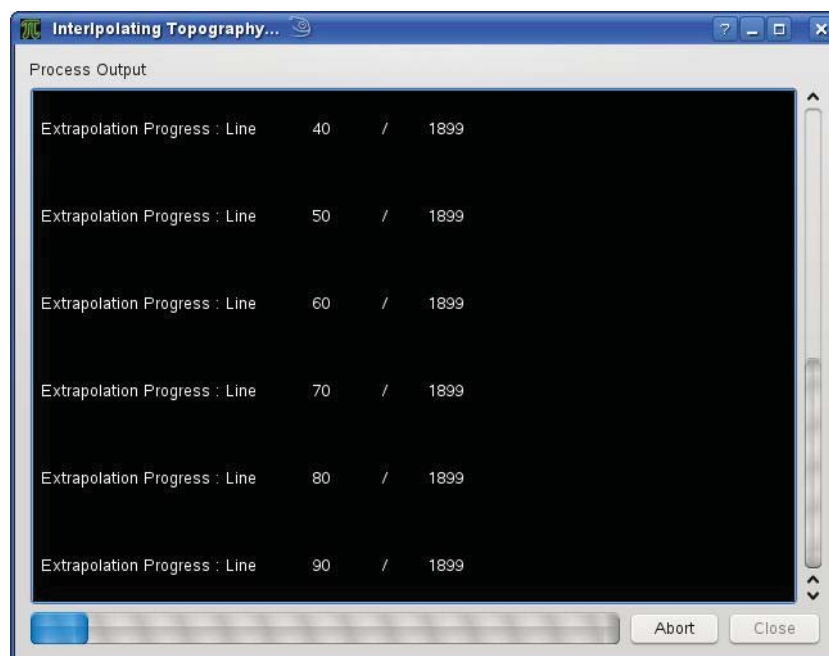
FIGURE A.12: Topography interpolation in progress
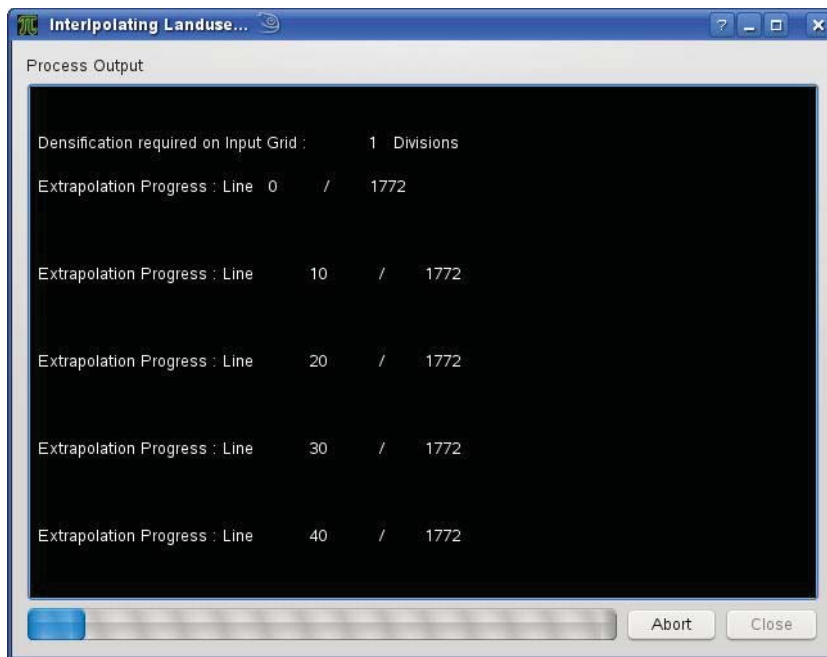
FIGURE A.13: Landuse interpolation in progress
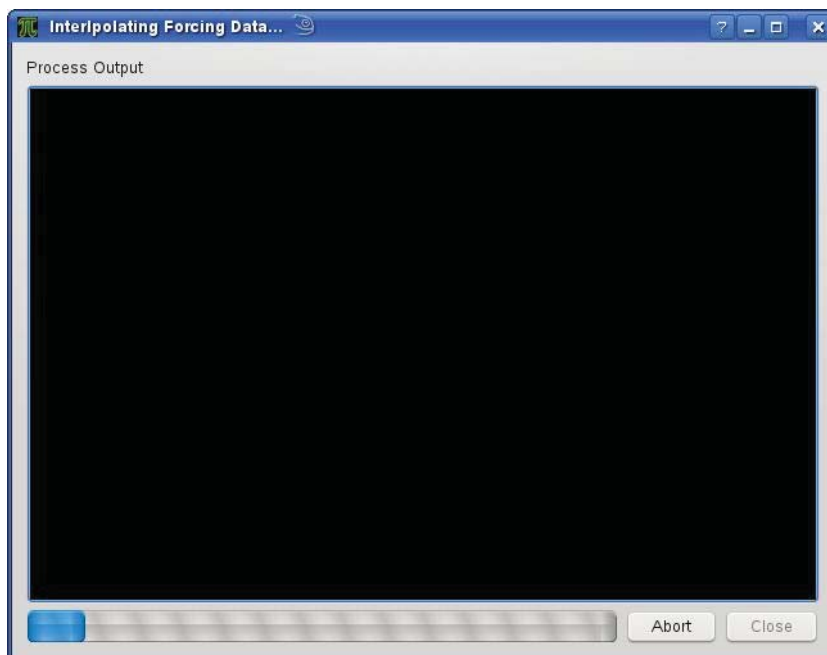
FIGURE A.14: Meteorological data interpolation in progress
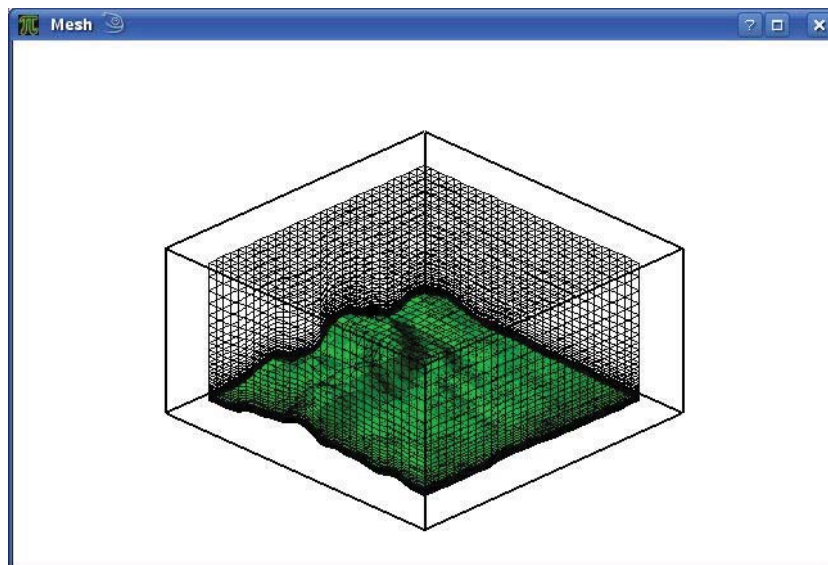
FIGURE A.15: Post processing: Topography and mesh visualization
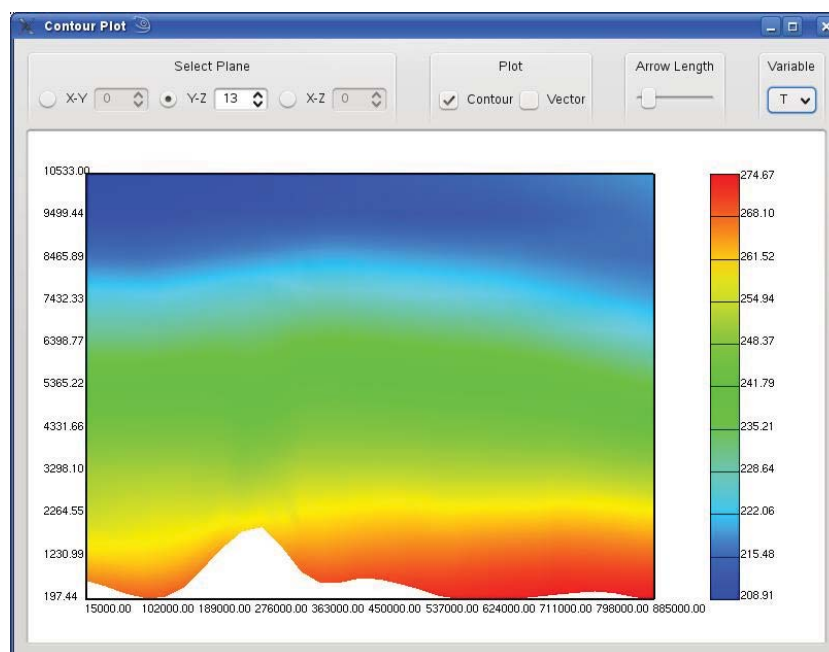
FIGURE A.16: Post processing: Contours
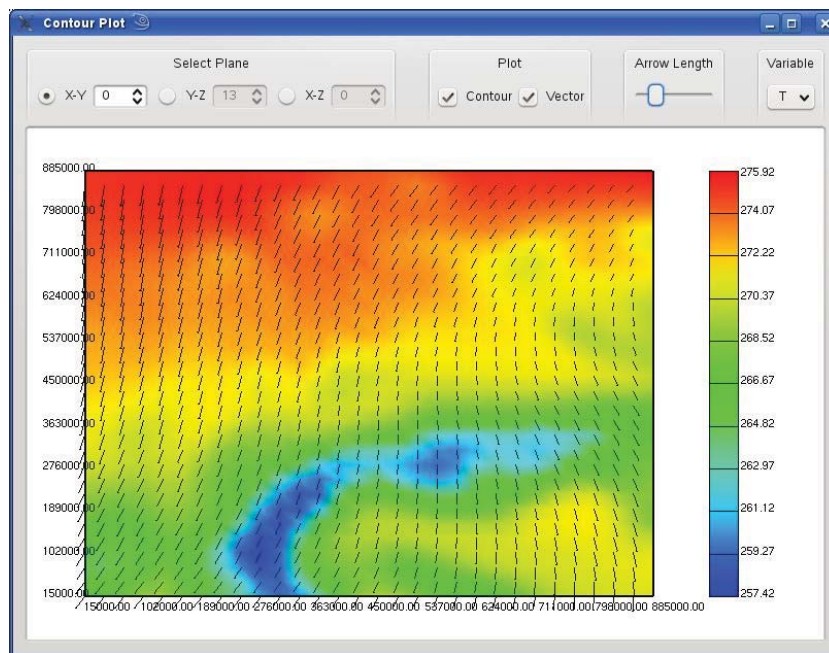
Figure A.17: Post processing: Vectors

Appendix B

Measuring Station Information

The following tale lists the different stations available during the BUBBLE IOP. They are divided into Urban (U), Rural (R) and Sub-urban (S) areas. The different urban and rural stations used for averaging procedure are emphasised.

Table B.1: A list of different BUBBLE measuring stations

Code on map (7.1)	Sttation name	Height [mASL]
Rp6	Aesch Schlatthof	353
Se1	Allschwil	277
Rp7	Airport Basel-Mulhouse	-
Sp2	Basel-Bäumlihof	289
Sp3	Basel-Binningen (ANETZ, NABEL)	316
Up6	Basel-Feldbergstrasse	255
Ue4	Basel-Horburg	254
Re3	Basel-Lange Erlen	275
Up7	Basel-Leonhard	273
Ue5	Basel-Kleinhüningen	265
Up8	Basel-Novartis Klybeck	255
Ue3	Basel-Messe	255
Up9	Basel-Novartis St. Johann	257
Up10	Basel-Roche	255
Ue2	Basel-Spalenring	278
Ue1	Basel-Sperrstrasse	255
Up11	Basel-St. Johann	260
Rp11	St. Chrischonaturm	490
Sp4	Dornach	325
Re4	Gempen	710
Re1	Grenzach	265
Sp5	Liestal LHA	320
Rp8	Oetlingen	450
Rp9	Pratteln Hardwasser	272
Sp6	Rheinfelden	285
Rp10	Schönenbuch	400
Sp7	Schweizerhalle	270
Re5	St. Louis	250
Re2	Village Neuf	240
Sp8	Weil am Rhein	250

Bibliography

Beckermann, C., Diepers, H., Steinbach, I., Karma, A., and Tong, X. (1999). Modeling melt convection in phase-field simulations of solidification. *Journal of Computational Physics*, 154:468–496.

Blackadar, A. (1968). The vertical distribution of wind and turbulent exchange in neutral atmosphere. *Journal of Geophysics*, 64:3085–3102.

Bornstein, R. (1987). Mean diurnal circulation and thermodynamic evolution of urban boundary layers, in modeling the urban boundary layer. *Am. Met. Soc.m Boston*, pages 52–94.

Bougeault, P. and Lacarre, P. (1989). Paramterisation of orography-induced turbulence in a mesobeta-scale model. *Monthly Weather Review*, 117:1872–1890.

Breuer, M., Lakehal, D., and Rodi, W. (1996). Flow around a surface mounted cubical obstacle: Comparison of les and rans-results. note on numerical fluid mechanics. *Vieweg Verlag*, 53:22–30.

Britter, R. and Hanna, S. (2003). Flow and dispersion in urban areas. *Annual Review of Fluid Mechanics*, 35:469–496.

Cheng, Y., Lien, F., Yee, E., and R, S. (2003). A comparison of large eddy simulation with a standard k-e reynolds-averaged navier-stokes model for the prediction of a fully developed turbulent flow over a matrix of cubes. *J. Wind Engineering and Industrial Aerodynamics*, 91:1301–1328.

Christen, A. (2005). Atmospheric turbulence and surfaces energy exchange in urban environments. results from the basel urban boundary layer experiment (bubble). *Diss. Phil.-Nat-Fak, University of Basel*, ISBN 3-85977-260-X.

Chung, T. (2002). *Computational Fluid Dynamics.* Cambridge.

Clappier, A. (1998). A correction method for use in multidimensional time-splitting advection algorithms: Application to two and three dimensional transport. *Monthly Weather Review*, 126:232–242.

Clappier, A., Perrochet, P., Martilli, A., Muller, F., and Krueger, B. (1996). A new non hyrostatic mesoscale model using a cvfe (control volume finite element) discretization technique. *EUROTRAC Symposium, Southampton, Computational Mechanics Publications*, 17:527–531.

Clarke, J. (2001). *Energy Simulation in Building Design.* Butterworth-Heimann.

Crowly, W. (1968). Numerical advection experiments. *Monthly weather review*, 96:1–11.

Driest, E. (1956). On turbulent flow near a wall. *PJ. Aero. Sci.*, 23:1007–1011.

Gambo, K. (1978). Notes on the turbulence closure model for atmospheric boundary layers. *Journal of the Meteorological Society of Japan*, 56:466–480.

Germano, M., Piomelli, U., Moin, P., and Cabot, W. (1991). A dynamic subgrid-scale eddy viscosity model. *Phys. Fluids A 3 (7),*, 91:1760–1765.

Graves, H., Watkins, R., Westbury, P., and Littlefair, P. (2001). Cooling buildings in london: Overcoming the heat island. *BRE*, Report 431:ISBN 9781860815263.

Hand, L. and Shepherd, J. (2009). An investigation of warm season spatial rainfall variability in oklahoma city: Possible linkages to urbanization and prevailing wind. *Journal of Applied Meteorology and. Climatology*, 48:251–269.

Hanna, S.R., C. J. and Strimaitis, D. (1993). Hazardous gas-model evaluation with field observations. *Atmos. Environ. A-Gen.*, 23:2265–2285.

Hosker, R. (1984). Flow and diffusion near obstacles. in atmospheric science and power production. 7:241–326.

Jacobson, M. (1999). *Fundamentals of atmospheric modelling.* Cambridge University Press, Cambridge UK.

Jones, B. (1992). Population growth, urbanization and disaster risk and vulnerability in metropolitan areas: a conceptual framework environmental management and urban vulnerability. *World Bank Discussion*, 168.

Klemp, J., B. and Lilly, D. (1975). The dynamics of wave-induced downslope winds. *Journal of Atmospheric Science*, 32:320–339.

Kolmogorov, A. (1941). A local structure of turbulence in incompressible viscous fluid for very large reynolds numbers. *Doklady ANSSSR*, 30:301–304.

Kolokotroni, M. and Giridharan, R. (2008). Urban heat island intensity in london: An investigation of the impact of physical characteristics on changes in outdoor air temperature during summer. *Solar Energy*, 83:986–998.

Kondo, H., Genchi, Y., Kikegawa, Y., Ohashi, Y., Yoshikado, H., and Komiyama, H. (2005). Development of a multi-layer urban canopy model for the analysis of energy consumption in a big city: Structure of the urban canopy model and its basic performance. *Boundary-Layer Meteorology*, 116:395–421.

Kondo, H. and Liu, F. (1998). A study on the urban thermal environment obtained through one-dimensional urban canopy model. *J Jap Soc Atmos Environ*, 33:179–192.

Krpo, A. (2009). Development and application of a numerical simulation system to evaluate the impact of anthropogenic heat fluxes on urban boundary layer climate. *PhD thesis, Swiss Federal Institute of Technology Lausanne*, 4428.

Kurihara, Y. (1976). On the development of spiral bands in a tropical cyclone. *Journal of Atmospheric Science*, 33:940–958.

Kusaka, H., Kondo, H., Kikegawa, Y., and F., K. (2001). A simple single-layer urban canopy model for atmospheric models: Comparision with multi-layer and slab models. *Boundary-Layer Meteorology*, 101:329–358.

Lakehal, D. and Rodi, W. (1997). Calculation of the flow past a surface-mounted cube with 2-layer models. *Journal of Wind Engineering and Industrial Aerodynamics*, 67:65–78.

Lemonsu, A., G. C. M. V. (2004). Modelling the surface energy balance of an old mediterranean city core. *Journal of Applied Meteorology*, 43:312–327.

Leveque, R. (2002). Finite volume method for hyperbolic problems. *Cambridge University Press, Washington*.

Lilly, D. (1992). A proposed modification of the germano subgrid-scale closure method. *Phys. Fluids*, 4:633–635.

Louis, J. (1979). A parametric model of vertical eddies fluxes in the atmosphere. *Boundary Layer Meteorology*, 17:187–202.

Martilli, A. and Santiago, J. (2007). Cfd simulation of air flow over a regular array of cubes. part ii: analysis of spatial average properties. *Boundary-Layer Meteorology*, 122:635–654.

Martilli, A., C. A. and Rotach, M. (2002). An urban surface exchange parametrization for mesoscale models. *Boundary Layer Meteorology*, 104:261–304.

Martinuzzi, R. and Tropea, C. (1993). The flow around surface-mounted, prismatic obstacles placed in a fully developed channel flow. *Journal of Fluid Engineering*, 115:85–91.

Masson, V., G. C. and Oke, T. (2002). Evaluation of the town energy balance (teb) scheme with direct measurements from dry districts in two cities. *Journal of Applied Meteorology*, 41:1011–1026.

Masson, V. (2000). A physically-based scheme for the urban energy budget in atmospheric models. *Boundary Layer Meteorology*, 94:357–397.

McBean, G. and Elliott, J. (1975). Vertical transport of kinetic energy by turbulence and pressure in boundary-layer. *Journal of Atmospheric Science*, 32:753–766.

Meinders, E. (1998). Experimental study of heat transfer in turbulent flows over wall-mounted cubes. *PhD thesis Faculty of Applied Sciences, Delft University of Technology, Delft, Netherlands.*

Meinders, E. and Hanjalic, K. (1999). Vortex structure and heat transfer in turbulent flowover a wall-mounted matrix of cubes. *Int. J. Heat Fluid Flow*, 20:255–267.

Mills, G. (1997). An urban canopy-layer climate model. *Theoretical Applied Climatology*, 57:229–244.

Muller, C. (2007). Improvement of an urban turbulence parameterization for meteorological operational forecast and air quality modelling. *PhD thesis N° 3766,.*

Noihan, J. (1981). A model for the net total radiation flux at the surfaces of a building. *Building and Environment*, 16(4):259–266.

Oke, T. (1973). City size and urban heat island. *Atmospheric Environment*, 7:769–779.

Oke, T. (1987). *Boundary Layer Climates.* 2nd edn. London: Metheu, 384pp.

Oke, T. (1988). *An Introduction to Boundary Layer Meteorology.* Kluwer Academic Publisher, Dordrecht, 670pp.

Otte, T., Lacser, A., Dupont, S., and Ching, J. (2004). Implementation of an urban canopy parametrization in a mesoscale meteorological model. *Journal of Applied Meteorology*, 43:1648–1665.

Perez, R., R., S., and Michalsky, J. (1993). All-weather model for sky luminance distribution-preliminary configuration and validation. *Solar Energy*, 50(3):235–245.

Peskin, C. (1977). Numerical analysis of blood flow in the heart. *Journal of Computational Physics*, 25:220–238.

Robinson, D., Haldi, F., Kaempf, J., Leroux, P., Perez, D., Rasheed, A., and Wilke, U. (2009). From the neighbourhood to the city: Resource flow modelling for urban sustainablity. *CISBAT*.

Robinson, D. and Stone, A. (2004). Solar radiation modelling in the urban context. *Solar Energy*, 77(3):295–309.

Robinson, D. and Stone, A. (2005). A simplified radiosity algorithm for general urban radiation exchange. *Building Services Engineering Research and Technology*, 26-4:271–284.

Roches, A. (2007). Développement d'un préprocesseur de modèles météorologiques. *MSc. Thesis, Swiss Federal Institute of Technology lausanne.*

Rotach, M. (2001). Simulation of urban-scale dispersion using a lagrangian stocastic dispersion model. *Boundary Layer Meteorology*, 99:379–410.

Rotach, M., Vogt, R., Bernhofer, C., Batchvarova, E., Christen, A., C. A. F. B. G. S., Martucci, S., Mayer, G., H.V., M., Oke, T., parlow, E., Richner, H., Roth, M., Roulet, Y.-A., Ruffieux, D., Salmond, J., Schatzmann, J., and Voggt, J. (2005). An urban meteorology project. *Theoretical Applied Climatology*, DOI: 10.1007/s00704-004-0117-9.

Rotach, M., W. (1993). Turbulence close to rough urban surface. part 1: Reynolds stress. *Boundary Layer Meteorology*, 65:1–28.

Roth, M. (2000). Review of atmospheric turbulence over cities. *Q.J.R. Meteorological Society*, 126:941–990.

Roulet, Y. (2004). Validation and application of an urban turbulence parameterisation scheme for mesoscale atmospheric models. *PhD Thesis, Swiss Federal Institute of Technology, Lausanne*, 3032.

Roulet, Y.-A., Martilli, A., Rotach, M., and Clappier, A. (2005). Validation of an urban surface exchange parameterization for mesoscale models -1d case in a street canyon. *Journal of Applied Meteorology*, 44:1484–1498.

Salamanca, F. and Martilli, A. (2008). A new building energy model coupled with an urban canopy parameterization for urban climate simulations-part ii. validation with one-dimensional off-line simulations. *Submitted to Theoretical Applied Climatology.*

Santiago, J., Conceal, O., Martilli, A., and Blecher, S. (2007). Variation of the sectional drag coefficient of a group of buildings with packing density. Submitted to Boundary-Layer Meteorology.

Sasamori, T. (1999). Radiative cooling calculation for application to general circulation experiments. *Journal of Applied Meteorology*, 16:721–729.

Schayes, G. (1982). Direct determination of diffusivity profiles from synoptic reports. *Atmospheric Environment*, 16:1407–1413.

Seinfield, J. and Pandis, S. (1998). *Atmospheric chemistry and physics from air pollution to climate change.* John Wiley and Sons, 1326 pp.

Shepherd, J. (2005). A review of current investigations of urban-induced rainfall and recommendations for the future. *Earth Interactions*, 9-No. 12:1–27.

Shepherd, J. and Mehta, A. (2002). Summary of first gpm partners planning workshop. *NASA Conference Publication-2002-210012-GPM Report 1, Available at NASA/GSFC*, pages 1–37.

Stanners, D. and Bourdeau, P. (1995). Europe's environment: the dobris assessment. *European Environmental Agency, Copenhagen.*

Taha, H. (1999). Modifying a mesoscale meteorological model to better incorporate urban heat storage: A bulk parametrization approach. *Journal of applied Meteorology*, 38:446–473.

Tennekes, H. and Lumley, J. (1972). *A First Course in Turbulence.* MIT Press.

Thuborn, J. (1996). Tvd schemes, positive schemes and universal limiters. *Monthly weather review*, 125:1990–1993.

Tregenza, P. and Sharples, S. (1993). Daylighting algorithms. *ETSUS, UK*, pages 1350–1993.

Vu, T. C., Asaeda, T., and Ashie, Y. (1999). Development of a numerical model for the evaluation of the urban thermal environment. *Journal of Wind Engineering and Industrial Aerodynamics*, 81:181–191.

Wang, T., A. and Lin, Y.-L. (1999). Wave ducting in a stratified shear flow over a two dimensional mountain. part ii: Implications for the development of high drag states for severe downslope windstorms. *Journal of Atmospheric Science*, 56:437–452.

Watanabe, T. and Kondo, J. (1990). The influence of the canopy structure and density upon te mixing length within and above vegetation. *Journal of Meteorological Society of Japan*, 68:227–235.

Adil RASHEED

EPFL-ENAC-ICARE-LESO-PB
Station-18
CH-1015
Lausanne, Switzerland
Languages: English, Hindi

Date of Birth: 28.11.1981
Nationality: Indian
adil.rasheed@gmail.com
Cell : 41-(0)786790812
www.adilrasheed.com

WORK EXPERIENCE

Research Scientist
2009-

SINTEF ICT
Department of Applied Mathematics, Trondheim, Norway
– Turbulence predictions on airports

Doctoral Assistant
2005-2009

Laboratory of Solar Energy and Building Physics
Swiss Federal Institute of Technology, Lausanne, Switzerland
– Supervision and development of Graphical User Interface for MESOSIM, a mesoscale modelling tool
– Supervision and development of GEOSIM, a tool for finding an equivalent geometry using Simplified Radiosity Algorithm and Immersed Surface Technique
– Co-development of Atmospheric codes
– Development of a new urban canopy model to simulate the effect of urban texture on the atmosphere using large Eddy Simulation
– Supervision and development of a 3-D modeling tool using gts library
– Development of structured and unstructured Navier Stokes solvers
– Compilation of scientific reports and presentations in International Conferences
– Guided architecture students in analyzing their design using building simulation tools and city planning tools

Associate Engineer
Aug-Oct 2005

Induslogic Pvt. Ltd.
Noida, India
– Undergone an intensive three weeks of training in advanced programming
– Worked on a telecommunication project involving VOIP and SIP technologies

Research Assistant
2004-2005

Mechanical Engineering Department
Indian Institute of Technology Bombay, India
– Developed CFD codes for simulating the scavenging process of a Two Stroke IC Engine
– Helped undergraduate students in solving partial differential equations using numerical methods
– Graded tutorials and exams

Summer Trainee
May-June 2003

Isha Steels Heat Treatment Plant
Mumbai, India
– Studied the heat transfer characteristics of components made of different materials using CFD
– Prospects of using cogeneration in different units of the plant were also examined

EDUCATION

PhD

Laboratory of Solar Energy and Building Physics
SWISS FEDERAL INSTITUTE OF TECHNOLOGY, Lausanne, Switzerland
Thesis: *Multiscale Modelling of Urban Climate*
Skills acquired: CFD, Large Eddy Simulation, Immersed Boundaries, Economics of Climate Change, Sustainable Development, Building Physics, Atmospheric Flow Modelling, Aeroelasticity, Finite Volume Method, Finite Element Method

Master of Technology

Thermal and Fluids Engineering
INDIAN INSTITUTE OF TECHNOLOGY BOMBAY, India
Thesis: *Experimental and Numerical Modeling of the Scavenging Process of a Two Stroke Engine*
Skills acquired: Steam and Gas Turbine, Wind Engineering, Advanced Heat and Mass Transfer, CFD, Advanced Combustion and Thermodynamics, Convective Heat and Mass Transfer, Power Plant Engineering, Fuel Cells, Numerical Methods in Engineering,

Bachelor of Technology

Mechanical Engineering
INDIAN INSTITUTE OF TECHNOLOGY BOMBAY, India
Thesis: *Evaluation of the performance of various Heat Transfer Enhancement Devices in a square channel*
Skills acquired: Refrigeration and Air Conditioning, Industrial Engineering and Operation Research, Internal Combustion Engines, Introduction to CAD/CAM, Experimental Engineering, Solid Mechanics

Junior and Senior Diploma

Fine Arts (painting)
Vani Chitrakala Kendra, Ranchi (RABINDRA BHARATHI UNIVERSITY, Kolkata India)
Skills acquired: Sketching, Painting, Designing

CREDENTIALS

– **National Science Foundation, PNR 41**, Doctoral Dissertation Research
– Attended a week long course on "Large Eddy Simulation" organized by Prof. Lars Davidson in Goteborg, Sweden
– Attended CEP Certificate Course in Advanced Programming (C++) and achieved the highest grade
– **Institute Merit-Cum-Means Scholarship** 2000-2005
– Awarded the **Certificate of Merit** for being in the **top 0.1%** of the students appearing in the Matriculation exam all over India.
– Scored 87% marks in **National Mathematics Olympiad Contest** organized by DAMT
– Awarded the **Institute Cultural Color** award for my contribution to the cultural scene of IIT Bombay
– Awarded **"Special Mention"** for my contribution to the Performing Arts Festival 2002 and 2005 of IIT Bombay

COMPUTER SKILLS

OS: Windows, Linux, Mac
Text processing: LATEX, Microsoft Office, HTML
Programming Languages: C++ , Fortran, Shell Scripting
CFD and atmospheric codes: Fluent, TransAT, Envi-Met, OpenFVM, Indigenous Code
Solid Modelling Softwares: Pro-Engineer, Rhinoceros, Auto CAD
Building Simulation Software: ESP-r

Image and Video Processing Softwares: Photoshop CS3, Adobe Premiere, Adobe Lightroom

ORGANIZATIONAL SKILLS

Institute Fine Arts Secretary, IIT Bombay
– Led the institute team to victories in two major inter college fine arts events at the national level
– Efficiently worked with the limited resources available to organize various events
– Managed a group of ten secretaries and a workforce of about 50 people

Hostel Photography and Fine Arts Secretary
– Awarded the **Best Office Bearer Award** for my contributions
– Designed the sets and stages for most of the dramatics events

EXTRA CURRICULAR ACTIVITIES

Painting
– Exhibited paintings in the **International Art Fair 2007** in **Palexpo**, Geneva
– Exhibited paintings in Zurich with the **Ambassador of India**
– Exhibited paintings in Fribourgh, Mumbai and Ranchi
– Participated in the world's biggest open air painting workshop **Art Air 2007**

Photography
– Self learned photographer with works exhibited on my personal photoblog
– Worked as a freelance club photographer for steveworld.ch
– Recently working on High Dynamic Range Imaging techniques

Travelling
– Travelled to USA, UK, Norway, Sweden, Finland, Japan, France, Switzerland, Germany, Estonia, Latvia, Spain, India, Japan, Portugal, Italy

Others
– Blogging, cooking and reading

INTERNATIONAL PUBLICATIONS AND CONFERENCES

Rasheed, A., Robinson, D., Clappier, A., Narayanan, C., Lakehal, D. *"On the effect of complexities in urban geometry on mesoscale modelling "*. Submitted to the special edition of the International Journal of Climatology

Rasheed, A., Nandi, K., Date, A.W., *"A Novel Experimental Set-up for Investigation of Perfect Mixing and Perfect Displacement Models of the Scavenging process in a Cavity"*, 7th World Conference on Experimental Heat Transfer, Fluid Mechanics and Thermodynamics 2009, Krakow, Poland

Rasheed, A., Robinson, D., Narayanan, C., Lakehal, D., *"On the effects of Complex Urban Geometries on Mesoscale"*, 7th International Conference on Urban Climate 2009, Yokohama, Japan

Rasheed, A., Robinson, D., Clappier, A.,, *"Development of a New Urban Canopy Model"*, 7th International Conference on Urban Climate 2009, Yokohama, Japan

Rasheed, A., Robinson, D., *"Multiscale modeling of the Urban Climate"* Proc. Eleventh Int. IBPSA Conf: Building Simulation 2009, Glasgow, UK

Nadege Blond, Luis C. Belalcazar, Adil Rasheed, Alain Clappier, Sebastian Huttner, Michael Bruse *"Design and Test of a System to Simulate Road Traffic Emissions"* Annales de l'ISUP 2008

Rasheed, A., Robinson, D., Clappier, A. *"Investigation of the nature of the dispersive fluxes in Urban*

Parametrization using Large Eddy Simulation" 2008 Annual Meeting, Boston, Massachusetts

Rasheed, A., Robinson, D., Clappier, A., Narayanan, C., Lakehal, D. *"Characterization of dispersive fluxes in Mesoscale models using LES of flow over an array of cube"*. Submitted to Atmospheric Environment

Rasheed, A., Robinson, D., Clappier, A. *"On the sensitivity of Building Performance to the Urban Heat Island Effect"*. [CISBAT 2007]

TECHNICAL REPORTS AND SCIENTIFIC TALKS

A talk on the modeling of urbal climate: *"Urban Atmospheric Modeling"*, SINTEF, Trondheim, Norway, 2009

A talk on new advancements in Urban Climate Modelling: *"Multiscale modeling of the Urban Climate"*, Hotel Novotel, Paris, 2009

Final Scientific report for Swiss National Science Foundation *"Multiscale Modelling of Building-Urban Interactions"*,Project: NRP 54 Sustainable Development of the Built Environment

Rasheed, A. *"Numerical and Experimental study of the Scavenging Process of a Two Stroke IC Engine"*, Masters Thesis, Mechanical Engineering Dept., Indian Institute of Technology Bombay 2005

Rasheed, A. *"Evaluation of the performance of various Heat Transfer Enhancement Devices in a square channel"*, Bachelors Thesis, Mechanical Engineering Dept., Indian Institute of Technology 2004

REFERENCES

Darren Robinson (darren.robinson@epfl.ch)
Alain Clappier (alain.clappier@epfl.ch)
A.W. Date (awdate@me.iitb.ac.in)
Himanshoo Saxena (himanshoo.saxena@gmail.com)

DECLARATION

I hereby confirm that the information given above is true to the best of my knowledge and belief and proof of any can be submitted if requested for.
 –Adil Rasheed